

Variability in Labrador Sea Water formation

Variabiliteit in the formatie van Labrador Zee Water

(met een samenvatting in het Nederlands)

Proefschrift

ter verkrijging van de graad van doctor aan de Universiteit Utrecht op gezag an de rector magnificus, prof.dr. G.J. van der Zwaan, ingevolge het besluit van het college voor promoties in het openbaar te verdedigen op maandag 14 mei 2012 des middags te 2.30 uur

door

Renske Gelderloos

geboren op 13 februari 1983 te Zuidhorn

Promotor: Prof. dr. W.P.M. de Ruijter

Co-promotor: Dr. C.A. Katsman

To my father, who believed in the light.

Abstract

The Labrador Sea is located in the northwestern corner of the North Atlantic Ocean. Although small in size, this sea is very important for the circulation in the ocean, because it is one of the few locations where deep convection takes place. Deep convection is vertical mixing of water over a large depth in the ocean, occasionally down to more than two kilometers depth in the Labrador Sea area. This process is the only way in which the water in the deep ocean is exposed to the atmosphere, and the only rapid interaction between water in the deep ocean and in the surface layer.

Deep convection is a typical winter process. The large-scale ocean circulation brings warm water from the Southern Hemisphere to the North Atlantic Ocean in the upper few hundred meters. In the subtropical region, large amounts of evaporation make the water saltier. This saline and warm water is then carried to the subpolar region, where part of it flows into the Labrador Sea. Here, strong winds from the North American continent bring in cold and dry air. The still relatively warm ocean water is strongly cooled down by the cold air, which makes the surface water denser. When the surface water is denser than the water underneath, it will mix (vertically) with the subsurface water. The much colder water returns to the Southern Hemisphere in the abyssal ocean.

While the atmosphere cools down the ocean, the ocean warms up the atmosphere. The warmed air is brought to the European continent by the prevailing westerly winds, which is why the winters in western Europe are relatively mild compared to other places at a similar latitude. The large-scale ocean circulation that transports heat to the North Atlantic Ocean shows a large variability, and studies have shown that the variability in this circulation is linked to variability in the formation of Labrador Sea Water on time scales of years to decades. Therefore, it is important to understand the variability in Labrador Sea Water formation.

Two of the processes that play an important role in this variability are studied in this dissertation. The first study focuses on the spring and summer period after a deep convection event. In these months the typical layered structure of the ocean, which is destroyed by the deep convective mixing, is quickly restored. The dense water in the area affected by deep convection is then (partly) replaced by lighter (warmer or fresher) water, originating from currents that encircle the interior Labrador Sea (called boundary currents). This process, known as 'restratification', is governed by eddies, which are coherent structures in the ocean in a swirling motion.

In the Labrador Sea, three different types of eddies are known to play role in this 'restratification' process. First, Convective Eddies are relatively small eddies (a radius of about 10 km) which form around the area where deep convection takes place. During and directly after deep convection, they mix the water in the convected area with the surrounding water. Second, Boundary Current Eddies, also relatively small, mix water from the boundary currents into the interior basin. Third, Irminger Rings are large (a radius of about 25 km) eddies that are formed off the west coast of Greenland due to a steepening of the slope at this location. These eddies bring the light water from the boundary current quickly to the deep convection area. Furthermore, they very efficiently stir the interior Labrador Sea which may enhance the efficiency of the smaller eddies in the restratification process.

Using a numerical model in a highly idealized configuration for the Labrador Sea, the contributions of these three eddy types to the restratification process after deep convection were quantified. The Convective Eddies and Boundary Current Eddies together replenished 30% of the heat that was lost during deep convection. Irminger Rings added another 45% to this number. The presence of Irminger Rings is thus essential for a realistic amount of restratification in this area.

The second process study focuses on the effects of a very fresh surface layer on deep convection. Fresh water is light, and therefore the wintertime cooling needs to be very strong to make the surface water denser than the subsurface water. A fresh surface layer can thus inhibit deep convection, a phenomenon that is well known. From 1969 to 1971, convection was restricted to the upper 300 m. This shutdown has been attributed to a substantial surface freshening. The abrupt resumption of convection in 1972, in contrast, is attributed to the exceptionally cold winter. Using the data collected at the Ocean Weather Station Bravo in the central Labrador Sea, the causes of the shutdown and resumption of deep convection are studied in detail.

The shutdown started as a result of the combined effects of the fresh surface water and the very mild winter conditions. Once convection was shut down, the wintertime temperature of the surface water decreased, which caused a reduction in the heat loss to the atmosphere. Thus, while a large heat loss was required for deep convection, a side effect of having no deep convection is a smaller heat loss.

A second effect of the lower surface water temperature was that the thermal expansion coefficient, which gives the change in density as a function of temperature, was reduced. As a consequence, a certain heat loss gives a smaller density change of the surface water. Both effects reinforce the shutdown state. In 1972, deep convection returned both because of the exceptionally harsh winter as well as advection of saltier waters into the convection region.

Apart from understanding the variability in Labrador Sea Water formation, it is also important to monitor this variability. *In situ* monitoring is however severely hampered by the harsh winter conditions. Furthermore, the monitoring programs do not cover the entire Labrador Sea and are often summer observations. The network of satellite altimeters does not suffer from these limitations and could therefore give valuable additional information. Altimeters can in theory detect deep water formation, because the water column becomes denser during convection and therefore the sea surface becomes lower. Because this signal is small compared to variability in sea surface height induced by other processes, the local depth of deep convection at a certain location and certain time does not correspond well to the sea surface height anomaly at that location and time. However, from the satellite altimetry data the approximate depth of deep convection (less than 1000 m, between 1000 and 1500 m or more than 1500 m depth) and the location of the convection area at a larger scale can be determined.

Samenvatting

De Labrador Zee ligt in het noordwesten van de Noord Atlantische Oceaan. Ondanks het feit dat deze zee maar een heel klein deel van oceaan beslaat, speelt het een belangrijke rol in de grootschalige oceaancirculatie omdat het een van de weinige locaties is waar diepe convectie plaatsvindt. Bij diepe convectie wordt oceaanwater tot op grote diepte gemengd met het oppervlaktewater. In de Labrador Zee kan dit wel tot twee kilometer diepte zijn. Dit is het enige manier waarop water in de diepte van de oceaan in contact kan komen met de atmosfeer, en tevens de enige manier waarop water uit de diepte en water uit de oppervlaktelaag op een snelle manier eigenschappen kunnen uitwisselen.

Diepe convectie vindt alleen plaats in de winter. De grootschalige oceaancirculatie brengt in de bovenste paar honderd meter warm water vanaf het zuidelijk halfrond naar de Noord Atlantische Oceaan. Doordat veel zoet water verdampt in de subtropen wordt het water in deze bovenste laag een stuk zouter. Dit warme en zoute water stroomt verder in noordelijke richting naar subpolaire streken, waar een gedeelte de Labrador Zee instroomt. Hier wordt koude en droge lucht aangevoerd vanuit Noord Amerika door sterke noordwestelijke winden. Het oceaanwater, dat nog steeds relatief warm is ten opzichte van de koude lucht, wordt snel afgekoeld en krijgt daardoor een hogere dichtheid. Als het water aan de oppervlakte een hogere dichtheid heeft bereikt dan het water dat eronder zit, zullen deze lagen (vertikaal) mengen. Het sterk afgekoelde water stroomt dan in de diepe oceaan terug richting het zuidelijk halfrond.

Terwijl de atmosfeer de oceaan afkoelt, warmt de oceaan de atmosfeer op. Doordat de wind hier overwegend westelijk is, stroomt de opgewarmde lucht richting Europa. Daarom zijn de winters in West Europa relatief mild in vergelijking met andere plaatsen op een vergelijkbare breedtegraad. Er is veel variabiliteit in de grootschalige oceaancirculatie die warmte naar de Noord Atlantische Oceaan

brengt en verschillende studies hebben laten zien dat deze variabiliteit, op een tijdschaal van jaren tot enkele tientallen jaren, samenhangt met de variabiliteit in de vorming van Labrador Zee Water. Daarom is het belangrijk om de variabiliteit in de formatie van Labrador Zee Water te begrijpen.

In deze dissertatie worden twee processen die een belangrijke rol spelen in deze variabiliteit onderzocht. In de eerste studie wordt de voorjaars- en zomerperiode bestudeerd die volgt op diepe convectie. In deze maanden wordt de gelaagde structuur van de oceaan, die door het verticale mengen tijdens diepe convectie is verdwenen, snel hersteld. Het water dat een hoge dichtheid heeft gekregen tijdens diepe convectie wordt dan (gedeeltelijk) vervangen door water met een lagere dichtheid (omdat het warmer of zoeter is), dat afkomstig is van de zeestromingen die langs de rand van de Labrador Zee stromen (grenslaagstromingen). Dit proces staat bekend als restratificatie. De uitwisseling tijdens dit proces gebeurt in de vorm van oceaantwervels, die het best kunnen worden omschreven als grote coherente structuren met een ronddraaiende stroming.

Drie soorten wervels spelen een rol in het restratificatieproces in de Labrador Zee. Ten eerste zijn er de Convectieve Wervels (straal van circa 10 km) die gevormd worden aan de rand het gebied waar diepe convectie plaatsvindt. Zowel tijdens als ook na afloop van de diepe convectie mengen deze wervels het water in het geconvecteerde gebied met het omringende water. Ten tweede zijn er de Grenslaagstromingswervels, die water vanuit de grenslaagstromingen die de Labrador Zee omringen richting het centraal gelegen gedeelte van de Labrador Zee mengen. Ten derde zijn er de Irminger Ringen, relatief grote wervels (straal van circa 25 km) die aan de westkust van Groenland gevormd worden door een toename van de helling in de bathymetrie. Deze wervels brengen het water met een lage dichtheid vanuit de grenslaagstromingen aan de rand van de Labrador Zee snel bij het gebied waar de diepe convectie plaatsvindt. Daarnaast roeren deze wervels het water in de Labrador Zee op effectieve wijze en kunnen ze op deze manier de efficiëntie van de kleinere wervels in het restratificatieproces vergroten.

De rol van deze drie soorten wervels in het restratificatieproces is bestudeerd met behulp van een numeriek model dat gerund is in een zeer geïdealiseerde configuratie van de Labrador Zee. De Convectieve Wervels en Grenslaagstromingswervels vulden samen 30% van de warmte die verloren was gegaan tijdens de diepe convectie weer aan. De Irminger Ringen voegden hier nog eens 45% aan toe. Irminger Ringen zijn dus essentieel voor een realistische restratificatie in dit gebied.

In de tweede processtudie worden de effecten van een hele zoete bovenlaag op diepe convectie onderzocht. Omdat zoet water licht is, moet de afkoeling in de winterperiode heel sterk zijn om het water zwaarder te maken dan het water in de onderliggende laag. Op deze manier kan een zoete bovenlaag diepe convectie

voorkomen, een fenomeen dat algemeen bekend is bij oceanografen. Tussen 1969 en 1971 was convectie beperkt tot de bovenste 300 m. Het gebrek aan diepe convectie in deze periode wordt toegeschreven aan een zeer verzoete bovenlaag. De terugkeer van diepe convectie in 1972 wordt daarentegen toegeschreven aan de zeer koude winter. De details van de oorzaken van de stop en terugkeer van diepe convectie worden onderzocht met behulp van de data die zijn verzameld door het weerschip Bravo in het centrale gedeelte van de Labrador Zee.

Diepe convectie stopte door een combinatie van de zoete bovenlaag en de zeer milde winter. Zodra diepe convectie was gestopt, nam de temperatuur van de bovenlaag verder af, wat een afname in de warmteflux naar de atmosfeer tot gevolg had. Terwijl er dus een grote warmteflux nodig was om diepe convectie te laten terugkeren, was een neveneffect van de afwezigheid van diepe convectie dat de warmteflux kleiner was. Een tweede effect van de lage oppervlaktewatertemperatuur was een lagere waarde van de thermische expansie coëfficiënt, die de verandering van de dichtheid bij een verandering in temperatuur geeft. Het gevolg hiervan is dat een bepaalde warmteflux een kleinere verandering van de dichtheid van het oppervlaktewater tot gevolg heeft. Beide effecten houden de situatie zonder convectie in stand. In 1972 keerde diepe convectie terug, zowel door een zeer strenge winter alsook advection van zouter water naar het convectiegebied.

Naast het feit dat we de variabiliteit in de vorming van Labrador Zee Water beter willen begrijpen, is het ook belangrijk om deze variabiliteit te monitoren. Het monitoren ter plaatse is echter moeilijk door de strenge wintercondities. Daarnaast bestrijken de monitoring programma's niet de hele Labrador Zee en worden de metingen vaak in de zomer gedaan. Het satellietnetwerk voor altimetrie (hoogtemetingen) heeft geen last van deze beperkingen en kan dus waardevolle aanvullende informatie verschaffen. In theorie zouden hoogtemeters recent gevormd Labrador Zee Water kunnen detecteren, omdat het water een hogere dichtheid krijgt, het volume dus afneemt en daardoor het wateroppervlak een stukje daalt. Omdat andere processen een veel grotere variabiliteit in oppervlakteniveau tot gevolg hebben, is er geen directe relatie tussen het oppervlakteniveau op een bepaald moment en een bepaald tijdstip enerzijds en de diepte van de menglaag als gevolg van diepe convectie anderzijds. Echter, gemiddeld over een groter gebied kan aan de hand van altimetriemetingen wel de menglaagdiepte bij benadering worden bepaald (minder dan 1000 m, tussen de 1000 m en 1500 m of dieper dan 1500 m) en kan tevens de locatie van het geconvecteerde gebied worden bepaald.

Contents

1	Introduction	1
1.1	The importance of deep convection	1
1.2	General deep convection theory	2
1.3	Water masses in the Atlantic Ocean	4
1.4	Labrador Sea Water formation	6
1.4.1	Hydrographic characteristics of the Labrador Sea	6
1.4.2	Prevailing atmospheric conditions	9
1.4.3	Observed variability in Labrador Sea deep convection	11
1.5	Outline of the dissertation	11
2	The Roles of Three Eddy Types in Restratification after Deep Convection	15
2.1	Introduction	15
2.2	Model and initial state	19
2.2.1	Model configuration	19
2.2.2	Setting the initial state	21
2.2.3	The eddy field	23
2.2.4	Set-up of the simulations	25
2.3	Restratification after deep convection	26
2.3.1	Heat content change of the convection area	28
2.3.2	Export of LSW by the boundary current	29
2.4	Restratification time scale	30
2.4.1	Derivation of restratification time scales	31
2.4.2	Observation-based restratification time scales	33
2.4.3	Model-based restratification time scales	36
2.5	Discussion	36
2.6	Summary and Conclusions	39

Appendix A: Derivation of τ_{CE}	40
Appendix B: Derivation of $\tau_{extCE+BCE}$	41
Appendix C: Derivation of τ_{IR}	43
3 Mechanisms behind the temporary shutdown of deep convection in the Labrador Sea: Lessons from the Great Salinity Anomaly years 1968-1971	45
3.1 Introduction	46
3.2 Hydrographic characteristics at OWS Bravo	49
3.3 Air-sea fluxes	50
3.3.1 Conditions at the air-sea interface	51
3.3.2 Heat fluxes	52
3.4 Absence of deep convection in 1969-1971	53
3.4.1 Buoyancy storage through increased stratification	55
3.4.2 Reduced surface buoyancy flux	56
3.4.3 Cause of the shutdown: 1D mixed layer model analysis	61
3.5 Return of deep convection in 1972	63
3.6 Summary and discussion	64
4 Detecting newly-formed Labrador Sea Water from space	69
4.1 Introduction	69
4.2 Convective activity in the period 1993-2009	71
4.3 Sea Surface Height anomaly data: AVISO	73
4.4 Detecting newly-formed Labrador Sea Water using altimetry	77
4.4.1 Visual inspection: detecting the chimney	77
4.4.2 Time and space-averaged SSH anomalies	78
4.4.3 Time-dependent SSH anomalies	78
4.4.4 When altimetry seems to fail: 2006 and 2007	81
4.4.5 When in situ monitoring programs disagree: 1996, 1998, 2002 and 2005	83
4.5 Potential of altimetry as a monitoring tool	84
4.5.1 Float-based mixed layer depth	84
4.5.2 Relating SSH anomaly to mixed layer depth	87
4.6 Summary and Conclusions	87
5 Conclusions and Outlook	91
5.1 Conclusions on the process studies	91
5.2 Detecting LSW formation from space	93
5.3 Outlook	94
Bibliography	97

Contents	xv
Acknowledgements	105
Curriculum Vitae	107

Chapter 1

Introduction

*"Knowledge of the oceans is more than a matter of curiosity.
Our very survival may hinge upon it."*

John F. Kennedy

1.1 The importance of deep convection

Deep convection in the ocean produces dense water masses which spread from their formation site and fill the abyssal and mid-depth ocean. In this way, they greatly affect the density structure of the ocean at depth. Being the only means of direct interaction between the deep ocean and the atmosphere, deep convection is a very interesting process from a climate point of view. Dense water formation is considered to play an important role in the Atlantic Meridional Overturning Circulation (AMOC). This circulation, sometimes referred to as the Thermohaline Circulation, is the large-scale circulation in the meridional-depth plane that is characterized by density gradients. The circulation transports a large amount of heat (on the order of 1 PW, a PW being 10^{15} W) in the surface waters from the Southern Hemisphere to the North Atlantic Ocean, where much of the heat is lost to the atmosphere. The prevailing westerly winds at midlatitudes bring this relatively warm air towards Europe. As a result, the western European climate is relatively mild compared to other places at a similar latitude.

For a long time deep convection was considered to directly drive the AMOC. In this view the ocean resembles a large heat engine where deep convection sets meridional density gradients, which in turn drive an overturning circulation. Marotzke and Scott (1999) however showed that deep convection is not a *source* of energy, but rather a *sink* (see Wunsch and Ferrari (2004) for a comprehensive overview of sources and sinks of energy in the ocean). In their view, the circulation, now driven by mechanical energy sources (wind and tides), builds up potential energy that is released from the deep convection regions when the stratification there has become unstable. Instead of a heat engine, the circulation is then better described as a pump and release valve system (Samelson 2004).

The exact link between deep convection and the AMOC is subject to an ongoing debate in the scientific community. Apart from the energy source discussion, a second debate is on where the water sinks. Sinking has long been considered to coincide with deep convection. However, a net downward velocity in the ocean interior, i.e. away from topographic boundaries, has to be accompanied by very large horizontal velocities. Such currents have not been observed in the Labrador Sea (Spall and Pickart 2001). On the other hand, convectively-formed water masses are found to spread and set the density structure at mid-depth (Talley and McCartney 1982) and are thus at the heart of this circulation.

Despite these open questions, there is a widespread consensus that deep convection and the AMOC are linked. As Kuhlbrodt et al. (2007) describes in a recent review, deep convection affects the strength and shape of the overturning cell. Also, models show a strong correlation between deep water formation in the Labrador Sea and the strength of the AMOC on interannual to decadal timescales (Eden and Willebrand 2001, Biastoch et al. 2008). Variability in deep convection thus affects the AMOC, and understanding variability in deep convection is therefore one of the keys to understanding variability in the AMOC and its impacts on the climate system.

1.2 General deep convection theory

Open ocean deep convection sites are known for their harsh climatic winter conditions. For decades, the understanding of this process was therefore mostly based on indirect observational evidence from the spreading of water masses. The MEDOC experiment (MEDOC-Group 1970) provided the first direct *in situ* observations of deep convective mixing in the ocean. Together with laboratory experiments, theoretical studies, and later other *in situ* observational studies and numerical simulations our understanding of the the deep convection process has been greatly enhanced.

Although the details, and even the driving mechanisms, of the deep convection process are different for different convection sites, it can generally be subdivided into three stages (Marshall and Schott 1999). First, preferred sites for deep convection have as a common feature a gyre-scale cyclonic circulation and an accompanying (upward) doming of isopycnals (Figure 1.1a). This process brings the abyssal weakly stratified water closer to the surface. During late autumn and early winter, the now thin layer of strongly stratified water is eroded by the increasingly large buoyancy loss to the atmosphere. This exposes the weakly stratified water underneath to the cold atmosphere. This first stage is referred to as 'preconditioning'.

During the second half of the winter the large heat (and thus buoyancy) loss to

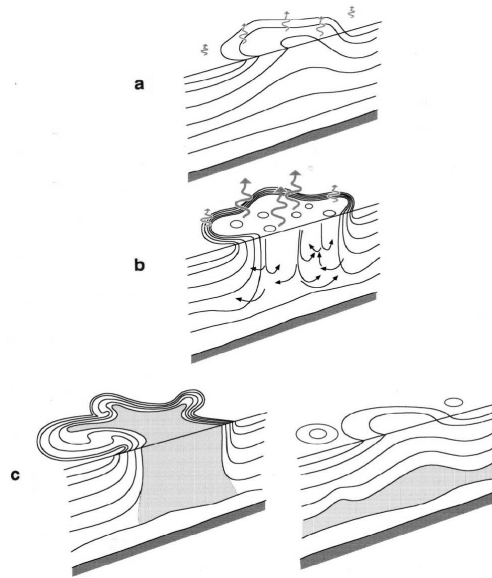


Figure 1.1: Theoretical stages of open ocean deep convection from Marshall and Schott (1999). (a) Preconditioning; (b) Deep convection; (c) Lateral exchange and spreading.

the atmosphere induces deep convection in very localized 'plumes' of order 1 km in diameter (Figure 1.1b). In these plumes downward velocities of up to 10 cm s^{-1} are measured. The large downward motion in the plumes is however compensated by smaller but more widespread upward velocities surrounding the plumes, giving little net downward flux of water. Instead, the main result of deep convection is vertical homogenization of heat and salt in the plumes.

During and after the deep convection phase, rapid lateral mixing with the surrounding water creates an area of dense water, known as a 'chimney' (MEDOC-Group 1970) or a 'mixed patch' (Marshall and Schott 1999). Around this chimney, between the dense water in the convected area and the stratified, lighter water surrounding it, a rim current develops in geostrophic balance with the lateral density gradient. This rim current then becomes baroclinically unstable and, by shedding eddies of stratified water into the chimney and eddies containing convected water into the surroundings, it mixes the water in the convection site and restratifies the ocean (Figure 1.1c).

1.3 Water masses in the Atlantic Ocean

Dense water mass formation through deep convection, as described in the previous section, only occurs in a few specific locations in the world ocean (Marshall and Schott 1999). Apart from the Labrador Sea, deep and intermediate water masses are also formed off Antarctica (AntArctic Bottom Water), in the Mediterranean Sea (Mediterranean Sea Outflow Water) and in other locations in the North Atlantic subpolar gyre (North Atlantic Deep Water, NADW). The way in which these water masses set the density structure of the Atlantic Ocean is illustrated in Figure 1.2.

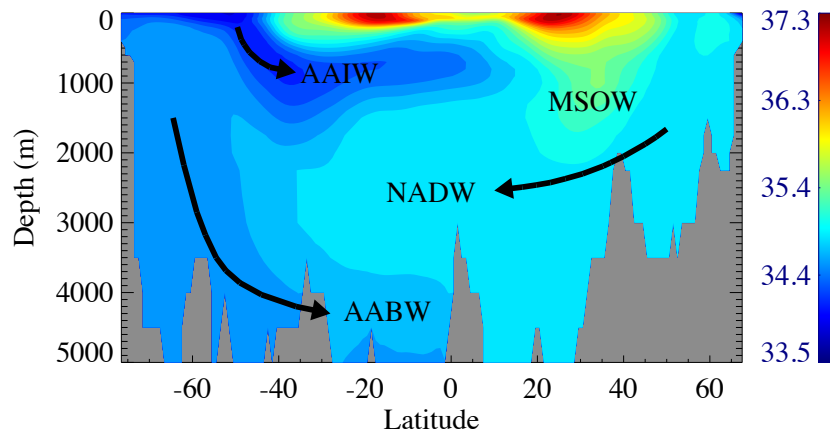


Figure 1.2: Salinity section of the Atlantic Ocean at 30°W from the World Ocean Atlas, showing the main intermediate and deep water masses. NADW = North Atlantic Deep Water; MSOW = Mediterranean Sea Outflow Water; AABW = AntArctic Bottom Water; AAIW = AntArctic Intermediate Water.

The term NADW is used for the combination of dense water masses formed in the subpolar North Atlantic Ocean (Figures 1.2 and 1.3). The densest water masses are formed in the northeastern part of the subpolar gyre in the Greenland-Iceland-Norwegian Seas (GIN Seas). Spreading of these water masses into the Atlantic is inhibited by the shallow Greenland-Iceland-Scotland ridge. This ridge is shallower than 500 m except for two narrow, relatively shallow straits. Through Denmark Strait, the northernmost one, between Greenland and Iceland, the densest and coldest water mass of the region (Denmark Strait Overflow Water, DSOW) flows over the sill down into the deep ocean on the western side of the ridge. Similarly, Iceland Scotland Overflow Water (ISOW) flows through the southern gap between Iceland and Scotland. The water mass is modified through mixing with other water masses

(therefore its name is changed into NorthEast Atlantic Deep Water, NEADW) and ultimately merges with the DSOW to form the Deep Western Boundary Current, which transports these dense water masses to the Labrador Sea (Figure 1.3).

The second deep convection site for NADW is the Labrador Sea itself, between Greenland and the Canadian east coast. Here, Labrador Sea Water (LSW) is formed (see section 1.4 for a more detailed description). LSW is also formed east of Greenland in the Irminger Sea and south of Greenland (Pickart et al. 2003), but the Labrador Sea is the primary formation site. Modeling studies (e.g. Eden and Willebrand 2001, Biastoch et al. 2008) indicate that especially variability in the formation of LSW can have a large impact on the variability of the large scale overturning circulation in the ocean. Therefore, the focus of this dissertation is on the variability of LSW formation.

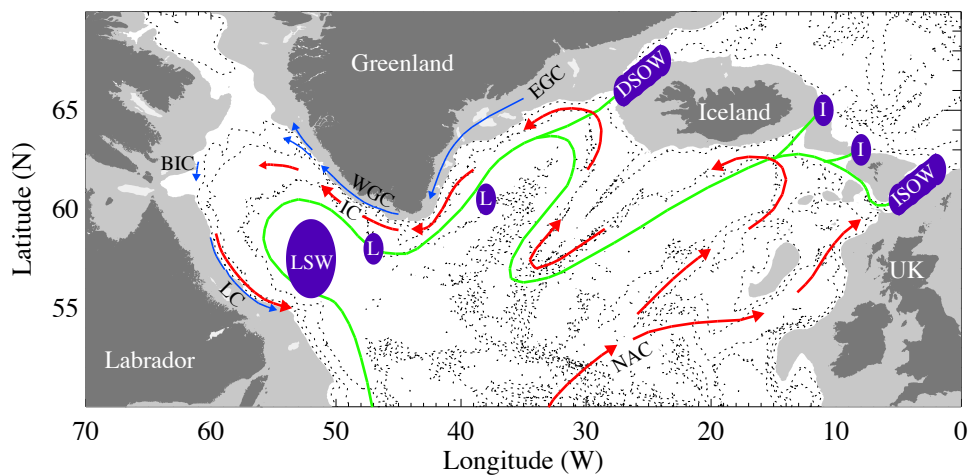


Figure 1.3: Map of the subpolar gyre. Areas shallower than 500 m are shaded in pale gray, continents are shaded in dark gray. Red arrows indicate warm and saline surface currents, while blue arrows indicate cold and fresh surface currents. Deep currents are indicated in green. Purple ellipses are deep convection areas and overflow regions. LSW = Labrador Sea Water formation site; L = secondary Labrador Sea Water formation site; DSOW = Denmark Strait Overflow Water region; ISOW/I = Iceland Scotland Overflow Water region. NAC = North Atlantic Current; EGC = East Greenland Current; IC = Irminger Current; WGC = West Greenland Current; BIC = Baffin Island Current; LC = Labrador Current.

1.4 Labrador Sea Water formation

The Labrador Sea is the westernmost basin of the subpolar North Atlantic gyre (Figure 1.3). It is a semi-enclosed basin, bounded by Canada on the western side and Greenland along the northeastern margin. In the north the Labrador Sea borders Davis Strait, a shallow (ca 700 m deep) connection with the Arctic Ocean. In the southeast it has an open connection with the Atlantic Ocean. The maximum water depth in the Labrador basin is about 4500 m in the southeastern part. This rapidly decreases across the continental slope to about 200 m on the continental shelves.

To understand the variability in LSW formation, one needs to consider both the atmospheric conditions and the oceanic characteristics. The oceanic characteristics in the interior are determined by lateral interaction with the boundary currents and, in case of wintertime deep convection, rapid vertical mixing during the convection season (February to April in the Labrador Sea case). The structure of the boundary currents and the resulting hydrographic structure of the central Labrador Sea are discussed in section 1.4.1. Then the prevailing atmospheric conditions are outlined in section 1.4.2. This section concludes with an overview of the observed variability of LSW formation in section 1.4.3.

1.4.1 Hydrographic characteristics of the Labrador Sea

The Labrador Sea is characterized by a system of boundary currents encircling a more quiescent interior domain. Both the boundary currents and the water in the interior show several distinct layers with very different temperature and salinity characteristics, depending on the origin of the water mass they carry. The following gives an overview of these different water masses.

The boundary current system

The upper part of the Labrador Sea is surrounded by buoyant boundary currents (Figures 1.3 and 1.4). This boundary current system has roughly two components. The lightest one brings in fresh and cold water from Arctic origin, while the denser one brings in relatively warm and saline water from subtropical origin. The Arctic water mostly comes in via the southern tip of Greenland (Figure 1.3), where the East Greenland current continues as the West Greenland Current on the West Greenland continental shelf. The West Greenland Current follows the bathymetry to the northern edge of the Labrador Sea, where it splits into a part that continues northward to Davis Strait and a part that flows westwards towards the Canadian coast. There it is joined by the Baffin Island Current, which in turn is fed by fresh water from the Canadian Archipelago and Baffin Bay.

The current system which brings in subtropical water starts southeast of the Labrador Sea in the North Atlantic Current (Figure 1.3), which is the extension of the Gulf Stream. The North Atlantic Current splits south of Iceland into one part which continues north into the GIN seas, and one part which follows the bathymetry around the Irminger Sea to the southern tip of Greenland. There it subducts and follows the continental slope obliquely underneath the West Greenland Current (Figure 1.4). It is guided westward by the bathymetry around the northern edge of the Labrador Sea towards the Canadian coast, where it merges with the West Greenland Current and the Baffin Island Current to form the Labrador Current.

The lower part of the Labrador Sea is surrounded by the Deep Western Boundary Current. As discussed in section 1.3, this current carries DSOW and NEADW, which are formed through convective densification in the GIN Seas and modified through mixing with other water masses on their way to the Labrador Sea. A more comprehensive description of the deep currents and water masses east of the Labrador Sea can be found in Yashayaev and Dickson (2008).

Hydrography of the central Labrador Sea

The stratification of the central Labrador Sea strongly reflects the vertical structure of the boundary current system. There are roughly five characteristic water masses (Figure 1.4). The upper ca 200 m is fed by the fresh and cold currents on the continental shelves. Although this layer is cold in winter, summertime solar insolation increases the upper layer temperature over the remainder of the year. Between ca 200 m and 800 m depth a layer of relatively warm and saline Irminger Water is found, which is fed by the subsurface Irminger Current in the east and the warm and saline part of the Labrador Current in the west. These upper two layers are mixed almost every winter through convection, but during spring and summer they regain the boundary current structure. If the deep convection reaches sufficiently deep, the layer of LSW is reached (typically between ca 800 m and 1500 to 2000 m), which consists of the remaining LSW formed in previous winters. If this happens, the LSW is said to be 'ventilated', i.e. exposed to the atmosphere. The combination of the water properties of the water being mixed, additional lateral mixing and atmospheric forcing determine the properties of the newly-formed LSW. It is these properties that enable oceanographers to trace LSW away from its formation site (e.g. Molinari et al. 1998). Last, the abyssal Labrador Sea is occupied by NEADW and DSOW (Figure 1.4). These layers have little impact on the variability of LSW formation, although the former water mass occasionally affects the LSW properties when deep convection reaches this layer. Such deep convection is, however, very rare (Straneo 2006b).

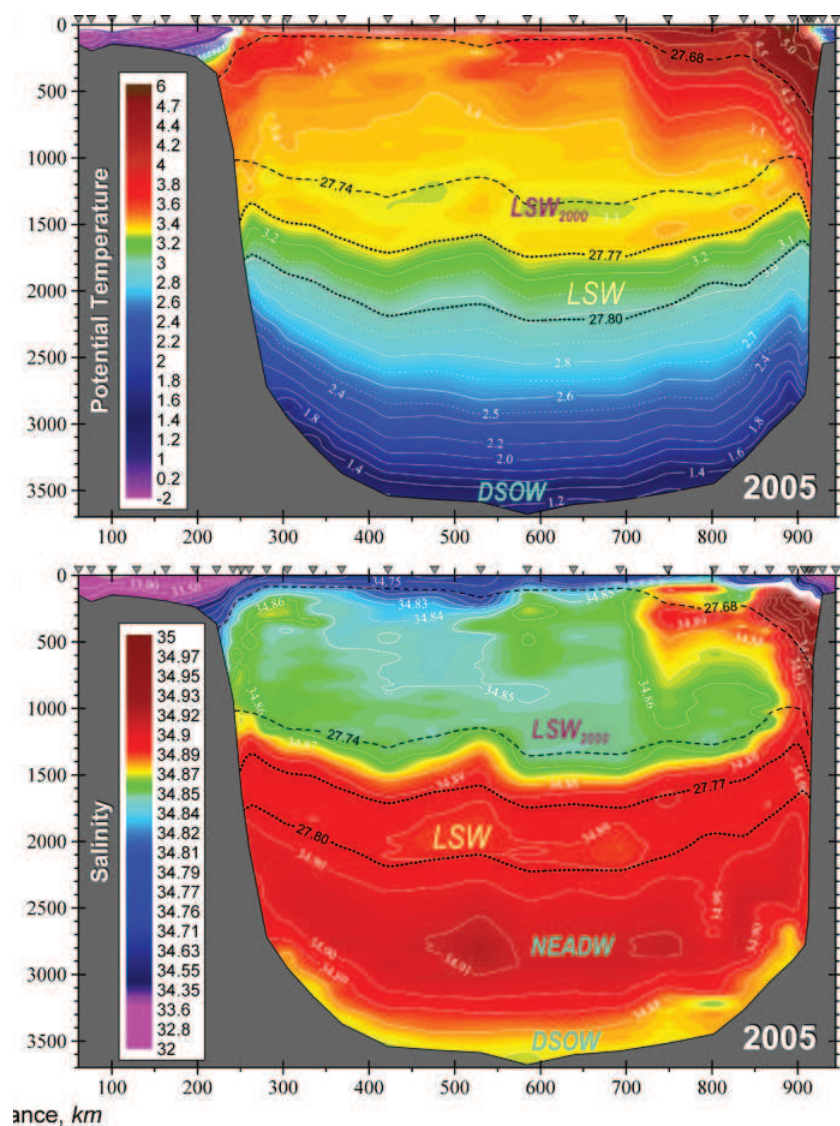


Figure 14: Hydrography of the Labrador Sea along the WOCE AR7W section from Yashayaev (2007) showing potential temperature (upper panel) and salinity (lower panel). LSW = Labrador Sea Water; LSW₂₀₀₀ = Labrador Sea Water formed in 2000; NEADW = NorthEast Atlantic Deep Water; DSOW = Denmark Strait Overflow Water. The black lines are isopycnals.

1.4.2 Prevailing atmospheric conditions

Deep convection is forced at the ocean-atmosphere interface by surface buoyancy fluxes, the magnitude of which depend on the oceanic and atmospheric conditions (see also chapter 3). There are two types of surface buoyancy fluxes: surface heat fluxes and surface fresh water fluxes. The latter, which is the net effect of precipitation, evaporation and runoff, is very small in the Labrador Sea (Myers and Donnelly 2008) and moreover adds buoyancy to the ocean and thus counteracts deep convection. The wintertime surface heat flux, on the other hand, is very large and the primary driver of deep convection. The atmospheric quantities that have a large effect on the magnitude of the surface heat flux are the air temperature, wind strength and humidity. These are briefly discussed below.

The Labrador Sea area is characterized by very harsh winters. This is illustrated in Figure 1.5, which shows the ERA40 air temperature averaged over February and March, which is generally the coldest time of the year, and averaged over an area in the central Labrador Sea where deep convection is known to occur. The 41-year mean February-March average air temperature is -0.7°C . The lowest monthly mean temperature in this time series is -6.1°C (December 1983). The air temperature is very variable however, and 6-hourly values drop below -10°C in most winters, and can be as low as -19.3°C .

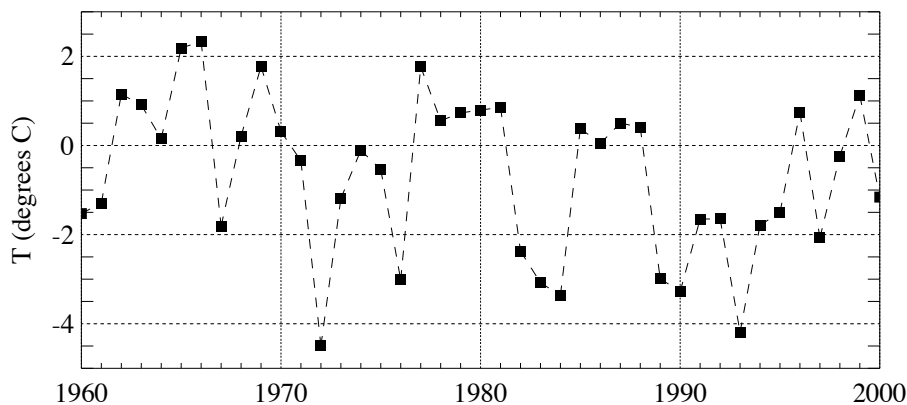


Figure 1.5: Average February-March air temperature in the central Labrador Sea area at 2 m height (from the ERA40 reanalysis, averaged over 55N-60N and 55W-50W).

The cold air is advected into the region from the North American continent by the prevailing northwesterly winds (Figure 1.6). Both the large wind speed and the characteristics of the air advected by the wind (cold and dry) induce large surface

buoyancy fluxes from ocean to the atmosphere and make the Labrador Sea susceptible to deep convective mixing. Note in both Figure 1.5 and in Figure 1.6 the substantial year-to-year variability.

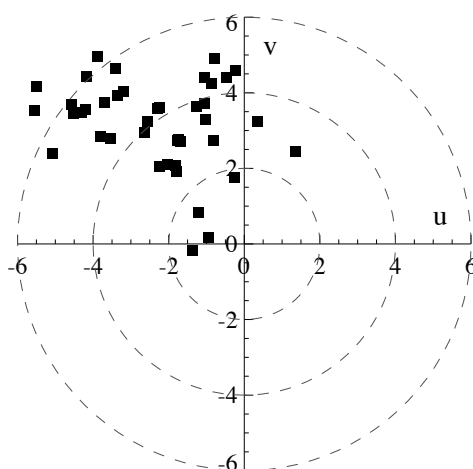


Figure 1.6: Average February-March wind speed and direction in the central Labrador Sea at 10 m height (from the ERA40 reanalysis, averaged over 55N-60N and 55W-50W). The plot shows the direction where the wind is coming from (mostly northwesterly winds). The circles indicate an absolute wind speed of 2, 4 and 6 m/s.

In literature on deep convection in the Labrador Sea, the North Atlantic Oscillation index (NAO; Hurrell 1995) is often used as an indicator for the atmospheric winter conditions. The NAO index is defined as the normalized sea level pressure difference between the Azores and Iceland. A high NAO index therefore means stronger westerlies and thus a larger chance of deep convection in the Labrador Sea. Although there is certainly a correlation between the NAO index and the convective activity in the Labrador Sea (Dickson et al. 1996, Curry et al. 1998, Yashayaev 2007), there is no one-to-one relationship. This can be either due to atmospheric conditions such as the position of the storm tracks (Våge et al. 2009) as well as oceanic conditions, such as a low surface salinity (Dickson et al. 1988).

1.4.3 Observed variability in Labrador Sea deep convection

Several dedicated *in situ* monitoring programs (see section 4.2 for a more elaborate description of the *in situ* observations) have recorded a substantial interannual to decadal variability in LSW formation over the past decades (Curry et al. 1998, Yashayaev 2007). Since 1970 (Figure 1.7), four multi-year periods of LSW formation can be distinguished: the early to mid 1970s, the early 1980s, the late 1980s to early 1990s, and the early 2000s. The volume and properties of the water masses formed during these periods also shows a large variability. Deep convection in the early 1990s was by far the deepest and has formed the coldest class of LSW in this observational record (Yashayaev and Loder 2009). Single-year convection periods also occur, a well monitored example of which is 2008 (Våge et al. 2009). In between successive deep-convection periods, convective mixing to shallower depths is observed. The most extreme example was in the late 1960s and early 1970s, when convection was restricted to the upper 200 meters (visible at the very left-hand side of the figure and discussed in detail in chapter 3).

1.5 Outline of the dissertation

This introductory chapter served to explain the importance of the variability in the formation of Labrador Sea Water, and the lack of understanding of this variability. The aim of this dissertation is to go beyond the general correlation with the NAO index and to study the impact of some of the oceanic processes on this variability in detail. Furthermore, the feasibility of monitoring LSW formation using satellite altimetry measurements will be assessed.

The first process study (chapter 2) deals with the impact of different eddy types on the restratification process after deep convection. Mesoscale eddies are known to be primary agents of restratification in the Labrador Sea, but the roles different types of eddies play in this process are not yet clear. "What is the contribution of different eddy types to the restratification process after deep convection?" is the main question in chapter 2. Using an idealized model of the region, these roles are investigated and quantified.

In the second process study (chapter 3) the effects of a low surface salinity on deep convection are investigated. It is generally known that a low surface salinity can severely limit the convection depth. But how does this work? Which processes important for the occurrence of deep convection are impacted by a low surface salinity? For a well-monitored case in the 1960s and early 1970s, these questions are addressed in chapter 3. Thus, in contrast to chapter 2 where a model is the main tool, an observational perspective with *in situ* data is used in this chapter.

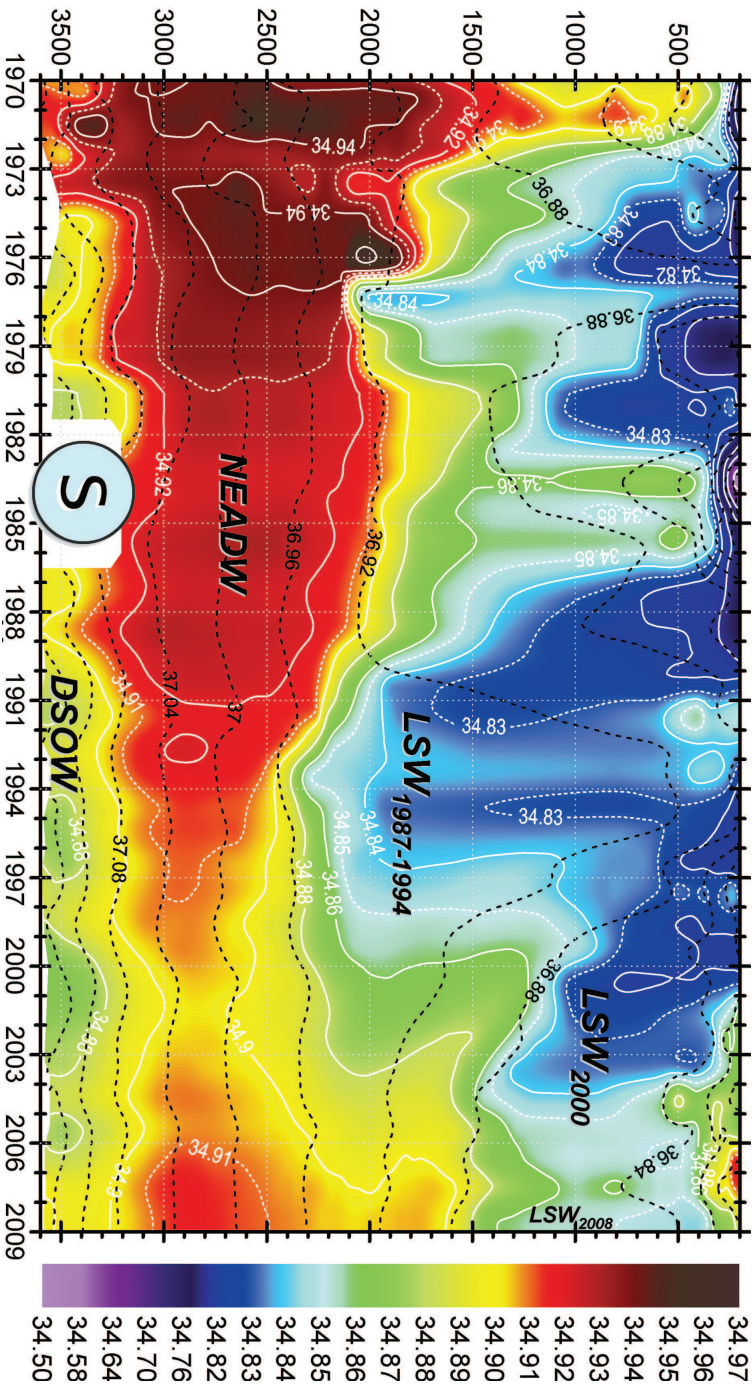


Figure 1.7: Observed vertical salinity distribution (color) between 1970 and 2009 in the central Labrador Sea from Yashayaev and Loder (2009), showing the variability in LSW formation over this period. $LSW_{1987-1994}$ = Labrador Sea Water formed in the winter of 1987 to 1994; LSW_{2000} = LSW formed in 2000; LSW_{2008} = LSW formed in 2008; NEADW = NorthEast Atlantic Deep Water; DSO = Denmark Strait Overflow Water. The black dashed lines indicate the potential density anomaly referenced to 2000 db.

Apart from understanding how different factors impact the variability of LSW formation, it is also important to monitor this variability. However, the harsh winter conditions in the Labrador Sea area pose serious constraints on the feasibility of doing *in situ* observations. Also, *in situ* observations are severely limited in their temporal and spatial coverage. A way to circumvent these problems is to use satellite altimetry in the monitoring program. Although possible in theory, this is not a straightforward procedure. The opportunities for detecting and monitoring the formation of Labrador Sea Water using satellite altimetry are discussed in chapter 4.

Last, in chapter 5 the main results from this dissertation are summarized. This chapter also contains an overview of still open questions on issues that require further attention in future work.

This chapter is based on work published as: R Gelderloos, C.A. Katsman and S.S. Drijfhout – “Assessing the Roles of Three Eddy Types in Restratifying the Labrador Sea after Deep Convection,” *Journal of Physical Oceanography*, vol. 41, pp. 2102–2119, 2011.

Chapter 2

The Roles of Three Eddy Types in Restratification after Deep Convection

We are travelers on a cosmic journey, stardust, swirling and dancing in the eddies and whirlpools of infinity.

Paulo Coelho, *The Alchemist*

Abstract

Restratification after deep convection is one of the key factors in determining the temporal variability of dense water formation in the Labrador Sea. In the subsurface it is primarily governed by lateral buoyancy fluxes during early spring. The roles of three different eddy types in this process are assessed using an idealized model of the Labrador Sea that simulates the restratification season. The first eddy type, warm-core Irminger Rings, is shed from the boundary current along the west coast of Greenland. All along the coastline the boundary current forms Boundary Current Eddies. The third type, Convective Eddies, arises directly around the convection area. In the model, the latter two eddy types are together responsible for replenishing 30% of the winter heat loss within six months. Irminger Rings add another 45% to this number. Our results thus confirm that the presence of Irminger Rings is essential for a realistic amount of restratification in this area. The model results are compared to observations using theoretical estimates of restratification time scales derived for the three eddy types. The time scales are also used to explain contradicting conclusions in previous studies on their respective roles.

2.1 Introduction

Labrador Sea Water (LSW) is one of the main mode waters in the North Atlantic Ocean (Lazier 1973, Lazier et al. 2002). It is formed in winter by deep convection (Clarke and Gascard 1983, LabSeaGroup 1998), facilitated by the harsh climatic conditions in this region and the regional ocean circulation (Marshall and Schott 1999). It spreads southwards and eastwards into the North Atlantic Ocean and beyond, where it partly sets the density structure at intermediate depths (Bower et al. 2009). As such it also contributes to the variability in the global meridional overturning circulation (Eden and Willebrand 2001, Yashayaev 2007, Biastoch et al. 2008).

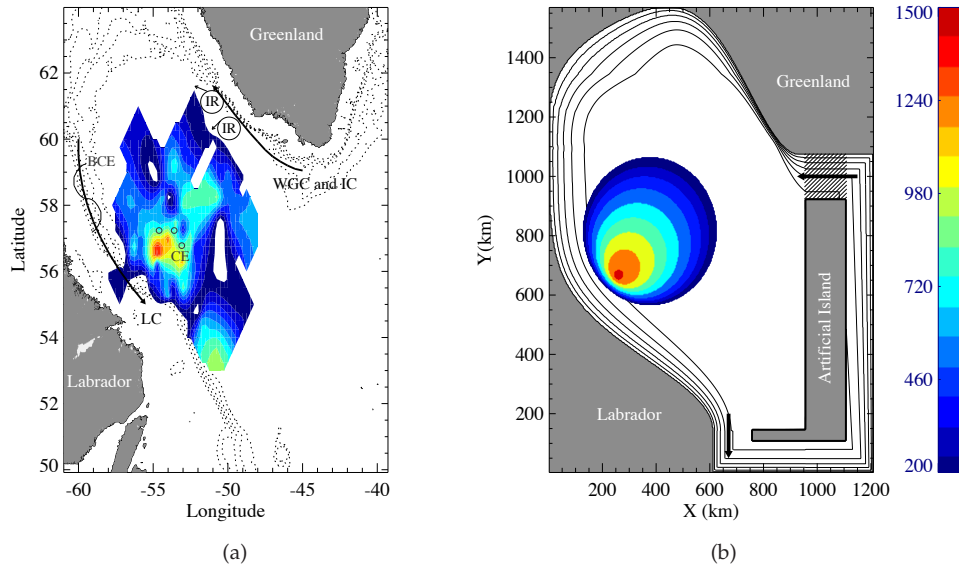


Figure 2.1: (a) Map of the Labrador Sea, with a schematic representation of the boundary current and the three eddy types (WGC West Greenland Current, IC Irminger Current, LC Labrador Current, IR Irminger Ring, BCE Boundary Current Eddy, CE Convective Eddy). The dashed lines are the 500 to 2500 m isobaths (contour interval of 500 m). The mixed layer depth in the winter of 1997 is shaded in color (Pickart et al. 2002). (b) Model domain and idealized bathymetry (contour interval is 500 m). The domain shape is roughly based on the 1000 m isobath in (a) to exclude the shelves. A boundary current is forced at the southern tip of Greenland by restoring conditions for temperature and velocity, applied in the shaded area. The L-shaped island in the southeast guides the flow back towards the restoring region. The mixed layer depth in the idealized convection area is shaded in color.

Besides wintertime atmospheric conditions, one of the key processes that determine the interannual and interdecadal variability of LSW formation (Dickson et al. 1996, Lazier et al. 2002, Kieke et al. 2007, Yashayaev 2007) is restratification after deep convection¹. The process is governed both by warming due to solar radiation in summer and lateral influx of heat from the boundary current. On average, about 60% of the total annual heat input over the upper 1600 m is provided by lateral

¹In periods of low convective activity, multi-year restratification is also important. That is however beyond the scope of this study where we focus on the restratification immediately after a deep convection winter.

heat fluxes (Yashayaev and Loder 2009), but solar radiative warming is limited to the upper 200 m (Straneo 2006a). Furthermore, the fact that restratification already starts when the atmosphere is still cooling the ocean in early spring (generally in April) (Lilly et al. 1999, Avsic et al. 2006, Yashayaev and Loder 2009) and that it occurs rapidly over a large depth (Lilly et al. 1999, Avsic et al. 2006) indicates an important role of lateral heat fluxes in restratification. In this study we therefore focus on the dynamics of the oceanic part of restratification (lateral fluxes) by ignoring solar radiative forcing.

The characteristics of the boundary current strongly affect restratification. Lateral fluxes (Figure 2.1a) adjust the water properties in the central Labrador Sea towards the properties of the very buoyant boundary current (Straneo 2006a). The boundary current water on the shelf is of Arctic origin and is hence cold and fresh. On the continental slope, it is of subtropical origin, and therefore relatively warm and saline. Both water masses supply low-density water to the interior Labrador Sea.

Early studies on restratification after deep convection focused on the efficiency of buoyancy exchange across a front (Jones and Marshall 1993, Maxworthy and Narimousa 1994, Jones and Marshall 1997, Legg et al. 1998). At the front surrounding the convection area a rim current develops, which becomes baroclinically unstable and generates small eddies with a size on the order of the Rossby deformation radius. These eddies exchange properties across the front and restratify the convection area. As they are formed as a result of deep convection, we will refer to them as Convective Eddies (CE), following Chanut et al. (2008).

After the Labrador Sea Experiment in the 1990's (LabSeaGroup 1998) it became clear that the boundary current acts as a major source of buoyancy for the replenishment of the dense water mass in the convected area (Lilly et al. 2003). The buoyant water is brought into the interior by lateral eddy fluxes (Spall 2004, Katsman et al. 2004, Straneo 2006b), while the dense convected water is exported out of the Labrador Sea in the boundary current (Straneo 2006b, Brandt et al. 2007).

This process is captured in a conceptual model by Straneo (2006b). With this model the restratifying effect of eddies originating from the boundary current was investigated. The results of the conceptual model agree nicely with in situ measurements, indicating that restratification in the interior Labrador Sea is indeed primarily caused by eddy-driven interior-boundary current exchange. However, Straneo (2006b) did not distinguish between the contributions of different eddy types to the exchange.

There are two distinct pathways by which eddies may flux buoyancy from the boundary current into the interior. The first mechanism is a buoyancy flux associated with baroclinic eddies that form at the density front between the warm bound-

ary current and the cold interior. Like CEs the size of these eddies is on the order of the Rossby radius of deformation, but contrary to CEs these eddies are present year round. Following Chanut et al. (2008), this eddy type will be referred to as Boundary Current Eddies (BCE).

Second, large eddies (15 to 30 km radius) are shed from the boundary current along the west coast of Greenland (Figure 2.1a). These eddies are referred to as Irminger Rings (IR) because of their warm and saline Irminger Water core (Lilly and Rhines 2002, Lilly et al. 2003, Hatun et al. 2007). The formation of these eddies is triggered by a steepening of the slope along a portion of the western Greenland coast (Bracco and Pedlosky 2003, Wolfe and Cenedese 2006) (Figure 2.1a). At the downstream end of this steep slope a large eddy kinetic energy signal is detected (Prater 2002, Lilly et al. 2003, Brandt et al. 2004). IRs form spontaneously in model simulations configured with such a steep slope (Eden and Böning 2002, Katsman et al. 2004, Chanut et al. 2008), while their formation can be suppressed by defining a more gentle slope for the simulation (Katsman et al. 2004, Chanut et al. 2008). Although IRs are only formed in a localized region in the eastern side of the basin, the eddies are very energetic and long-lived (Lilly et al. 2003). They travel southwestwards into the Labrador Sea interior, allowing them to bring buoyant boundary current water to the area of deep convection.

The possibility to eliminate IRs from a model simulation by changing the bathymetry pattern allows a systematic investigation of their role in restratification. Katsman et al. (2004) performed two 6-month spindown simulations of the restratification season in the Labrador Sea, one with and one without IRs, in an idealized regional configuration. Based on the very slow restratification in the case where IRs were absent it was concluded that these eddies were the dominant contributors to restratification in this area. The authors only considered the contribution of CEs and IRs however, because the boundary current was too stable for BCEs to form. Chanut et al. (2008) used two 10-year equilibrium simulations in a realistic configuration to investigate the effects of CEs, BCEs and IRs on restratification. In contrast to Katsman et al. (2004), they concluded that BCEs make the dominant contribution. Because both of their simulations reached a quasi-equilibrium state, with winter-time convection and restratification over summer, and with a similar lateral heat flux into the interior, the authors concluded that the presence of IRs is not crucial for restratification.

The two equilibria in the Chanut et al. (2008) study are however very different. As at least one of the equilibria does not resemble the actual situation, the observation that the heat flux into the interior is the same does not justify conclusions on the lateral heat flux mechanisms in the real Labrador Sea. In contrast, simulations of a single restratification season can be started from the same realistic end-of-winter

state. The efficiency of different eddy types can be assessed by their ability to adjust this end-of-winter state to a realistic end-of-summer state within one restratification season. In this study we use this approach to address the question which eddy type dominates the lateral heat flux and we explain the opposing conclusions from previous studies.

The model configuration used in this study is described in Section 2.2, as well as the initial state of the model fields, the general characteristics during the spindown simulations, and a description of the simulated cases. In Section 2.3 the model results are discussed with respect to the rate of restratification. In Section 2.4 scalings are derived for the time scale of restratification for the different eddy types, which are used in Section 2.5 to compare the results from this study with results from earlier work. A summary of the results and conclusions is given in Section 2.6.

2.2 Model and initial state

In this study we used an idealized regional model for the Labrador Sea discussed below. Despite its simplicity, the model reproduced the hydrographic properties and the eddy field in the Labrador Sea well. To assess the effect of the different eddy types on restratification, three spindown simulations were performed where one or more eddy types were eliminated.

2.2.1 Model configuration

The simulations in this study were performed with the MIT primitive equation model (Marshall et al. 1997) in an idealized regional configuration for the Labrador Sea (Figure 2.1b). The configuration was similar to the one used in Katsman et al. (2004), but the basin shape was improved and the location of the convection area was, more realistically, in the southwestern Labrador Sea.

The basin (Figure 2.1b and Table 2.1) had a maximum depth of 3000 m, which decreased towards the boundaries to form a slope along the perimeter of the basin. Possible interactions with the Arctic via the Davis Strait have been neglected and deep boundary currents and the continental shelved were omitted. Note the steepening of the slope along the west coast of Greenland, which has been shown to be essential for the shedding of IRs (Section 2.1). The horizontal grid spacing was 3.75 km in both zonal and meridional directions. This is well below the Rossby radius of deformation (about 7 km in this area), so that the model is eddy resolving. In the vertical the model consisted of 15 layers with layer thickness ranging from 100 m in the upper layers to 450 m near the bottom. In the simulations, only the influence of temperature was assessed, neglecting the role of salinity for simplicity. A

linear equation of state $\rho = \rho_0 (1 - \alpha T)$ was used, with a reference density ρ_0 and a constant thermal expansion coefficient α . The use of a linear equation of state with temperature alone can be justified because the density of sea water is temperature dominated in the restratification season. The values of parameters used in the numerical simulations are given in Table 2.1.

A boundary current was formed by restoring temperature and zonal velocity south of the southern tip of Greenland (gray shaded area in Figure 2.1b), from where it continues cyclonically around the basin. The restoring conditions were applied over the full depth of the channel with a very short restoring time scale (40 minutes) to form a zonal flow in geostrophic balance (Katsman et al. 2004):

$$T(y, z) = T_{ref}(z) + \frac{\Delta\rho}{2\alpha\rho_0} \left(1 - \frac{z}{z_b}\right) \left[1 + \tanh\left(\frac{y - y_0}{L_y}\right)\right] \quad (2.1)$$

$$U(y, z) = \frac{g\Delta\rho}{4L_y f \rho_0} \frac{(z - z_b)^2}{z_b} \frac{1}{\cosh^2\left(\frac{y - y_0}{L_y}\right)} \quad (2.2)$$

where $T_{ref}(z)$ is the temperature profile at the start of the spinup (based on the average density profile from a summer occupation over the southwestern part of the AR7W hydrographic section; Katsman et al. 2004). The density difference across the boundary current ($\Delta\rho$) and the boundary current width (L_y) determine the maximum boundary current velocity. z_b is the bottom depth, and y_0 is the meridional position of the maximum current speed, measured in distance from the south coast of Greenland. g is the acceleration due to gravity and f the Coriolis parameter. The parameter values (Table 2.1) were chosen such that the resulting boundary current has the properties seen in the AR7W hydrographic observations. The total transport in the boundary current was 17 Sv, in line with observational estimates (Cuny et al. 2002, Dengler et al. 2006, Fischer et al. 2010) (not taking into account deep currents associated with overflow waters not represented in this model). The maximum current velocity is 0.56 m s^{-1} , in good agreement with the observed velocity over the upper continental slope from surface drifter measurements (Cuny et al. 2002).

The use of open boundaries has been avoided by directing the boundary current behind an artificial island in the southeast of the domain, from the southern Labrador coast back to the restoring region south of Greenland (Spall 2007). One IR bounced against this artificial island in one of the simulations, but as this was far away from the convection region it did not noticeably influence the results. The restoring conditions induce a continuous warming of the basin, but this is small over the limited period of the restratification season ($0.06 \text{ }^\circ\text{C}$ averaged over the interior basin in six months). The restoring conditions are the only forcing in the model; no surface fluxes are applied in any of the simulations.

basin width (zonal)	945 km
basin length (meridional)	1417.5 km
channel width	112.5 km
horizontal eddy viscosity	$0.9 \times 10^8 \text{ m}^4 \text{ s}^{-1}$
horizontal diffusion coefficient	$0.5 \times 10^8 \text{ m}^4 \text{ s}^{-1}$
vertical eddy viscosity	$1.0 \times 10^{-5} \text{ m}^2 \text{ s}^{-1}$
vertical diffusion coefficient	$1.0 \times 10^{-5} \text{ m}^2 \text{ s}^{-1}$
ρ_0	1028 kg m^{-3}
α	$2.0 \times 10^{-4} \text{ }^\circ\text{C}^{-1}$
$\Delta\rho$	-0.26 kg m^{-3}
L_y	22.5 km
y_0	22.5 km
f	$1.26 \times 10^{-4} \text{ s}^{-1}$
g	9.81 m s^{-2}

Table 2.1: Standard parameter values.

2.2.2 Setting the initial state

Earlier idealized model studies of restratification after deep convection (Jones and Marshall 1997, Send and Käse 1998, Katsman et al. 2004) prescribed a convection region by specifying the initial density field in their simulations and an ocean at rest. However, these studies did not consider the effect of the presence of a boundary current. In order to do so, it is necessary to perform a spinup simulation first to let the warm boundary current encircle the basin and to let the eddy field develop. Once the circulation has spun up, the density field can be altered offline to prescribe a convection region representing the situation at the end of winter. In this way, all simulations of the restratification season can be started from nearly² the same conditions.

Figure 2.2 shows a zonal cross section of the temperature and meridional velocity at $y = 1150 \text{ km}$ averaged over the last month of the spinup phase. Because the influence of salinity is neglected, the low density of the cold and fresh surface waters is represented as a warm top layer. The boundary current flows northwards along the west coast of Greenland and returns on the Canadian side in southern direction. The southward-flowing boundary current in the west is much weaker and wider and has lost part of its heat to the interior due to eddy activity. On both sides of the

²At the end of the spinup phase, the temperature field in the interior displayed only minor differences between the spinup simulations with and without IRs. As a consequence, the amount of heat removed from the basin by constructing the convection region differs by about 1%.

basin, the density and velocity structure of the boundary current compare favorably with observations (Cuny et al. 2002, Pickart and Spall 2007).

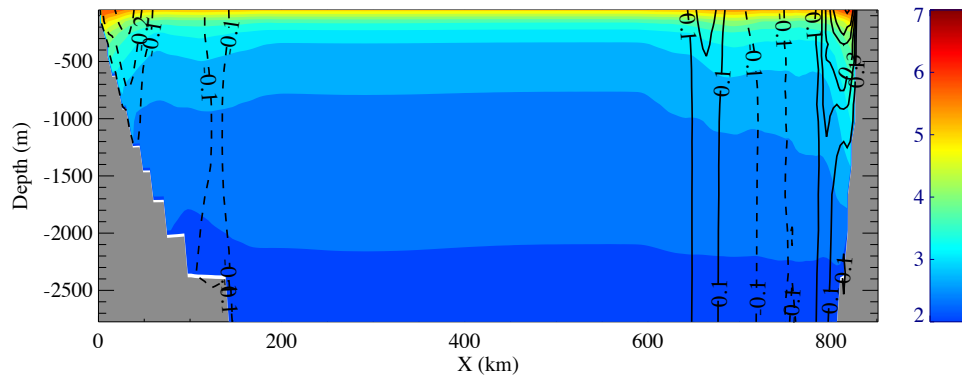


Figure 2.2: Zonal cross section of the basin at $y = 1150$ km, time-averaged over the last month of the 6 month spin-up phase. Temperature ($^{\circ}\text{C}$) is shaded in color and the meridional velocity is overlaid (contour interval is 0.1 m s^{-1} , dashed represents southward flow). The Canadian (Greenland) side is on the left (right).

After the spin-up phase an idealized convection region was constructed synthetically by altering the temperature field of the final state of the spin-up simulation offline. The prescribed convection region (Figure 2.1b) has a spatially varying mixed layer in the shape of a skewed cone, with characteristics similar to the end-of-winter data published by Pickart et al. (2002) (their Figure 12d, reproduced in Figure 2.1a). At each grid point inside the skewed cone, the temperature throughout the mixed layer is set equal to the temperature found at the base of the local prescribed mixed layer. The temperature field outside the convection region is unaltered (Figure 2.3).

We also studied the dependence of the restratification rate on the chosen shape of the convection area. The density gradient across the front was varied by changing the shape from a cone towards a cylinder. For a wide range of the two parameters varied (mixed layer depths between 0.75 and 1.5 times the standard mixed layer depth, and frontal density gradients between 0.2 and 4 times the standard value) the final conclusions on the roles of the three eddy types in restratification after deep convection (which are discussed in the remainder of the chapter) remain the same.

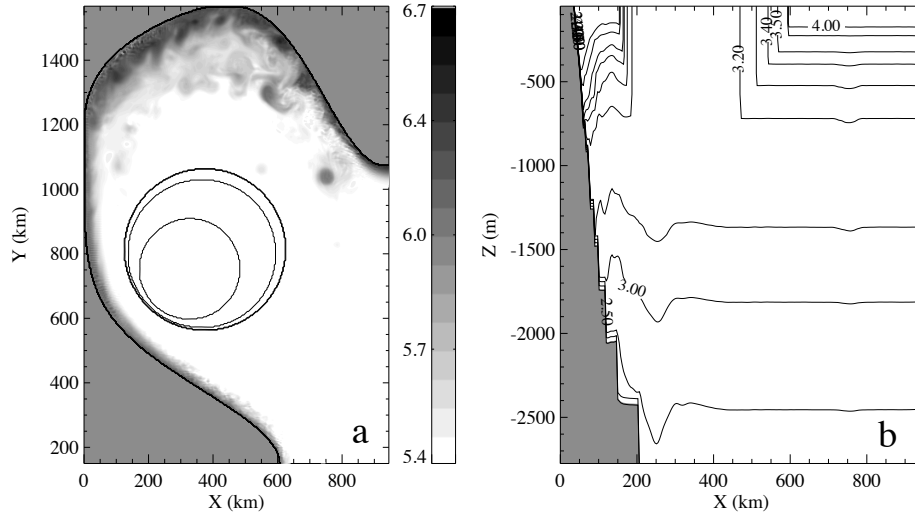


Figure 2.3: The convection area in the model, constructed based on end-of-winter data (see Figure 2.1) in the form of a skewed cone. (a) Plan view. Gray scale is temperature above 5.4°C. The IR signals are clearly visible in the northeast. (b) Zonal cross section at $y = 700$ km. Contours indicate temperature (°C).

2.2.3 The eddy field

To gain confidence that the model is realistically representing eddy processes, we examine one of our numerical simulations in which all three eddy types are resolved (see Section 2.2.4). As a good measure of the overall eddy activity, Figure 2.4 gives the surface eddy speed (V_{EKE}) calculated from the model velocity fields, as an average over the 6 months of the spindown simulation according to

$$V_{EKE} = \left(\overline{u'^2 + v'^2} \right)^{1/2}$$

where the primes denote deviations from the mean flow and the bar denotes the time mean. Lilly et al. (2003) showed V_{EKE} as inferred from satellite observations (their Figure 24). In their altimetry analysis as well as in our model the maximum V_{EKE} is found at the location where IRs are shed. From there the signal fans out in a southwesterly direction and then decays in a southerly direction, broadly indicating the path of the IRs that travel into the basin interior (8 IRs followed this pathway in our 6 month spindown simulation). The somewhat higher values in the model compared to the altimetry-based estimate are likely because of the processing of the altimeter data involving some smoothing that can lead to an underestimation of the

EKE maximum. The secondary EKE maximum around $x = 500$ km and $y = 650$ km may be the footprints of individual eddies, an effect of the relatively short averaging period. However, a secondary maximum was also reported by Lilly et al. (2003) at this location. Overall, the pattern is in good agreement with observations.

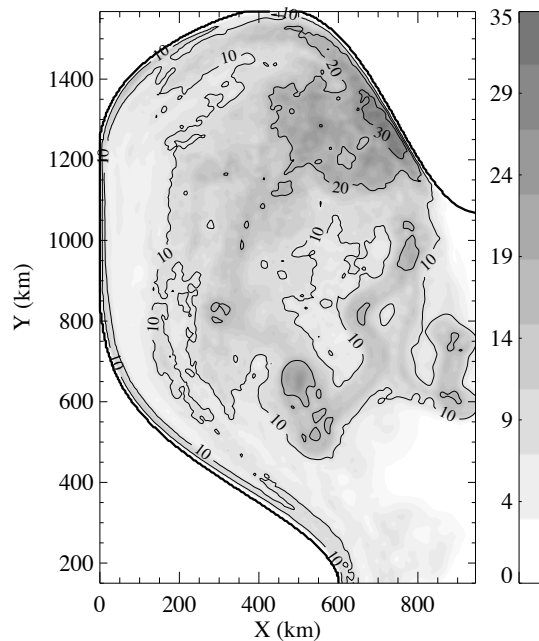


Figure 2.4: Surface eddy speed (V_{EKE}) averaged over the 6 month spindown simulation (cm s^{-1}). The field is smoothed with a two dimensional 3-point boxcar filter.

Further support for the realism of the eddy field may be obtained by comparing the characteristics of the model-generated eddies with observations. CEs and BCEs are however too small to be captured by satellite altimetry and they are only occasionally sampled by a mooring (Lilly et al. 2003). On IRs more data is available, both remotely observed by satellites and in situ in mooring records (Lilly et al. 2003), in glider and float records (Prater 2002, Hatun et al. 2007) and, occasionally, in the WOCE AR7W hydrographic sections (Rykova et al. 2009). Their characteristics can be compared with the model results in more detail.

The IRs in the model are traced by eye from their surface temperature and sea surface elevation signal. In line with observations (Lilly et al. 2003, Prater 2002), most IRs are anticyclonic, but some dipoles and cyclonic features have been ob-

served as well. The maximum velocity in the IRs ranges between 0.4 and 0.8 m s^{-1} , occasionally reaching 0.95 m s^{-1} when just shed off. These results are in excellent agreement with the 0.3 to 0.8 m s^{-1} range obtained by Lilly et al. (2003). The radius of the model-generated eddies, defined by the distance between its center and the velocity maximum, ranges between 15 and 27 km, again in good agreement with the 15-30 km found by Lilly et al. (2003). As an example, Figure 2.5 shows the meridional velocity and temperature profile in a cross section of a representative IR from our model simulation. Its properties are in good agreement with available data (Lilly et al. 2003, Hatun et al. 2007, Rykova et al. 2009), recalling that the density in our model is temperature dependent only. The surface intensification and weakening of the currents below 500-700 m depth is also well reproduced.

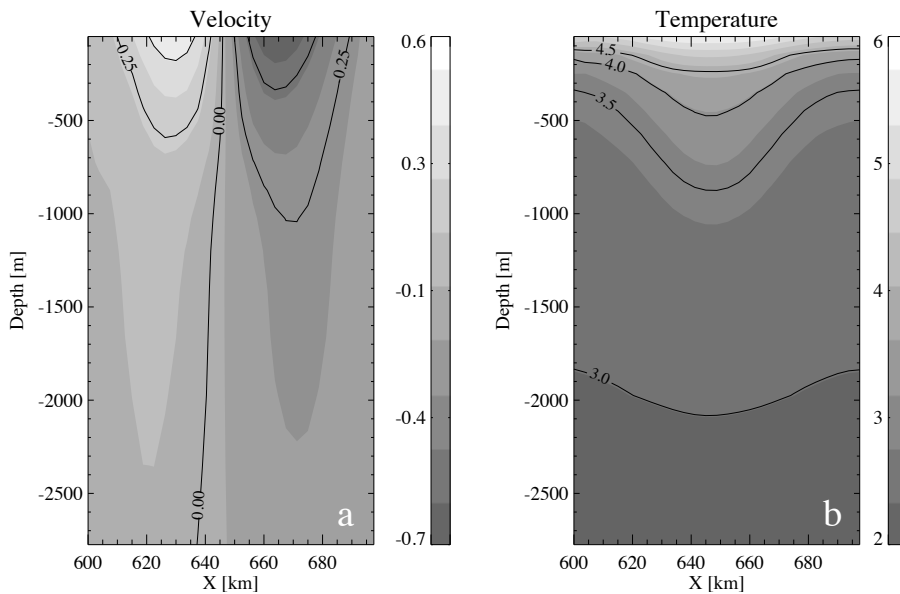


Figure 2.5: Zonal cross section of an example Irminger Ring from the model ($x = 620 \text{ km}$, $y = 630 \text{ km}$, $t = 3 \text{ months}$, visible in the upper right panel of Figure 2.6). (a) Meridional velocity (contour interval is 0.25 m s^{-1}). (b) Temperature (contour interval is 0.5°C).

2.2.4 Set-up of the simulations

Now that we have confidence in our model performance, we can describe three simulations designed to isolate the effects of different eddy types (Table 2.2). The

first case, referred to as *ALL_IN*, includes all three eddy types discussed in Section 2.1 and is hence the most realistic one (Figures 2.2 to 2.5 were obtained from this simulation). In the second case, *NO_IR*, the formation of IRs is suppressed using a bathymetry with a wider slope along the west Greenland coast (Katsman et al. 2004). The effect of IRs on restratification can be assessed by comparing the *ALL_IN* case with the *NO_IR* case. The restratifying effect of CEs can be studied from the third case, *NO_BC*, where the boundary current itself is left out, so that both IRs and BCEs are eliminated. The effect of BCEs on restratification may be analyzed by comparing the *NO_BC* case with the *NO_IR* case.

Simulation name	Description	Resolved eddies		
		IR	BCE	CE
<i>ALL_IN</i>	unstable BC, steep slope	+	+	+
<i>NO_IR</i>	unstable BC, wide slope	-	+	+
<i>NO_BC</i>	no BC	-	-	+

Table 2.2: Overview of three cases that are studied and the eddy types resolved in these simulations.

2.3 Restratification after deep convection

The results of the three spindown simulations are discussed by first analyzing the evolution of the heat content in the convection area. Next, the amount of LSW exported by the boundary current is discussed.

The evolution of the sea surface temperature may be used as an initial indicator of how the three eddy types act to restratify. It is displayed in Figure 2.6 for the three cases listed in Table 2.2, after three months and after six months in the simulations. The restratifying effect of the CEs alone (left panels) is clearly insufficient to warm up the Labrador Sea in half a year. The *NO_IR* case (middle panels) shows stronger surface warming, but the warming is not fast enough. The center of the convection area is only starting to gain some heat after half a year. When IRs are present (right panels), the surface rapidly warms suggesting fast restratification of the Labrador Sea within 6 months. Also, in the right panels more violent mixing takes place: after three months the blue patch is already diluted. The mixing is caused by the high stirring rate of the IRs (see also Figure 2.9, which shows the concentration of a passive tracer that was initialized in the convection area only). They break up the convection area and mix on the large scale. It is likely that BCEs and CEs play a role in mixing to smaller scales and disintegrating the coherent IRs.

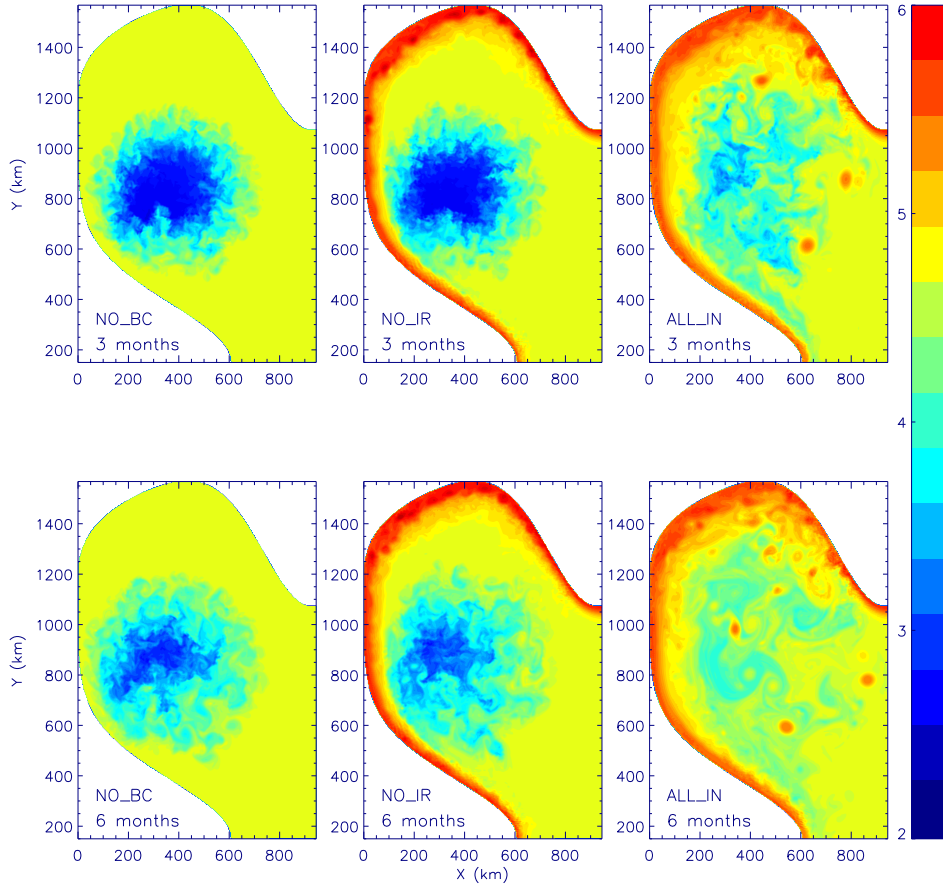


Figure 2.6: Snapshot of the surface temperature field ($^{\circ}\text{C}$) for the three different cases. Left: *NO_BC*. Middle: *NO_IR*. Right: *ALL_IN*. Upper row: $t = 3$ months. Lower row: $t = 6$ months.

The importance of IRs for restratification is confirmed by the evolution of temperature with depth at the center of the convection area for the *NO_IR* case (Figure 2.7a) and the *ALL_IN* case (Figure 2.7b). Without IRs, the first signs of warming can be observed after three to four months, but the effect is very shallow and weak. In contrast, when IRs are present the warming already starts after 1.5 months. This is in line with in situ data (Lilly et al. 1999, Avsic et al. 2006). Figures 2.6 and 2.7 thus point towards a dominant role of IRs in the restratification process. In the following

these results will be supported quantitatively.

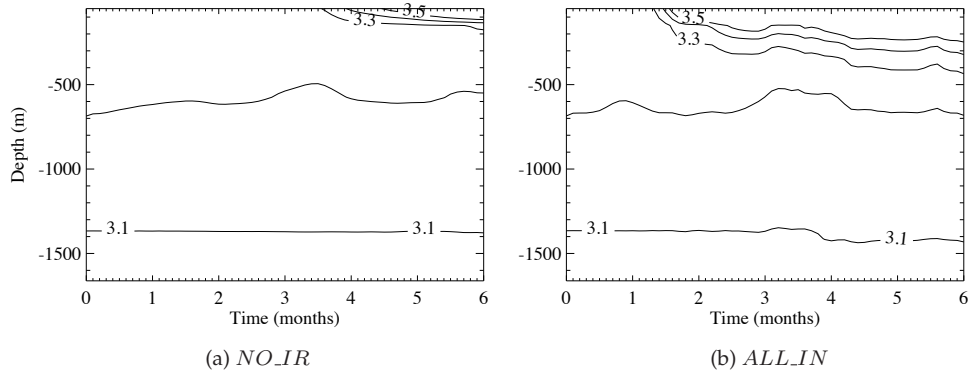


Figure 2.7: Time series of the temperature evolution averaged over an area in the center of the convection area ($x = 350\text{-}450$ km, $y = 825\text{-}925$ km) for the (a) *NO_IR* case and the (b) *ALL_IN* case. Contours are plotted every 0.1°C .

2.3.1 Heat content change of the convection area

An objective measure of the effect of the different eddies on restratification is the change in heat content of the convection area over time. The cone of mixed cold water prescribed as initial condition (Section 2.2.2) has a heat deficit with respect to the unconvected state of

$$\Delta H(t) = \rho_0 c_p \int (T(x, y, z, t) - T(x, y, z, 0)) dV \quad (2.3)$$

where ρ_0 is a reference density, c_p the heat capacity, and $T(x, y, z, t)$ is the instantaneous temperature at a certain location in the convection area. The integral is over the volume of the initial convection cone (Figures 2.1b and 2.3).

Figure 2.8 shows the evolution of the heat deficit $\Delta H(t)$, normalized by its initial value. The CEs replenish 25% of the initial heat deficit within six months. BCEs add another 5% to this, while IRs are able to restratify another 45%. At the end of the *ALL_IN* simulation about 75% of the initial heat deficit is replenished. Note that the effect of the BCEs and IRs on the heat content includes export of LSW out of the convection area by the boundary current, which is discussed below.

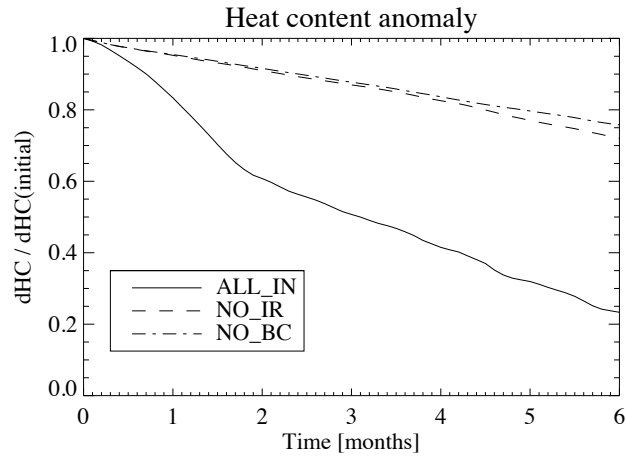


Figure 2.8: Heat content deficit of the convection area normalized by its initial value. The latter is defined as the reduction in the heat content that arises from the construction of the convection area (Section 2.2.2). A zero heat content anomaly implies that the heat content of the convected cone has become exactly equal to the heat content of a cone before convection. Solid line: *ALL_IN*. Dashed line: *NO_IR*. Dash-dotted line: *NO_BC*.

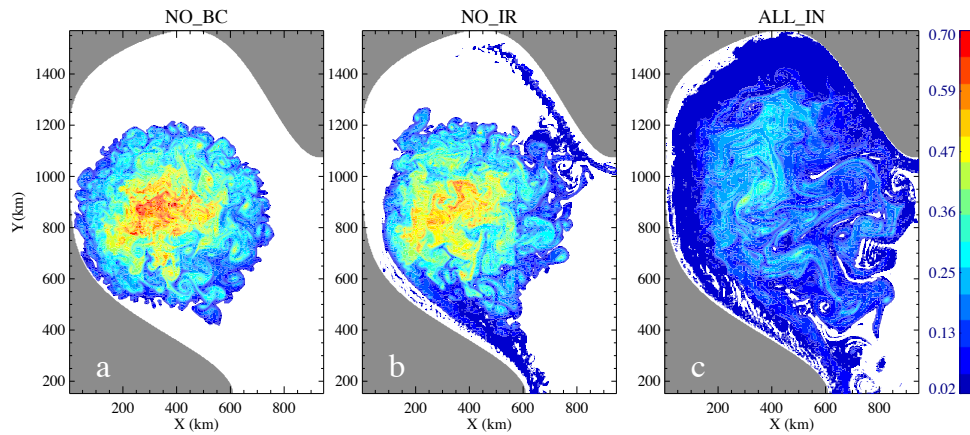


Figure 2.9: Depth-averaged concentration of a passive tracer after 6 months in the spindown simulations (a) *NO_BC* (b) *NO_IR* (c) *ALL_IN*. The tracer was initialized to 1 inside the convected area and to 0 in the remainder of the domain.

2.3.2 Export of LSW by the boundary current

Export of LSW by the boundary current may be a non-negligible factor in restratification (Brandt et al. 2007). Simulations in which a passive tracer was added in-

side the convective cone illustrate this process (Figure 2.9). The panels show the depth-averaged tracer concentration after six months. As the *NO_BC* case has no boundary current, the spreading of the passive tracer is entirely due to CEs.

In the *NO_IR* case some of the LSW is exported by the boundary current, which is indicated by the blue tongue extending southwards. In our model simulation, 1.6% of the LSW was transported southwards past the $y = 200$ km line within 6 months. In the *ALL_IN* case about 6.7% of the convected water is exported in the boundary current. We hypothesize that this is due to the substantial stirring by IRs, which increases the interaction with the boundary current. The export in the *ALL_IN* case is equivalent to 1 Sv, in good agreement with the amount of overturning related to the convectively transformed waters formed in the interior (Pickart and Spall 2007). Brandt et al. (2007) reported an export of newly ventilated water of about 9 Sv, but a substantial part of this is formed in the boundary current itself (see their Figures 1a and 11b). Note also that the export rate shows a large interannual variability, and that single-year simulations such as the ones in Brandt et al. (2007) and this study will not cover the whole range. Notwithstanding this uncertainty, the model results indicate that the LSW formed in the interior gives a minor contribution to the total export, as can be expected for a simulation in which convection in the boundary current is absent.

The tracer studies also shed some light on the notably small difference between the restratification rate in the *NO_BC* case and the *NO_IR* case. In the case without a boundary current restratification is expected to be very slow, which is supported by the model results (Figure 2.8). Simply adding a warm boundary current, without the Irminger Rings (*NO_IR*), has however little effect (unless the convection area is unrealistically large and immediately adjacent to the boundary current throughout the whole Labrador Sea; not shown). The stirring by the Irminger Rings, which acts as a catalyst, is thus essential for the boundary current to be truly effective on restratification.

2.4 Restratification time scale

To generalize the results of the numerical simulations, we derive relevant scaling relations for the time it takes to restratify the convection area. This also allows for a direct comparison with observations. Moreover, it provides a framework for an objective discussion of the discrepancies between previous studies (Section 2.5). Jones and Marshall (1997) derived a restratification time scale for a cylinder-shaped convection area with a constant ambient stratification, where only CEs restratified. Here, we extend their analysis by including cone-shaped convection areas. We also derive time scales for restratification by BCEs and IRs. For simplicity, we consider

a symmetric cone-shaped convection area rather than the skewed shape used in the model simulations (Figures 2.1b and 2.3). Furthermore, the stratification is assumed to be constant with depth as in Jones and Marshall (1997). A schematic with the definitions used in this section is given in Figure 2.10.

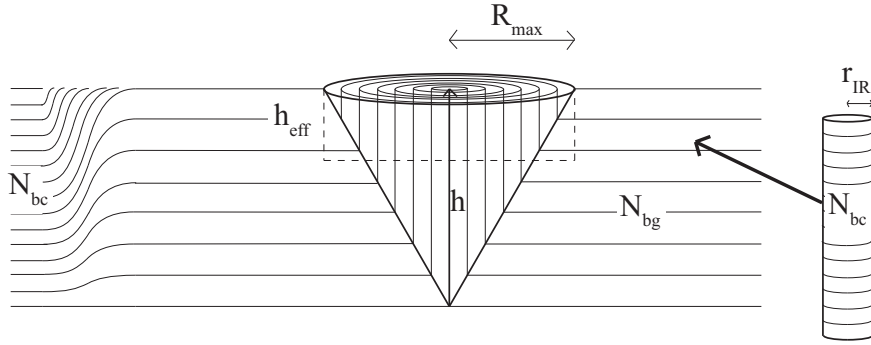


Figure 2.10: Definitions of the variables used in the derivations of the restratification time scales in Section 2.4.1.

2.4.1 Derivation of restratification time scales

In the absence of surface forcing and other restratification mechanisms, the buoyancy gain of a convected cone due to CEs can be expressed as (Jones and Marshall 1997)

$$\frac{\partial}{\partial t} \int_{V_{cone}} \bar{b} dV_{cone} = - \oint \int_{-h}^0 \overline{\mathbf{v}'b'} \cdot \mathbf{n} dz dl \quad (2.4)$$

where V_{cone} is the volume of the cone-shaped convection area, \bar{b} is buoyancy deficit with respect to an unconvected cone, $\overline{\mathbf{v}'b'}$ is the eddy buoyancy flux, \mathbf{n} is the normal unit vector and h is the maximum depth of the convection area. The eddy buoyancy flux is parameterized as

$$\overline{\mathbf{v}'b'} = c_e \Delta b(r, z) u_0 \quad (2.5)$$

where c_e is a dimensionless eddy efficiency coefficient, $\Delta b(r, z)$ is the buoyancy difference between the convection area and the ambient fluid as a function of depth and radial position (see Appendix A), and u_0 is the rim current velocity. The latter may be estimated from the thermal wind balance (Jones and Marshall 1997). Combining Eqs. 2.4 and 2.5 (Appendix A) yields the restratification time scale for CEs only

$$\tau_{CE} = \frac{1}{2c_e} \frac{f R_{max}^2}{N_{bg}^2 h^2} \quad (2.6)$$

where f is the Coriolis parameter, R_{max} is the radius of the cone-shaped convection area at the surface, and N_{bg} is the buoyancy frequency based on the ambient background stratification.

If the convection area would cover the whole basin of interest, BCEs would re-stratify in the same way as CEs. The restratification time scale would then be defined by Eq. 2.6, with the background stratification N_{bg} replaced by the stratification of the boundary current, N_{bc} . If the convection area is smaller than the whole basin, as is the case in the Labrador Sea, BCEs exchange heat between the boundary current and the interior, thereby warming up the interior basin. This induces a sharper front around the convection area, which is now surrounded by warmer water. Thus, they enhance the effect of CEs. We define the stratification

$$N_{BCE}^2 = \epsilon N_{bc}^2 + (1 - \epsilon) N_{bg}^2 \quad (2.7)$$

which represents the enhancement of the stratification in the interior³ due to the influx of boundary current water (having stratification N_{bc}^2) by BCEs, by an amount measured by the parameter ϵ ($0 < \epsilon \leq 1$). If we assume that the heat which is brought into the interior from the boundary current is uniformly distributed and therefore available at the edges of the convection region, we obtain a restratification time scale for the combination of CEs and BCEs (Appendix B):

$$\tau_{CE+BCE} = \frac{1}{\left(1 + \epsilon \left[\left(\frac{N_{bc}}{N_{bg}}\right)^2 - 1\right]\right)^2} \tau_{CE} \quad (2.8)$$

Note that $\tau_{CE+BCE} < \tau_{CE}$.

IRs mainly transport heat by carrying warm boundary current water in their core from the coast towards the interior. The restratification time scale depends on the buoyancy brought into the convection area by an individual ring, as well as the frequency of occurrence f_{IR} of such an event:

$$\frac{\partial}{\partial t} \int_{V_{cone}} \bar{b} dV_{cone} = f_{IR} \pi r_{IR}^2 \int_{-h_{eff}}^0 \Delta b_{IR}(z) dz \quad (2.9)$$

In this expression, r_{IR} is the radius of the ring, $\Delta b_{IR}(z)$ is its buoyancy anomaly (see Appendix C), and h_{eff} is the effective depth over which IRs restratify. The effective depth is introduced because, since $r_{IR} \ll R_{max}$, most eddies will encounter a part of the cone with a mixed layer depth smaller than h (see Figure 2.10), so that only

³In the model simulations, the fact that restratification of the whole basin must be a multi-year effect is incorporated in the initial density field, which is constructed based on observations, and the spin-up of 6 months to get the boundary current - interior density gradient correct.

the upper part of an IR contributes to the restratification. On average, an individual eddy passing through the convection region will encounter a mixed layer depth equal to the mean depth over the cone ($h_{\text{eff}} = h/3$). This yields a restratification time scale for IRs (Appendix C):

$$\tau_{IR} = \frac{3}{10} \frac{1}{f_{IR}} \frac{R_{max}^2}{r_{IR}^2} \left(\frac{N_{bg}}{N_{bc}} \right)^2 \quad (2.10)$$

The eddy efficiency coefficient c_e

The main unknown in the scalings above is the eddy efficiency coefficient c_e , a measure for the rate at which baroclinic eddies transport buoyancy across a baroclinically unstable front. Estimates for c_e , based on theoretical reasoning, numerical simulations and laboratory experiments, mostly vary between $0.02 < c_e < 0.04$ (Visbeck et al. 1996, Jones and Marshall 1997, Spall and Chapman 1998). Larger estimates are also found in a theoretical upper bound of $c_e = 0.045$ (Spall and Chapman 1998), an estimate of $c_e \approx 0.08$ by Haine and Marshall (1998), and an order of magnitude larger estimate (Legg et al. 1996) based on a quasigeostrophic model. The eddy efficiency coefficient in the *NO-BC* simulation is $c_e = 0.02$, calculated based on the mean lateral eddy fluxes across the edge of the convected cone by CEs. This is on the lower side of the range found in previous studies, as in our cone-shaped convection area the density change across the front is not as large as in those studies.

2.4.2 Observation-based restratification time scales

The restratifying effect of the three eddy types in this area can roughly be estimated using the scalings derived in Section 2.4.1 and using representative values for the Labrador Sea. In this section the restratification time scales are calculated from observed hydrographic properties of the Labrador Sea. In addition, the scalings are applied to values based on the model configuration and compared to the simulations results (Table 2.3).

Convective Eddies

If CEs were the only restratifying mechanism at play, Eq. 2.6 gives an estimate of the time it would take to restratify the whole convection area by lateral fluxes only. The convection area as measured in situ by Pickart et al. (2002) (Figure 2.1a) gives $R_{max} = 300$ km and $h = 1500$ m. To obtain an estimate of the background stratification N_{bg} , we use the mean of late spring occupations of the WOCE AR7W section as described in Pickart and Spall (2007): In Figure 2.11 the average buoyancy frequency N in the upper 1500 m of the water column is shown as a function of position along

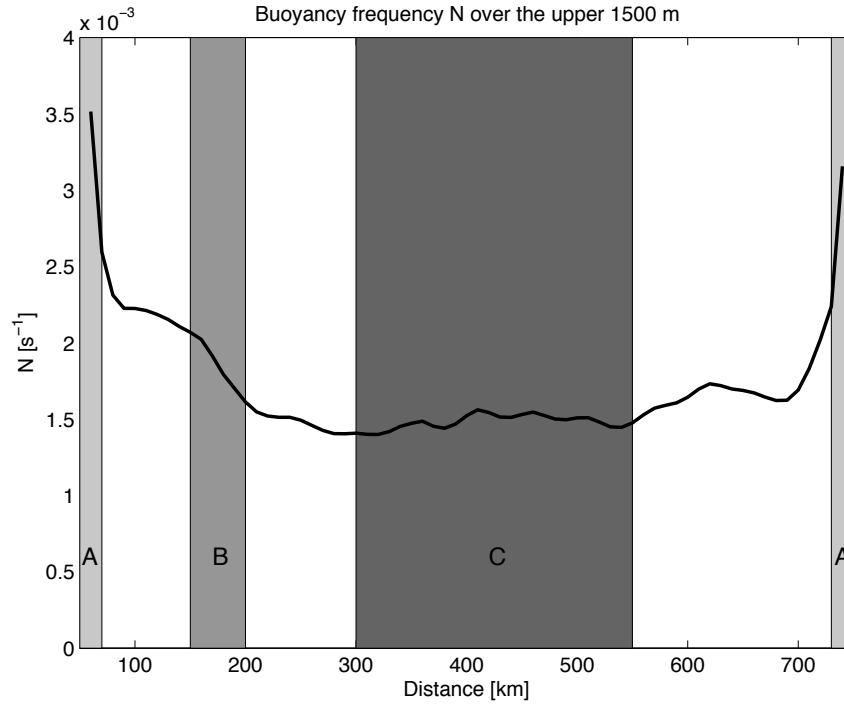


Figure 2.11: Buoyancy frequency averaged over the upper 1500 m of the water column from a mean late spring section over the 1990s (Pickart and Spall 2007). The shaded areas marked by A are used to determine N_{bc} , the area marked by B is used to determine N_{BCE} , and N_{bg} is found from the area marked by C.

this section. It shows a background stratification of around $N_{bg} = 1.5 \cdot 10^{-3} \text{ s}^{-1}$. A value for the efficiency constant c_e cannot be obtained from measurements, as in the real ocean other eddy types are always present. It seems sensible to use the range most commonly found in literature ($0.02 < c_e < 0.04$, see Section 2.4.1). Combining these values in Eq. 2.6 yields a restratification time scale τ_{CE} for CEs alone of 0.9 to 1.8 years, depending on the value of c_e . With $c_e = 0.02$ as in our model, $\tau_{CE} = 1.8$ years.

Convective Eddies and Boundary Current Eddies

An exact estimate of τ_{CE+BCE} (Eq. 2.8) based on observations is not feasible, as neither ϵ nor N_{BCE} can be retrieved from measurements directly. Nevertheless, one can estimate an upper bound from the data as follows: The contribution of BCEs to

	Observations	Model	Simulations	(Chanut et al. 2008)
c_e	0.02 - 0.04	0.02		0.02 - 0.04
N_{bg} (s^{-1})	$1.5 \cdot 10^{-3}$	$1.6 \cdot 10^{-3}$		$0.8 \cdot 10^{-3}$
R_{max} (km)	300	300		350
h (m)	1500	1500		2400
N_{BCE} (s^{-1})	$1.75 \cdot 10^{-3}$	$1.7 \cdot 10^{-3}$		-
N_{bc} (s^{-1})	$3.0 \cdot 10^{-3}$	$3.0 \cdot 10^{-3}$		$3.0 \cdot 10^{-3}$
ϵ	< 0.12	0.05		0.1
f_{IR} (per year)	15	16		1
r_{IR} (km)	20	20		20
τ_{CE} (years)	0.9 - 1.8	1.6	2.0	1.7 - 3.3
τ_{BCE+CE} (years)	> 0.7	1.3	1.8	0.3 - 0.6
τ_{IR} (years)	1.1	1.2	1.5	5.9

Table 2.3: Restratification time scales and the parameter values used to calculate them. The time scales under ‘Observations’, ‘Model’, and ‘(Chanut et al. 2008)’ are based on Eqs. 2.6, 2.8 and 2.10. The time scales under ‘Simulations’ are found by extrapolation of the lines in Figure 2.8: τ_{CE} from the *NO_BC* simulation, τ_{BCE+CE} from the *NO_IR* simulation, and τ_{IR} from the difference between the *ALL_IN* and the *NO_IR* simulations.

restratification is largest in the southwestern part of the convection area, where the boundary current is closest and the density gradient between the boundary current and convection area is therefore strongest. Moreover, it is expected that the contribution of IRs in this part of the convection area is smallest, because they originate in the northeast and propagate from there towards the interior. If we assume no contribution from IRs on this side of the convection area and take into account that the effect of BCEs is smaller everywhere else, the enhanced stratification between the boundary current and the southwestern part of the convection area thus gives an upper bound for N_{BCE} . In Figure 2.11 this region is found approximately between 150 and 200 km and has an average stratification of about $N_{BCE} = 1.75 \cdot 10^{-3} s^{-1}$. With $N_{bc} = 3.0 \cdot 10^{-3}$ from Figure 2.11 it then follows from Eq. 2.7 that $\epsilon < 0.12$. The time scale for restratification for CE and BCE is then more than 0.7 years. Due to the very stringent assumptions in determining an upper bound for N_{BCE} (the gradient between the convection area and the boundary current is generally much smaller than in the southwestern corner, and part of the IRs follow the boundary current around the basin to the western side (Prater 2002, Hatun et al. 2007) and the influence of IRs on this side is therefore not zero) it is likely to be significantly longer.

Irminger Rings

For a time scale estimate τ_{IR} (Eq. 2.10) the work by Lilly et al. (2003) may be used to obtain the frequency of IRs reaching the convection area, f_{IR} . From their Figures 40-42 it follows that 15-45 IRs are shed from the coast each year. The number of anticyclones and dipoles, which are the eddies assumed by the authors to have positive temperature anomalies, decline, averaged over 7 years, from 30 in the northern part of the Labrador Sea to 21 in the southern part (Lilly et al. 2003). With roughly 30 IRs shed per year and 70% of them reaching the southern part of the Labrador Sea, a fair estimate of f_{IR} is about 15 yr^{-1} (the estimate is lowered to 50% because the southern Labrador Sea box in Lilly et al. (2003) reaches slightly further east than the convection area). The radius of an IR is approximately 20 km (Prater 2002, Lilly et al. 2003, Hatun et al. 2007). With $R_{max} = 300 \text{ km}$ from Pickart et al. (2002) and N_{bg} and N_{bc} taken from Figure 2.11, this yields a restratification time scale of 1.1 years.

2.4.3 Model-based restratification time scales

Now that we know the time scales of restratification for the three eddy types based on observed characteristics, we can assess whether our model simulations give similar results. The parameter values from the model used in Eqs. 2.6, 2.8 and 2.10 and the resulting restratification time scales are listed in the column 'model' in Table 2.3. (N_{bg} is based on T_{ref} , N_{BCE} on the *NO-IR* simulation, ϵ is found using Eq. 2.7, f_{IR} is based on the fact that 8 IRs reached the convection area in 6 months in the *ALL-IN* simulation, and r_{IR} is also found from the *ALL-IN* simulation results.) The resulting restratification time scales are indeed in good agreement with the ones based on observations.

The actual restratification time scale in the model simulations may be estimated by linear extrapolation of the time evolution of the heat deficit in Figure 2.8. The time scales thus obtained are listed in Table 2.3 under 'simulations'. Given the simplifying assumptions in the derivation of the scalings, the estimates are very similar. Note that none of the eddy types can restratify the Labrador Sea individually within one year, but as we have seen in Section 2.3 their combined effect is much more efficient.

2.5 Discussion

From the model simulations it is evident that IRs play an important role in the process of restratification in the Labrador Sea. This conclusion is in contradiction to the results from Chanut et al. (2008). Based on the notion that two 10-year equilibrium

simulations (one with and one without IRs) both reach an equilibrium state, these authors concluded that BCEs play a crucial role in the restratification process, and that the importance of IRs is only moderate. In our view, this result does however not justify such a conclusion. A model can still produce a quasi-equilibrium state when a major source of buoyancy (IRs) is removed, but this equilibrium may not be representative for the Labrador Sea. Their simulation without IRs indeed displays a 0.1°C lower basin-averaged temperature compared to the simulation with IRs (Chanut et al. 2008). This is a significant difference representing half the annual cycle, suggesting that IRs do have a non-negligible impact in their simulations.

The prominent role of BCEs in the Chanut et al. (2008) study results from an overestimation of the effect of BCEs, combined with an underestimation of the effect of IRs. Their results display unrealistically deep mixed layers (2400 m) over a large part of the Labrador Sea for multiple winters in a row. These are caused by the strong surface cooling that is applied, which exceeds the ECMWF values by 50% (Chanut et al. 2008). Such deep mixed layers were so far only observed in a small part of the Labrador Sea basin in the early 1990s (Yashayaev 2007, see also Chapter 4). Due to the large depth and extent of the convection area the density gradient between the interior and the boundary current is very large. This enhances the efficiency of BCEs in restratifying the Labrador Sea interior.

The scaling relations from Section 2.4.1 (Eq. 2.8) illustrate how restratification can be efficient enough in their model to reach an equilibrium, despite the absence of IRs (Table 2.3). Beside the deep mixed layers (their Figure 8a), the background stratification is also weak: the mean stratification in the upper 1500 m is only $N_{bg} = 0.8 \cdot 10^{-3} \text{ s}^{-1}$ (their Figure 7a). To calculate τ_{CE+BCE} the stratification in the boundary current (N_{bc}) is also required, as well as either N_{BCE} or the parameter ϵ . From the temperature/density cross section we can infer that the stratification in the boundary current in their simulation (their Figure 7b) is at least as strong as in the climatology (their Figure 7a). We will therefore use the climatological value of $N_{bc} = 3.0 \cdot 10^{-3} \text{ s}^{-1}$ (Figure 2.11). Using $\epsilon \approx 0.1$ from the observations, Eq. 2.8 yields a restratification time scale of 0.3 to 0.6 years (Table 2.3). The strongly enhanced boundary current-interior density gradient thus enables restratification to be sufficiently quick to restratify the Labrador Sea before the next winter even without IRs.

The contribution of IRs to restratification (Eq. 2.10) in the simulation of Chanut et al. (2008) is very small because the eddies hardly reach the convection area. Their Figure 11 shows the tracks of IRs in two years of the simulation. Because the tracks lie too far north compared to observations (Lilly et al. 2003), only one or two of all the IRs actually reach the southwestern part of the Labrador Sea, giving $f_{IR} \approx 1 \text{ yr}^{-1}$. With the other parameter values as above, the restratification time scale for IRs is 5.9

years. The time scales (Table 2.3) clearly show that the restratification mechanism in Chanut et al. (2008) does not match observations.

Another study on restratification by eddies in the Labrador Sea was performed by Straneo (2006b). Using a conceptual 2-layer model this study showed that lateral eddy fluxes play an important role in the restratification process in the Labrador Sea. No distinction was made however between different eddy types. Instead, the eddy flux closure in Eq. 2.6 was used, with $c_e = 0.03$ based on literature. The case studied in Straneo (2006b) is a special case, since the convection area directly borders the boundary current and has the shape of a cylinder. The scalings derived for cone-shaped convection areas in this study are therefore not applicable. Alternatively, the time scale derived by Jones and Marshall (1997) for cylinder-shaped convection areas (their Equation 2.11) should be used:

$$\tau_{\text{restrat}} = \frac{3}{2c_e} \frac{R}{Nh}$$

where $R = 230$ km is the radius of the convection area and $h(= D - h_2) = 800$ m the depth over which lateral eddy fluxes act (Straneo 2006b). The relevant stratification is here the stratification of the boundary current N_{bc} , which can be found by taking $\frac{\partial \rho}{\partial z}$ from the center of the upper layer to the center of the lower layer ($\Delta\rho = 0.05$ kg m⁻³ and $\Delta z = 750$ m), yielding $N_{bc} = 8.0 \cdot 10^{-4}$ s⁻¹. With these values, the restratification time scale is a very realistic 0.6 years.

Because the study by Straneo (2006b) does not distinguish between different eddy types, we should compare its restratification time scale to a time scale based on our model with all three eddy types included. Assuming a linear superposition of the effects of the eddies, the evolution of the buoyancy in the convected cone is given by a combination of Eqs. 2.4 and 2.9:

$$\frac{\partial}{\partial t} \int_{V_{\text{cone}}} \bar{b} dV_{\text{cone}} = - \oint \int_{-h}^0 \overline{\mathbf{v}'b'} \cdot \mathbf{n} dz dl + f_{IR} \pi r_{IR}^2 \int_{-h_{\text{eff}}}^0 \Delta b_{IR}(z) dz \quad (2.11)$$

A restratification time scale for the combined effect of all three eddy types can be derived (see Eqs. 2.16, 2.19 and 2.22):

$$\frac{1}{\tau_{ALL}} = \frac{4}{N_{bg}^2 h} \left(\frac{c_e \left(\epsilon N_{bc}^2 + [1 - \epsilon] N_{bg}^2 \right)^2 h^3}{2 f R_{max}^2} + \frac{5}{6} f_{IR} \frac{r_{IR}^2}{R_{max}^2} N_{bc}^2 h \right) \quad (2.12)$$

With parameter values from our study (Table 2.3, 'model' column) this yields a restratification time of 0.6 years, in good agreement with the estimate from Straneo (2006b).

2.6 Summary and Conclusions

The contributions of three different eddy types (Convective Eddies, Boundary Current Eddies and Irminger Rings, see Section 2.1) to restratification after deep convection in the Labrador Sea are assessed using simulations of the restratification season with an idealized numerical model. The model configuration is comparable to the one used by Katsman et al. (2004), but highly improved in terms of basin shape and location and shape of the convection area. Furthermore, the analysis was expanded to include the effect of Boundary Current Eddies.

Three different cases were studied: one with only Convective Eddies, one with Convective Eddies and Boundary Current Eddies, and one with all three eddy types. The model results clearly show an essential role of Irminger Rings in the restratification process. Convective Eddies and Boundary Current Eddies together only replenish 30% of the initial heat loss, while IRs add another 45% (Figure 2.8). Part of the effectiveness of Irminger Rings in restratification is due to enhanced interaction with the boundary current: In the simulation with Irminger Rings, the transport of convected water out of the convection region is four times larger than in the simulation without Irminger Rings. Also, IRs stir the convected water through the basin, thereby facilitating mixing by the smaller eddies. Thus, while we argue that IRs are required for restratification in this region, they may need the smaller eddies to be genuinely effective.

Simple theoretical scalings, used to assess the time it takes the three different eddy types to restratify the convective region, lead to the same conclusion (Table 2.3). The estimated restratification time scales show that none of the three eddy types can restratify the Labrador Sea by themselves during one restratification season. The contribution of IRs (restratification time scale of 1 year and 1 month) is slightly larger than the contribution of CEs and BCEs together (restratification time scale of more than 1 year and 2 months). When all three eddy types contribute to the restratification process, the estimated time scale is a realistic 7 months.

A few interesting questions for further research have arisen from this study. First, it was shown that IRs are an efficient mixer, which suggests that their interaction with the other eddy types may not be a simple linear superposition. Although the scalings, which are based on the assumption of this linear superposition, give very reasonable results, the nature of the interaction might be important for a proper representation of the restratification process. Also, the pathways of the IRs are apparently of vital importance to model the restratification appropriately. It is as yet unclear what determines these pathways and why they are different in the Chanut et al. (2008) model. Third, the frequency of IRs reaching the convection area shows a seasonal and interannual variability in reality. The question how that affects the

restratification process is still unanswered. Last, and perhaps most importantly, IRs are not resolved in the current generation of global climate models. As the eddies play an important role in restratification in this area, they should be adequately parameterized.

Appendix A: Derivation of τ_{CE}

The evolution of the buoyancy deficit in the convection area is equal to the buoyancy flux through the lateral surface of the cone by CEs:

$$\frac{\partial}{\partial t} \int_{V_{cone}} \bar{b} dV_{cone} = - \oint \int_{-h}^0 \overline{\mathbf{v}'b'} \cdot \mathbf{n} dz dl \quad (2.13)$$

where the left hand side represent the change in buoyancy in time, integrated over the volume of the cone. The buoyancy flux through the sides of the cone $\overline{\mathbf{v}'b'}$ is parameterized by

$$\overline{\mathbf{v}'b'} = c_e \Delta b(r, z) u_0 \quad (2.14)$$

with c_e an eddy efficiency coefficient, $\Delta b(r, z)$ the buoyancy difference between the convection area and the ambient fluid

$$\Delta b(r, z) = N_{bg}^2 h \left(1 + \frac{z}{h}\right) \left(1 - \frac{r}{R_{max} (1 + z/h)}\right) \quad (2.15)$$

as a function of horizontal position r and vertical position z in the convected cone. N_{bg} is the background stratification, h the maximum convection depth, and R_{max} the radius of the cone at the sea surface. u_0 is the rim current velocity at the surface, which can be found from the thermal wind balance as follows:

$$\frac{\partial u}{\partial z} = \frac{1}{f} \frac{\partial \rho}{\partial r} \approx \frac{1}{f} \frac{\Delta b(0, z)}{R_{max} (1 + z/h)} = \frac{1}{f} \frac{N_{bg}^2 h}{R_{max}}$$

with density ρ . Integrating over the vertical direction gives the velocity as a function of z :

$$\int \frac{\partial u}{\partial z} dz = \frac{1}{f} \frac{N_{bg}^2 h^2}{R_{max}} \left(\frac{z}{h} + c\right)$$

$$\Rightarrow u(z) = \frac{1}{f} \frac{N_{bg}^2 h^2}{R_{max}} \left(\frac{z}{h} + c\right)$$

The integration constant can be obtained by ensuring that the vertical integral of u over the mixed layer is zero:

$$\begin{aligned}\int_{-h}^0 u(z) dz &= \frac{1}{f} \frac{N_{bg}^2 h^2}{R_{max}} \left(\frac{1}{h} \int_{-h}^0 z dz + c \int_{-h}^0 dz \right) \\ &= \frac{1}{f} \frac{N_{bg}^2 h^2}{R_{max}} \left(-\frac{1}{2} h + c h \right) = 0 \Rightarrow c = \frac{1}{2} \\ u(z) &= \frac{N_{bg}^2 h^2}{f R_{max}} \left(\frac{z}{h} + \frac{1}{2} \right)\end{aligned}$$

The right hand side of Eq. 2.13 is then, after dividing over the volume of the cone:

$$\begin{aligned}& \frac{1}{V_{cone}} 2\pi \int_{z=-h}^0 \int_{r=0}^{R_{max}(1+\frac{z}{h})} c_e \Delta b(r, z) u(z=0) dr dz \\ &= \frac{2\pi}{\frac{1}{3}\pi R_{max}^2 h} \int_{z=-h}^0 \int_{r=0}^{R_{max}(1+\frac{z}{h})} c_e N_{bg}^2 h \left(1 + \frac{z}{h}\right) \left(1 - \frac{r}{R_{max}} \left(1 + \frac{z}{h}\right)^{-1}\right) \frac{1}{2} \frac{N_{bg}^2 h^2}{f R_{max}} dr dz \\ &= \frac{c_e}{2} \frac{N_{bg}^4 h^3}{f R_{max}^2}\end{aligned}$$

The integral on the left hand side of Eq. 2.13 is, after dividing over the volume of the cone:

$$\begin{aligned}& \frac{1}{V_{cone}} 2\pi \int_{z=-h}^0 \int_{r=0}^{R_{max}(1+\frac{z}{h})} r \Delta b(r, z) dr dz \\ &= \frac{2\pi}{\frac{1}{3}\pi R_{max}^2 h} \int_{z=-h}^0 \int_{r=0}^{R_{max}(1+\frac{z}{h})} r N_{bg}^2 h \left(1 + \frac{z}{h}\right) \left(1 - \frac{r}{R_{max}} \left(1 + \frac{z}{h}\right)^{-1}\right) dr dz \\ &= \frac{1}{4} N_{bg}^2 h\end{aligned}$$

The time scale can now be found by equating the right and left hand side of Eq. 2.13:

$$\begin{aligned}\frac{c_e}{2} \frac{N_{bg}^4 h^3}{f R_{max}^2} &= \frac{1}{\tau_{CE}} \frac{1}{4} N_{bg}^2 h \\ \tau_{CE} &= \frac{1}{2c_e} \frac{f R_{max}^2}{N_{bg}^2 h^2}\end{aligned}\tag{2.16}$$

Appendix B: Derivation of τ_{CE+BCE}

Eq. 2.13 is also applicable to restratification by BCEs. The left hand side, i.e. the initial buoyancy deficit, is unchanged, but the rate of restratification differs. The closure from Eq. 2.14 is still valid, but the buoyancy difference $\Delta b(r, z)$ is now larger.

BCEs basically warm up the basin surrounding the convection area, thereby enhancing the effect of CEs. We therefore introduce a new stratification

$$N_{BCE}^2 = \epsilon N_{bc}^2 + (1 - \epsilon) N_{bg}^2 \quad (2.17)$$

with N_{bc} the stratification in the boundary current and ϵ a parameter ($0 < \epsilon \leq 1$). The buoyancy difference (Eq. 2.15) is then

$$\Delta b(r, z) = (\epsilon N_{bc}^2 + (1 - \epsilon) N_{bg}^2) h \left(1 + \frac{z}{h}\right) \left(1 - \frac{r}{R_{max} \left(1 + \frac{z}{h}\right)}\right) \quad (2.18)$$

Analogous to the case of CEs this gives the following velocity profile based on the thermal wind balance:

$$u(z) = \frac{(\epsilon N_{bc}^2 + (1 - \epsilon) N_{bg}^2) h^2}{f R_{max}} \left(\frac{z}{h} + \frac{1}{2}\right)$$

The right hand side of Eq. 2.13 for the BCE case is thus, after division by the volume of the cone

$$\begin{aligned} & \frac{1}{V_{cone}} 2\pi \int_{z=-h}^0 \int_{r=0}^{R_{max}(1+\frac{z}{h})} c_e \Delta b(r, z) u(z=0) dr dz \\ &= \frac{2\pi}{\frac{1}{3}\pi R_{max}^2 h} \int_{z=-h}^0 \int_{r=0}^{R_{max}(1+\frac{z}{h})} \left[c_e (\epsilon N_{bc}^2 + (1 - \epsilon) N_{bg}^2) h \left(1 + \frac{z}{h}\right) \left(1 - \frac{r}{R_{max} \left(1 + \frac{z}{h}\right)}\right)^{-1} \frac{1}{2} \frac{(\epsilon N_{bc}^2 + (1 - \epsilon) N_{bg}^2) h^2}{f R_{max}} \right] \\ & \quad dr dz \\ &= \frac{c_e}{2} \frac{(\epsilon N_{bc}^2 + [1 - \epsilon] N_{bg}^2)^2 h^3}{f R_{max}^2} \end{aligned}$$

Equating the left and right hand side of Eq. 2.13 yields τ_{CE+BCE} :

$$\begin{aligned} \frac{c_e}{2} \frac{(\epsilon N_{bc}^2 + [1 - \epsilon] N_{bg}^2)^2}{f R_{max}^2} &= \frac{1}{\tau_{CE+BCE}} \frac{1}{4} N_{bg}^2 h \\ \frac{1}{\tau_{CE+BCE}} &= 2c_e \frac{h^2}{f R_{max}} \frac{(\epsilon N_{bc}^2 + [1 - \epsilon] N_{bg}^2)^2}{N_{bg}^2} \\ &= \tau_{CE} \left(1 - \epsilon \left[1 - \left(\frac{N_{bc}}{N_{bg}}\right)^2\right]\right)^2 \end{aligned}$$

$$\tau_{\text{CE+BCE}} = \frac{1}{\left(1 + \epsilon \left[\left(\frac{N_{bc}}{N_{bg}} \right)^2 - 1 \right] \right)^2} \tau_{\text{CE}} \quad (2.19)$$

Appendix C: Derivation of τ_{IR}

In the case of restratification by IRs the right-hand side of Eq. 2.14 is not appropriate to estimate the eddy flux. IRs carry buoyant water from the boundary current into the interior. An appropriate way to describe the influx of buoyancy by IRs is therefore to estimate the buoyancy brought into the convected cone by an individual ring of radius r_{IR} , and account for the frequency f_{IR} of occurrence of such an event:

$$\frac{\partial}{\partial t} \int_{V_{\text{cone}}} \bar{b} dV_{\text{cone}} = f_{\text{IR}} \pi r_{\text{IR}}^2 \int_{-h_{\text{eff}}}^0 \Delta b_{\text{IR}}(z) dz \quad (2.20)$$

For an explanation of h_{eff} see Section 2.4.1. The initial buoyancy deficit, given on the left hand side of Eq. 2.20, is the same as before ($\frac{1}{4} N_{bg}^2 h$). On the right hand side the buoyancy difference $\Delta b_{\text{IR}}(z)$ is given by

$$\Delta b_{\text{IR}}(z) = N_{bc}^2 h \left(1 + \frac{z}{h} \right) \quad (2.21)$$

The right hand side of equation of Eq. 2.20 is thus, after dividing by the volume of the cone:

$$\begin{aligned} \frac{1}{V_{\text{cone}}} f_{\text{IR}} \pi r_{\text{IR}}^2 \int_{-h_{\text{eff}}}^0 \Delta b_{\text{IR}}(z) dz &= \frac{1}{\frac{1}{3} \pi R_{\text{max}}^2 h} f_{\text{IR}} \pi r_{\text{IR}}^2 \int_{-h_{\text{eff}}}^0 N_{bc}^2 h \left(1 + \frac{z}{h} \right) dz \\ &= \frac{5}{6} f_{\text{IR}} \frac{r_{\text{IR}}^2}{R_{\text{max}}^2} N_{bc}^2 h \end{aligned}$$

Equating the left and right hand side of Eq. 2.20 gives τ_{IR} :

$$\begin{aligned} \frac{5}{6} f_{\text{IR}} \frac{r_{\text{IR}}^2}{R_{\text{max}}^2} N_{bc}^2 h &= \frac{1}{\tau_{\text{IR}}} \frac{1}{4} N_{bg}^2 h \\ \tau_{\text{IR}} &= \frac{3}{10} \frac{1}{f_{\text{IR}}} \frac{R_{\text{max}}^2}{r_{\text{IR}}^2} \left(\frac{N_{bg}}{N_{bc}} \right)^2 \end{aligned} \quad (2.22)$$

This chapter is based on: R Gelderloos, F. Straneo and C.A. Katsman – “Mechanisms behind the temporary shutdown of deep convection in the Labrador Sea: Lessons from the Great Salinity Anomaly years 1968-1971,” accepted for publication by Journal of Climate, 2012.

Chapter 3

Mechanisms behind the temporary shutdown of deep convection in the Labrador Sea: Lessons from the Great Salinity Anomaly years 1968-1971

The cure for anything is salt water

Isak Dinesen

Abstract

From 1969 to 1971 convection shut down in the Labrador Sea thus interrupting the formation of the intermediate/dense watermasses. The shutdown has been attributed to the surface freshening induced by the Great Salinity Anomaly (GSA), a fresh water anomaly in the subpolar North Atlantic. The abrupt resumption of convection in 1972, in contrast, is attributed to the extreme atmospheric forcing of that winter. Here we use oceanic and atmospheric data collected in the Labrador Sea at Ocean Weather Station Bravo and a one-dimensional mixed layer model to examine the causes of the shutdown and resumption of convection in detail. These results highlight the tight coupling of the ocean/atmosphere in convection regions and the need to resolve both components to correctly represent convective processes in the ocean. They are also relevant to present-day conditions given the increased ice melt in the Arctic Ocean and from the Greenland Ice Sheet. Our analysis shows that the shutdown started as a result of the GSA-induced freshening as well as the mild 1968-1969 winter. After the shutdown had begun, however, two positive feedbacks (both associated with the sea-surface temperature (SST) decrease due to lack of convective mixing with warmer subsurface water) further inhibited convection. First, the SST decrease reduced the heat flux to the atmosphere by reducing the air-sea temperature gradient. Second, it further reduced the surface buoyancy loss by reducing the thermal expansion coefficient of the surface water. Convection resumed in 1972 both because of the extreme atmospheric forcing as well as advection of saltier waters into the convection region.

3.1 Introduction

In the northern North Atlantic the winter heat loss from the ocean to the atmosphere is so extreme that in certain areas, notably the Labrador Sea and the Nordic Seas, the water column becomes statically unstable and convectively mixes surface water downwards to form dense water masses (Marshall and Schott 1999). These convectively-formed dense water masses feed the lower limb of the Atlantic Meridional Overturning Circulation (AMOC). Contrary to the classical view (e.g. Stommel 1961), the current understanding is that dense water formation does not act as a driving force for the AMOC (Marotzke and Scott 1999, Kuhlbrodt et al. 2007), but that it is essential for setting its shape and strength and the variability therein (Kuhlbrodt et al. 2007).

The AMOC is responsible for a northward heat transport of the order of 1 PW (1 PW = 10^{15} W; Ganachaud and Wunsch 2000) and therefore plays an important role in the climate system. Major abrupt climate changes in the past have been attributed to large changes in the AMOC (Broecker et al. 1985, Broecker 1997, Clark et al. 2002, Alley et al. 2003), and a shutdown of the AMOC would have significant consequences for the oceanic heat supply to the North Atlantic region. As argued by Kuhlbrodt et al. (2007), the strength of the AMOC is set by dense water formation processes, and models show a strong correlation between the variability in deep Labrador Sea convection and AMOC variations on interannual to decadal time scales (Eden and Willebrand 2001, Biastoch et al. 2008). Both in modern times and in past and future climate scenarios, a slowdown or collapse of the AMOC is typically associated with a reduction of convection in the North Atlantic. In order to accurately simulate AMOC variability and its consequences for climate, it is thus very important to understand what causes deep convective variability in the Labrador Sea. In this chapter we study the details of the extreme case of a complete convective shutdown.

Two mechanisms are often proposed in literature as a potential cause of a shutdown of deep convective activity in the Labrador Sea: (1) a reduction in the heat (buoyancy) loss to the atmosphere which drives deep convection and (2) a convergence of buoyant (typically fresh) water in the convection region due to advection by the ocean circulation. Variations in the heat loss have generally followed the phase of the North Atlantic Oscillation (NAO) for at least the length of the instrumental records (Curry et al. 1998, Yashayaev 2007). In the early 1990s, for example, the deepest convection on record (up to 2400 m) was observed in the Labrador Sea when the NAO index was high for several years. The convergence of buoyant water, on the other hand, is associated with a lateral influx from the boundary currents surrounding the Labrador Sea (Straneo 2006a). Variations in the boundary current

characteristics, either due to changes in the freshwater carried at the surface or in the warm, salty Irminger water found below it, can thus also influence convective activity (Lazier 1980, Dickson et al. 1988, Curry et al. 1998, Häkkinen 1999, Houghton and Visbeck 2002, Mizoguchi et al. 2003, Straneo 2006a). Many studies on the distant past, recent history as well as future scenarios point out large freshwater anomalies as means of shutting down convection and affecting the AMOC, but the details on how this happens are unclear.

A well-known example of the second mechanism in recent history, which could shed more light on how fresh water anomalies cause deep convection to shut down, occurred when the Great Salinity Anomaly (GSA; Dickson et al. 1988), a low salinity signal, passed through the Labrador Sea in the late 1960s and early 1970s and restricted convection to the upper ca 300 m (Lazier 1980). This event, however, also coincided with a low NAO period raising the question of how mild winters may have contributed to the shutdown. In the early 1980s convection was also strongly reduced by a fresh water anomaly (Belkin et al. 1998), yet this occurred during a high NAO period (Curry et al. 1998). Several model studies have been carried out with the aim of determining the dominant factor of the two in shutting down convective activity in the Labrador Sea during the GSA, but the results are conflicting (Häkkinen 1999, Haak et al. 2003, Mizoguchi et al. 2003).

The GSA is a particularly interesting case in recent history as deep convection was completely shut down for three winters in a row. In 1968 the GSA entered the Labrador Sea and caused a substantial freshening of the surface layer, increasing the ocean stratification. During the three following winters, all particularly mild, the convection depth did not exceed the extent of the fresh surface layer. It was not until the winter of 1971/1972 (hereafter we will refer to this winter as 1972), one of the harshest winters on record in this region (Uppala et al. 2005, see also Figure 3.8), that deep convection resumed to 1500 m depth. The traditional view (e.g. Dickson et al. 1988) is that the large fresh surface anomaly of the GSA increased the ocean stratification and thereby inhibited convective mixing, after which the very harsh winter of 1972 made convection resume. Curry et al. (1998) noted that the mild winters could have played a role as well in shutting down convection, but stated that the phase of the NAO was of minor importance based on the notion that the low-salinity event which restricted the convection depth in the 1980s coincided with a high NAO period. Yet, to date, the exact mechanism by which convection shut down has not been identified.

Here we examine in depth the relative contribution of the mild winters and of the surface freshening in shutting down convection from 1968 to 1971. Furthermore, we analyze an important feedback of the presence of the GSA on the surface buoyancy flux. Under typical deep convection conditions, warm subsurface water

is mixed upwards, keeping the surface water relatively warm and enhancing the air/sea temperature gradient and, thus, the surface heat loss. On the other hand, if no deep convection occurs the surface becomes anomalously cold. This in turn decreases the surface heat flux, which depends on the temperature gradient between the relatively warm ocean and the cold atmosphere. A second impact of a fresh surface layer is to limit the surface buoyancy flux by affecting the thermal expansion coefficient, which is smaller for lower temperatures. These observations suggest that once convection has stopped, its resumption becomes increasingly more difficult. This is not only because of the increasing stratification of the ocean (as been noted before; Dickson et al. 1988), but also because the surface ocean properties actively decrease the magnitude of the surface buoyancy flux. Thus in order to understand the full impact of freshening on deep convection - an important current topic with the increasing ice melt rates in the Arctic region (Maslanik et al. 2011, Kwok et al. 2009, Rignot et al. 2011) - a more quantitative understanding of these feedbacks is required.

To address these questions we use the oceanographic data set from Ocean Weather Station Bravo (hereafter OWS Bravo), which comprises frequent oceanographic measurements taken from 1964 to 1974 along with the usual atmospheric observations (Lazier 1980). This data set has, fortuitously, carefully documented the only complete shutdown of deep convection in the Labrador Sea in the past decades. We also investigate the causes of the return of deep convection in the winter of 1972. By unraveling the details of this particular event we hope to shed light on the mechanisms leading to both a shutdown and a return of deep convection, which will help to understand past and future climate scenarios involving convective shutdowns.

This chapter is structured as follows. In sections 3.2 and 3.3 the observational data used in this study are presented (the hydrographic observations in section 3.2 and the air-sea fluxes in section 3.3). These data are carefully analyzed in section 3.4 to assess the relative importance of the mild winters versus the low surface salinity in the shutdown of deep convection in the winters of 1969 to 1971. First, in section 3.4.1 we discuss the increasing stratification that is traditionally assumed to be responsible for the absence of deep convection in these years. Then, using bulk formulas, in section 3.4.2 the impact of the low sea surface temperature on the surface buoyancy fluxes is analyzed, which could have played a role in the persistence of the non-convective state (through the surface feedbacks). Also, the effect of the mild winters on the surface buoyancy flux is quantified in this section. Finally, the actual impact of the ocean surface feedbacks and the mild winters on the convection depth are quantified using a simple 1D mixed layer model in section 3.4.3. In section 3.5 the same model is used to investigate the return of deep convection in 1972. The results presented in this study are summarized and discussed in section 3.6.

3.2 Hydrographic characteristics at OWS Bravo

The oceanic part of the OWS Bravo data set (Figure 3.1) comprises 11 years of year-round, relatively high-frequency oceanographic measurements, from January 1964 to September 1974 (Lazier 1980). The sampling rate during this period varied between 6 hours and 2 months. Here we use monthly averages of the data interpolated to standard depth levels (Kuhlbrodt et al. 2001). Linear interpolation was used for months when data were missing.

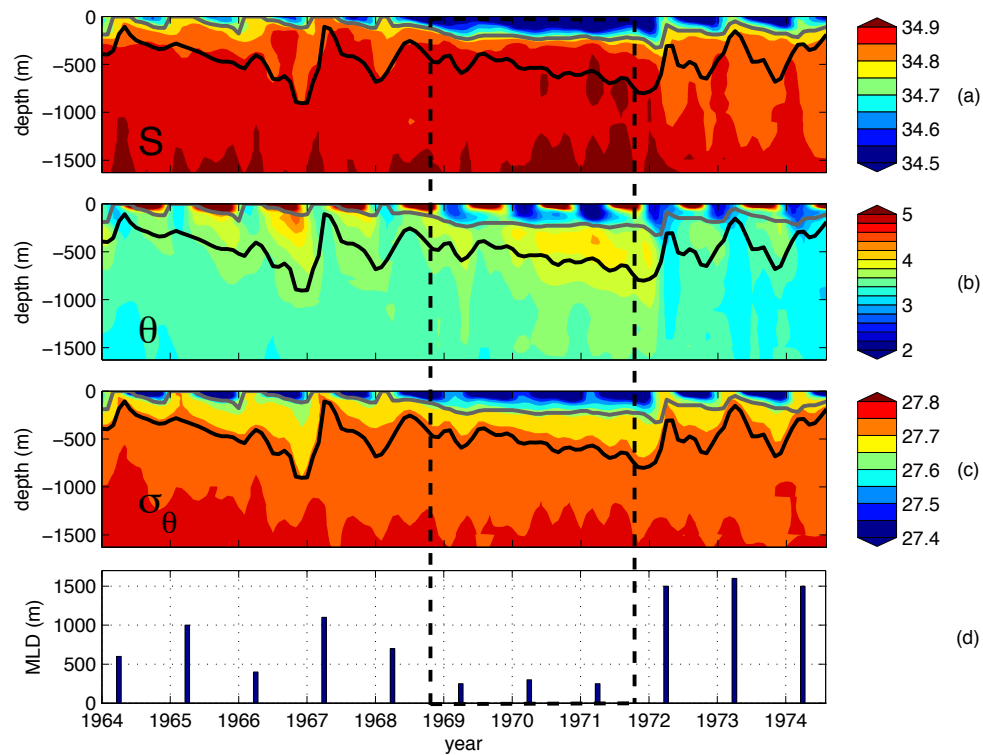


Figure 3.1: Time series of the oceanographic measurements taken at Ocean Weather Station Bravo. (a) salinity (psu); (b) potential temperature ($^{\circ}\text{C}$); (c) potential density (kg m^{-3}); (d) mixed layer depth (MLD in m). The thick gray line is the $S = 34.75$ psu isohaline, which we defined as the lower boundary of the cool and fresh upper layer. The thick black line is the $\sigma_{\theta} = 27.72$ kg m^{-3} isopycnal, which separates the LSW layer from the warm and saline intermediate layer. The dashed box indicates the GSA years.

The upper 1500 meters in the interior Labrador Sea broadly consist of three layers

(Straneo 2006a, Straneo 2006b, Yashayaev 2007). The upper layer, which typically occupies the upper ca. 200 m, is fed by the fresh and cold boundary current water of Arctic origin found on the continental shelves. The lower boundary of this layer is indicated in Figure 3.1 by the thick gray line, which represents the $S = 34.75$ psu isohaline¹. Below that layer resides a relatively warm and saline layer, which is typically found between ca. 200 and 800 m depth. It obtains its properties from the Irminger Current that carries water of subtropical origin, and encircles the basin while it follows the continental slope. In Figure 3.1 this layer is found between the thick gray line and the thick black line. The latter represents the $\sigma_\theta = 27.72$ kg m⁻³ isopycnal, which marks the upper boundary of the Labrador Sea Water (LSW) layer (Straneo 2006a). Note that the results we will present are not very sensitive to the exact values of the dividing isohaline and isopycnal.

The first five years and the last three years of the time series in Figure 3.1 show a clear seasonal cycle. In winter the water is convectively mixed to one homogeneous layer² of several hundred meters or more. During spring and summer, the water column is restratified and the three layers reappear. In the winters of 1969, 1970 and 1971, however, no deep convective mixing was observed (Figure 3.1d). This period coincided with the time when the GSA passed through the Labrador Sea as seen by the large freshening of the surface layer (Figure 3.1a). During this period a thickening of the upper two layers is observed, with cold and fresh water accumulating in the surface layer and the subsurface waters becoming increasingly warmer and saltier (Figures 3.1a and 3.1b). The result was a rapid increase in the stratification during these years (Figure 3.1c).

3.3 Air-sea fluxes

Besides the stratification and water properties described in the previous section, the magnitude of the surface buoyancy flux from the ocean to the atmosphere has a decisive influence on the variability of deep convection. The surface buoyancy flux consists of a surface heat flux and a surface fresh water flux component. Al-

¹The oceanographic community is currently moving towards the use of a new equation of state, TEOS10 (IOC et al. 2010), in which the practical salinity is replaced by absolute salinity. For easier reference to earlier literature on OWS Bravo data and as the difference between practical and absolute salinity is negligible in the Labrador Sea (McDougall et al. 2009), we used psu throughout this chapter.

²As in (Lazier 1980), the mixed layer depths in Figure 3.1d are based on a subjective estimate of the depth to which cold and fresh surface water was mixed downward, i.e. to the depth to which convective mixing appeared to have influenced the temperature and salinity. The values are all within 100 m of Lazier's MLD estimates (Lazier 1980), except for 1973 for which Lazier's estimate is 600 m shallower, and 1974, for which no winter estimate was given. The reason for Lazier's low estimate for 1973 is unclear, as his Figure 4 clearly shows similar cooling at 1500 m depth in the winters of 1972 and 1973.

though estimates of the fresh water flux contribution vary due to large uncertainties in the precipitation data (Sathiyamoorthy and Moore 2002, Straneo 2006a), Myers and Donnelly (2008) clearly show this term to be an order of magnitude smaller than the heat flux contribution. Moreover, the fresh water flux contribution is such that it adds buoyancy to the ocean surface and thereby inhibits convective mixing (Sathiyamoorthy and Moore 2002, Straneo 2006a, Myers and Donnelly 2008). Thus, the heat flux is the dominant contributor to the surface buoyancy loss in winter. The magnitude of the heat flux and its efficiency in extracting buoyancy from the ocean, in turn, depend on the sea surface conditions. Therefore, these are briefly discussed below before we look at the heat fluxes.

3.3.1 Conditions at the air-sea interface

The sea surface salinity (SSS) time series (Figure 3.2a) shows a clear seasonal cycle with maximum SSS around March and minimum value around October. This is a result of the convergence of fresh water from remote oceanic sources, precipitation, and vertical mixing into the saline subsurface layer in winter (Kuhlbrodt et al. 2001, Houghton and Visbeck 2002, Schmidt and Send 2007). After the winter of 1968 the SSS strongly decreased due to the GSA. The freshening continued up to early 1972, when winter convective mixing with the salty subsurface layer restored the SSS towards the pre-GSA level.

The sea surface temperature (SST) and surface air temperature (SAT) display a clear seasonal cycle as well³ (Figure 3.2b). In summer, the SST and SAT are very similar and show little interannual variability. In contrast, wintertime SATs are generally much lower than the SSTs. The 3-hourly SAT values are highly variable and the low-passed SATs vary by as much as 7°C between winters. Generally, the winters with the lowest SATs were winters with deep convection (e.g. 1967 and 1972), while winters with relatively high SATs (e.g. 1966 and 1969) were associated with shallow convective mixing (see also Figure 3.1). The wintertime SSTs, on the other hand, are much less variable with differences on the order of 1 or 2°C between winters. In contrast to the SAT time series, deep convection winters have relatively high SSTs due to convective mixing with the warm subsurface layer, while during winters when convection was very shallow the SSTs declined (Figure 3.3). Thus, in the absence of deep convection both the SSS and SST steadily decrease during winter. Convective mixing with the saline and warm subsurface layer levels off this trend for SST and even reverses it in the SSS time series.

³Atmospheric measurements and sea-surface temperature (SST) observations were taken at OWS Bravo every 3 hours and thus had a much higher frequency than the deep oceanographic observations. From the COADS data base we retrieved the data from 1964 to 1972. The data from 1973 and 1974 were not available.

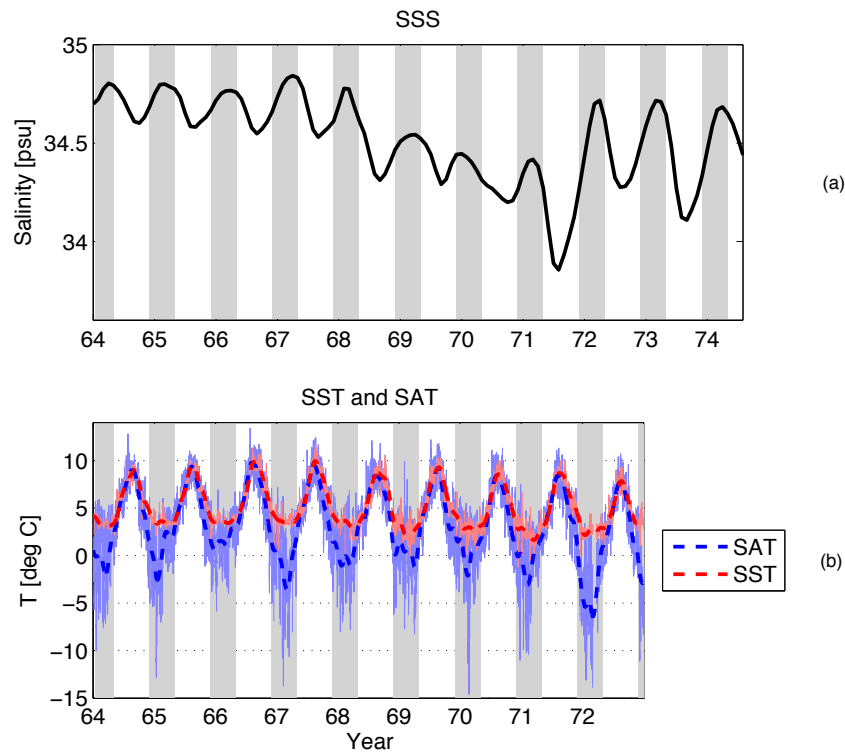


Figure 3.2: Conditions at the air-sea interface measured at OWS Bravo. (a) Monthly mean sea surface salinity (SSS). (b) Surface air temperature (SAT, blue) at 2 m height and sea surface temperature (SST, red). The thin lines are the 3-hourly values and the thick dashed lines show the 2-month low-passed time series. In both panels the shading marks the convection season (December to April).

3.3.2 Heat fluxes

The surface heat flux is the sum of the sensible heat flux, the latent heat flux, the short wave incoming radiation and the net outgoing long wave radiation. During winter the heat flux in the Labrador Sea is dominated by the sensible and latent heat flux components (Figure 3.4; note that we use ERA40 reanalysis product as according to Renfrew et al. (2002) these fluxes are within the bounds of observational uncertainty). Like for the SAT time series (Figure 3.2b), the deep convection winters are associated with a large heat flux (1965, 1967, 1968, 1972, 1973 and 1974; note that we will not include 1973 and 1974 in the analysis later on because we do not have

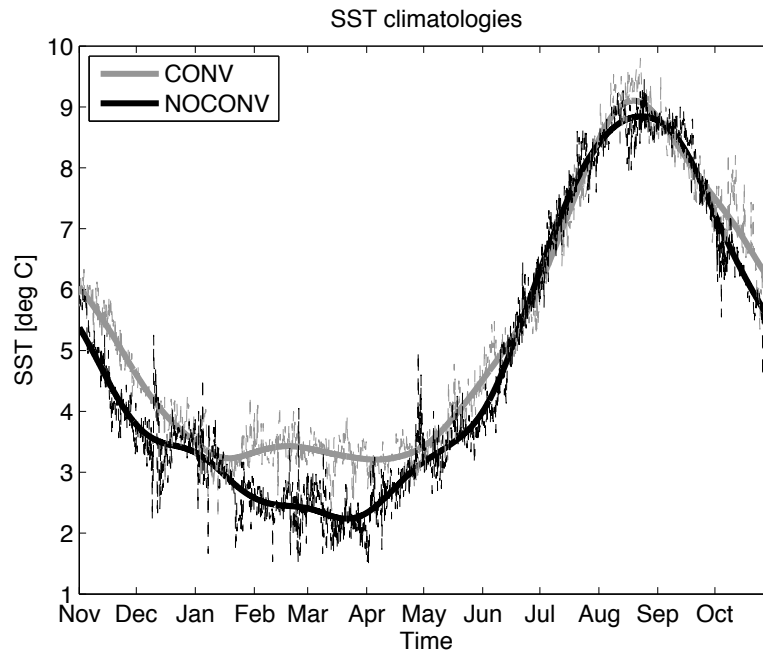


Figure 3.3: Mean of the 3-hourly (thin) and a 2-month low-pass filtered (thick) time series of in situ measured SST at the OWS Bravo site (shown in Figure 3.2b), for the mean over years without deep convection (NOCONV: 1969, 1970, and 1971; black) and years with deep convection (CONV: 1965, 1967, 1968, and 1972; gray).

the 3-hourly data for these two years). Contrary, the three years without deep convection (1969 to 1971) are associated with a remarkably small heat flux. On average, the mean heat flux over the winter months (December to April) in years with deep convection (193 W m^{-2}) is about 70% larger than in the winters without deep convection (113 W m^{-2}), 56% of which is due to a change in sensible heat flux, 33% due to latent heat flux and 11% due to changes in the radiative fluxes.

3.4 Absence of deep convection in 1969-1971

In the winters of 1969 to 1971 convective mixing was restricted to the upper 200 meters. The absence of deep convection in these winters is generally attributed to anomalously low surface salinity due to the GSA (Dickson et al. 1988, Curry et al. 1998), but the details of the process have never been quantified. A low surface salinity inhibits deep convection in two ways ('Ocean' box in Figure 3.5): (1)

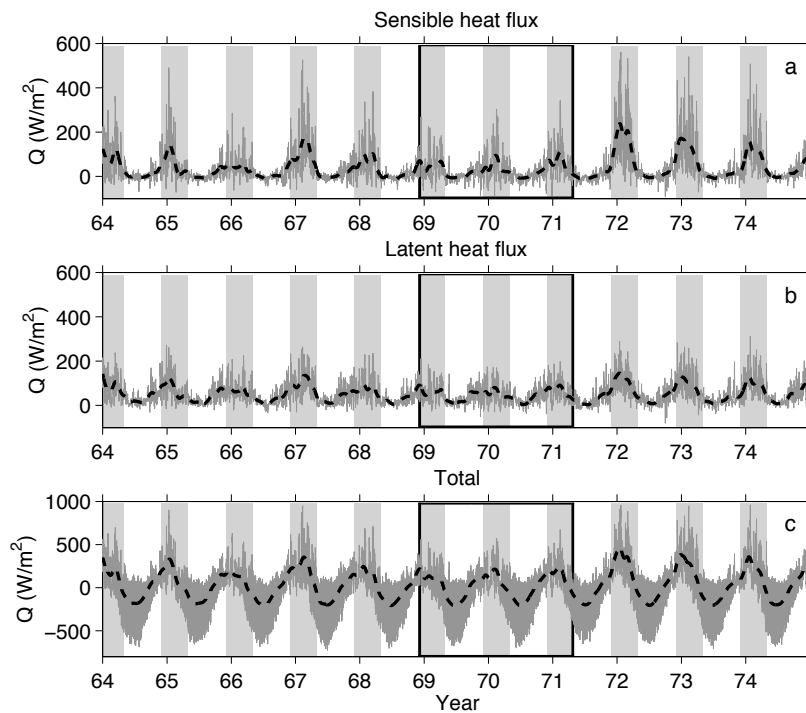


Figure 3.4: Heat-flux components over the central Labrador Sea (ERA-40; Uppala et al. 2005). (a) Sensible heat flux, (b) Latent heat flux, (c) Total heat flux (including radiative terms). The gray lines are the 6-hourly values, while the thick black dashed lines are the 2-month low passed time series. The boxes indicate the GSA years and the shading marks the convection season (December to April).

by increasing the stratification (Dickson et al. 1988, here discussed in section 3.4.1) and (2) while deep convection is shut down, by decreasing the surface buoyancy flux (section 3.4.2). The latter effect has been mostly neglected in literature and is shown here to have a non-negligible impact. It is depicted schematically in Figure 3.5 as ‘Surface feedback loop’, and works as follows: when convection is limited to the cold and fresh surface layer, no warm water is mixed upwards during the winter months (Figure 3.3). Furthermore, the small mixed layer depth implies that the accessible heat reservoir available for cooling is small. Both effects result in a rapid decline of the SST. The low SSTs reduce the heat flux to the atmosphere (Q) and thus the buoyancy flux. In addition, the thermal expansion coefficient of seawater (α) is also reduced at lower water temperatures, which further decreases the surface

buoyancy flux to the atmosphere. Oceanic conditions aside, the surface buoyancy flux was also limited by the mild winters that occurred during the GSA years ('Atmosphere' box in Figure 3.5). These three contributions to the lower surface buoyancy flux - mild winter, low SST via Q and low SST via α - are quantified in section 3.4.2.

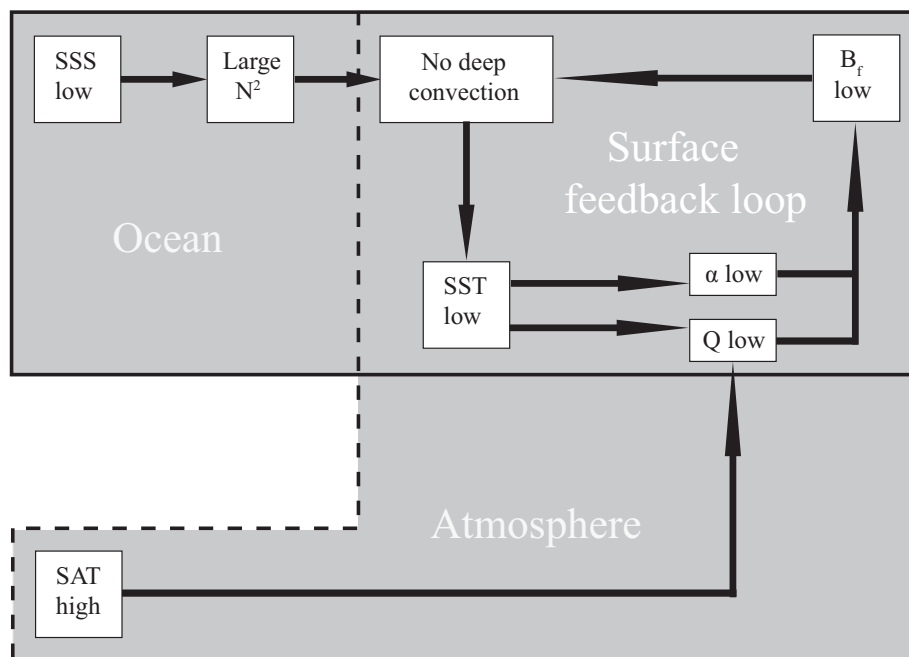


Figure 3.5: Schematic showing the feedbacks associated with the shutdown of deep convection in the winters of 1969 to 1971. SSS is sea surface salinity; N^2 is the Brunt-Väisälä frequency, a measure of ocean stratification; B_f is surface buoyancy flux; SST is sea surface temperature; α is the thermal expansion coefficient of seawater (at the surface); Q is the surface heat flux; SAT is surface air temperature.

3.4.1 Buoyancy storage through increased stratification

Due to the increasing stratification from 1969 to 1971 (Figure 3.1) the "resistance" of the ocean to deep convection increased. To quantify this increase we calculated the amount of buoyancy (ΔB) that needs to be removed for convection to reach the upper boundary of the LSW layer from early-winter (November) profiles for each

year:

$$\Delta B = \frac{g}{\rho_0} \int_{z_{\sigma_\theta=27.72}}^0 \sigma_\theta dz \quad (3.1)$$

with ΔB the required buoyancy loss to induce deep convection (in $\text{m}^2 \text{s}^{-3}$), g the acceleration due to gravity (9.81 m s^{-2}), ρ_0 a reference density (1027 kg m^{-3}), and σ_θ the potential density (in kg m^{-3}) ($z_{\sigma_\theta=27.72}$ is the depth of the upper boundary of the LSW layer, Figure 3.1). During the period when deep convection was absent (1969 to early 1972), ΔB initially remained stable, but sharply increased after 1969 (solid line in Figure 3.6). Note that the oceanic resistance to convection at the beginning of the winter of 1969 (November 1968) was not unusually high. It is similar in magnitude to the resistance in the winter of 1967 (November 1966), which was a year with deep convection (Figure 3.1).

Next, we considered whether changes in ΔB were due to the buoyancy stored in the cold and fresh upper layer (dotted line in Figure 3.6) or the amount stored in the warm and saline intermediate layer (dashed line). The water in both of these layers grew in volume over the summer 1968 to early 1972 period (Figure 3.1), but we do not know a priori how much they contributed to the ΔB increase over this period. Figure 3.6 clearly shows that the increase in ΔB during the summer 1968 to early 1972 period is almost entirely due to the increasing buoyancy storage in the upper cold and fresh layer, and that it dominates the increase over the first year. The buoyancy stored in the intermediate warm and saline layer on the other hand is more or less constant over the first two years of this period and only shows a steady increase during 1970 and 1971 when the thickness of the layer grew. To summarize, ΔB increased over the GSA period, although it was not unusually large at the beginning of this period, and this increase is primarily due to the buoyancy stored in the upper fresh layer.

3.4.2 Reduced surface buoyancy flux

In the previous section we estimated how much buoyancy needed to be removed from the ocean to induce deep convection (Figure 3.6). Next we consider the magnitude of the buoyancy flux. As mentioned above in section 3.3, we neglect the fresh water contribution, which is thought to be small. The surface buoyancy flux is then defined (Gill 1982) as

$$B_f = \frac{g\alpha}{\rho_0 c_p} [Q_{sens} + Q_{lat} + Q_{lw} - Q_{sw}] \quad (3.2)$$

where g is the acceleration due to gravity (m s^{-2}), α the thermal expansion coefficient of seawater ($^\circ\text{C}^{-1}$), ρ_0 a reference density for seawater (kg m^{-3}), c_p the heat

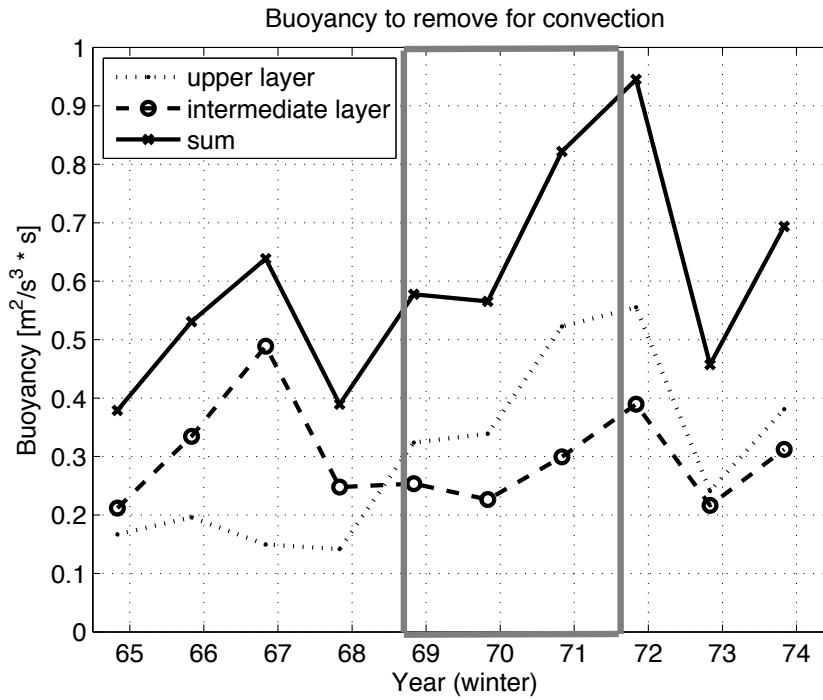


Figure 3.6: Oceanic buoyancy loss required for convection to reach the top of the LSW layer (solid line), the bottom of the upper cold and fresh layer (dotted line), and from the top to the bottom of the intermediate warm and saline layer (dashed line) at the onset of each winter (November). The solid line is thus the sum of the dashed and the dotted lines. The layers are defined in the section 3.2 and Figure 3.1. The gray box indicates the GSA years.

capacity ($\text{J (kg } ^\circ\text{C}^{-1})$), and Q_{sens} , Q_{lat} , Q_{lw} and Q_{sw} (W m^{-2}) are the sensible and latent heat flux and the heat fluxes due to long wave and short wave radiation, respectively.

The objective of this section is to assess why the surface buoyancy loss during the 1969 to 1971 winters, when convection did not reach beyond the upper fresh and cold surface layer (hereafter "NOCONV years") was smaller than during deep convection winters (1965, 1967, 1968 and 1972, hereafter "CONV years"; note that 1964 could in principle be considered a CONV year, but is excluded from the analysis as only part of this winter is covered by the data set). There are two possible mechanisms (see Figure 3.5):

1. Mild winters \Rightarrow small heat flux $Q \Rightarrow$ small buoyancy flux B_f

	Ocean	Atmosphere	Q	Bf ($\times 10^{-8}$)	ΔQ	ΔBf
NOCONV	NC	NC	105	2.19		
CONV	C	C	173	3.86	65%	76%
cold winter	NC	C	149	3.12	42%	42%
warm ocean surface	C	NC	127	2.92	21%	33%

Table 3.1: The buoyancy flux increase with respect to the mean buoyancy flux over the NOCONV winters (NC, 1969-1971) is calculated for two hypothetical cases (see text). For reference, the top two rows of this table give the mean winter heat (Q) and buoyancy (Bf) fluxes over the NOCONV and CONV winters (C, 1965, 1967, 1968 and 1972). ΔQ and ΔBf represent the increase of the heat and buoyancy flux respectively with respect to the mean over the NOCONV winters. Q is in $W m^{-2}$ and Bf is in $m^2 s^{-3}$.

2. Cold ocean surface (low SST) \Rightarrow small heat flux Q and low thermal expansion coefficient $\alpha \Rightarrow$ small buoyancy flux B_f

As the surface buoyancy loss is a function of the coupled ocean/atmosphere conditions it is difficult to separate these mechanisms. If we assume however that the air temperature is mostly related to larger scale atmospheric features (e.g. wind direction) rather than to the SST, we can look at anomalies of just one of these mechanisms at a time. Support for this assumption is found in the fact that when the SAT is high, the SST is low and vice versa, which is not what one would expect if SST had a significant impact on the local SAT.

The sensible and latent heat fluxes were calculated using the COARE bulk flux formulas (Fairall et al. 2003). In these formulas the heat fluxes are both a function of the wind speed (including a gustiness factor) and a transfer coefficient, which depends on the stability of the atmosphere. The sensible heat flux furthermore depends on the air-sea temperature difference, while the latent heat flux is a function of the difference between the water vapor mixing ratio in the atmosphere and the interfacial water vapor mixing ratio. The fluxes were first calculated for the observed atmospheric and oceanic conditions to obtain the actual heat flux and buoyancy flux during the CONV and NOCONV winters. It was found that, on average, the winter heat flux in CONV winters was 65% larger⁴ than in the NOCONV winters, while the mean winter buoyancy flux was 76% larger (Table 3.1).

Next, we combine the oceanic conditions of for example the (NOCONV) 1969

⁴The difference with the 70% reported in section 3.3.2 is mainly because the present number does not include radiation terms. About 1% is due to the difference between our own calculations from the bulk formulas with BRAVO data (this section) and ERA40 data (section 3.3.2).

winter with the atmospheric conditions of the (CONV) 1965 winter to examine how much larger the heat flux would have been if the 1969 winter had not been so mild. To examine the impact of a cold ocean, on the other hand, we use the atmospheric conditions of the (NOCONV) 1969 winter with the oceanic conditions of the (CONV) 1965 winter. This gives an idea how much larger the heat flux would have been if the ocean surface had been warmer. This procedure is applied to all possible combinations of winters and then results are averaged. Finally, for all those combinations we calculate from Eq. 3.2 how much larger the buoyancy flux would have been, both through the increased heat flux and, in the case of different oceanic conditions, through the larger α . By doing this, we necessarily neglect the radiation terms in Eq. 3.2, but this does not affect the results significantly as from the ERA40 reanalysis it is found that the radiation terms together only explain about 10% of the difference in the total heat flux between the CONV and the NOCONV winters.

The heat fluxes are calculated with the 3-hourly BRAVO data for atmospheric measures and SST. The thermal expansion coefficient α is calculated using the high resolution SST data, and SSS data linearly interpolated to the same 3-hourly resolution. An overview of the cases is given in Table 3.1.

Mild winter effect on the buoyancy flux

To quantify the impact of the mild winters we compare the heat and buoyancy fluxes of the NOCONV years with those obtained using atmospheric conditions of the (harsh) CONV winters and oceanic conditions from the (mild) NOCONV winters. We find that the average winter heat and buoyancy flux would have been 42% larger if the atmospheric conditions alone had been different (Table 3.1 and dash-dotted line in Figure 3.7).

Cold ocean surface effect on the buoyancy flux

Second, the effect of the low SST on the buoyancy flux is estimated. This effect has two contributions: from the heat flux and from α (Figure 3.5). The heat flux contribution is due to both the sensible and latent heat fluxes. The former depends on the temperature gradient between the ocean and the atmosphere, i.e. a colder ocean can give up less heat. As the wintertime SST was lower by about 1°C (Figure 3.3), we expect a reduction of the heat flux. The latent heat flux is also reduced due to lower SSTs, as the saturation value of the air just above the sea surface is lower. Because of the lower SST (and SSS), α is reduced on average over the whole winter by about 10%.

The combined effect of the reduced heat flux and α resulting from the low ocean surface temperature is investigated by combining NOCONV atmospheric condi-

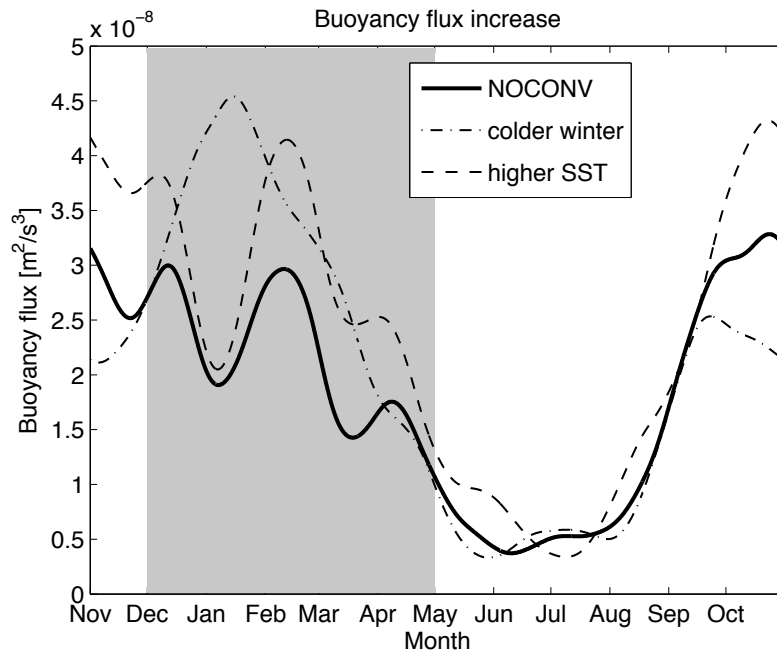


Figure 3.7: Result of the surface buoyancy flux calculations for two hypothetical cases (see Table 3.1). The buoyancy flux in the NOCONV years is given for reference as the solid line. The gray period indicates the convective season (December-April).

tions with CONV oceanic conditions (Table 3.1 and dashed line in Figure 3.7). The winter heat flux would have been 21% larger during the NOCONV years if the oceanic conditions had been those of the CONV years, while the buoyancy flux would have been 33% larger (the impact on the buoyancy flux is larger because Q and α are both larger for a higher SST). The surface buoyancy flux would thus have been 21% larger due to the Q -feedback, while the α -feedback gives an additional 12%.

Conclusions on mild winter and low SST effects on the buoyancy flux

In summary, the winter surface buoyancy flux in the years with deep convection was 76% larger than in the years when convection was restricted to the cold and fresh surface layer. This was partly caused by lower SSTs in the NOCONV years (as a result of lack of convective mixing with the warm intermediate layer) and partly by the mild NOCONV winters. While the contribution of the atmosphere to the surface

heat flux increase (+42%) is twice that of the ocean (+21%), the contribution of the atmosphere to the buoyancy flux is only slightly larger (+42% vs. +33%) due an additional feedback in the ocean component via the thermal expansion coefficient α . In other words, the reduced buoyancy loss during the NOCONV years was in almost equal parts due to mild winters and to having lower SSTs.

3.4.3 Cause of the shutdown: 1D mixed layer model analysis

1D mixed layer model

For a conclusive answer to the question whether the ocean or the atmosphere was solely responsible for the sudden cease of convection in the winter of 1969, or whether it was a combination of the two, we simulated the convection season with a 1D mixed layer model (Price et al. 1986). This model relies on bulk stability considerations to calculate the mixed layer depth. It calculates the density profile using the nonlinear equation of state, then applies surface heat and fresh water fluxes, and finally deepens the mixed layer until static stability is achieved in the density profile and a bulk Richardson number criterion is satisfied for wind mixing. A gradient Richardson number criterion is used to smooth the sharp gradient below the mixed layer. This relatively simple model has been successfully used before to simulate deep convection in the Labrador Sea (Bramson 1997) as well as the Irminger Sea (Våge et al. 2008). The model is initialized with the observed November profiles for temperature and salinity. [The results are not very sensitive to the choice to use November profiles as other initial conditions (October, December or January) give similar results and the choice is supported by model results from Mizoguchi et al. (2003), who observed that the preconditioning in November contributes significantly to the determination of the convection depth.]

The model is forced by surface heat fluxes and lateral fresh water fluxes. For the heat fluxes the 6-hourly ERA40 (Uppala et al. 2005) surface fluxes are used (Figure 3.4). This choice is based on a comparison of the sensible and latent heat fluxes from ERA40 and the recalibrated NCEP data set (Kistler et al. 2001, Renfrew et al. 2002) with our own calculation of the fluxes from observations at OWS Bravo using the COARE bulk formulas. The ERA40 fluxes closely resembled our own estimates. Note that we need a reanalysis product for an estimate of the incoming short-wave radiation and net outgoing long wave radiation, which we cannot calculate with bulk formulas. Lateral heat fluxes are ignored because, in the presence of strong surface fluxes and deep convection, it is not feasible to extract the necessary information on lateral heat fluxes from the OWS Bravo data. This does not pose a problem, however, because they are relatively small compared to the surface heat flux in winter (Straneo 2006a) and the mixed layer temperature be can fairly well

simulated by the 1D model without lateral heat fluxes (which supports the previous statement that the surface fluxes dominate).

In the case of fresh water fluxes the situation is reversed. While the exact magnitude of the surface fresh water flux is uncertain, literature hints towards a minor role of the surface fluxes with respect to lateral fluxes (Lazier 1980, Khatiwala et al. 2002, Straneo 2006a). Although in some years the lateral salinity flux is small, in other years it must be included in the model calculations to obtain a realistic mixed layer depth and properties. Therefore, the surface fresh water flux is ignored and the lateral salinity fluxes are simulated by restoring the salinity over the whole depth of the profile to the monthly mean observed profiles (Figure 3.1) with a restoring time scale of a month.

Model results

The first hypothesis that is tested using the 1D mixed layer model is whether convection ceased only because of the low SSS and SST (as a result of the GSA; 'Ocean' box in Figure 3.5). If this were the case, no reasonable winter heat flux could have induced deep convection in these winters. To test this we initialized the mixed layer model with the observed November profiles of temperature and salinity from the winters of 1969, 1970, and 1971. Then the model was forced with increasingly larger heat fluxes, until the minimum heat flux was found that resulted in deep convective mixing (mixing down to the LSW layer).

In Figure 3.8 the winter (December to April) surface heat fluxes from the ERA40 reanalysis are given for the winters of 1960 to 1999. The NOCONV winters are indicated by open squares and the winter of 1972, when deep convection returned, is highlighted by the filled circle. To put these values in perspective, consider that the winter heat loss in 1972 was 69% larger than the 40-year mean of 139 W m^{-2} , while the winter heat loss in 1969 to 1971 was up to 53% smaller. The heat flux required to induce deep convection in the model simulations is indicated by the open triangles in Figure 3.8. The likelihood of obtaining these heat fluxes (or larger ones) in the 40 years of the ERA40 record is 12.5%, 10% and 2.5% for 1969, 1970 and 1971, respectively. A harsher winter in 1969 would thus have induced deep convection despite the cold and fresh surface layer in the ocean, even though the likelihood of deep convection decreased rapidly afterwards through the surface feedbacks explained in section 3.4.2.

The second hypothesis that we can test is whether convection ceased only because of the mild winters ('Atmosphere' box in Figure 3.5). If this were the case, the 1969 winter heat flux would not have caused deep convection in other winters with 'normal' oceanic conditions either. We therefore used the model to predict the

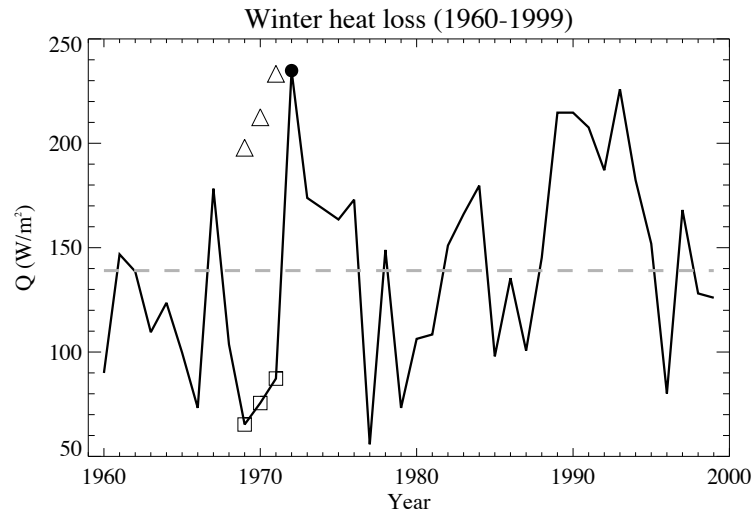


Figure 3.8: Mean winter (December-April) surface heat loss from the ERA40 reanalysis. The gray dashed line is the mean value over the 40-year time series (139 W m^{-2}). The open squares are the NOCONV years (1969-1971) and the closed circle is the winter of 1972 when deep convection returned. The open triangles indicate the heat flux required for deep convection to occur in the NOCONV winters.

extent of convection using the November temperature and salinity profiles of non-GSA winters and the 1969 winter heat flux. In the winter of 1965, when the LSW layer was closer to the surface, this heat flux would have been sufficient to induce deep convective mixing. For 1968 the mixing depth is on the edge of the LSW layer, and in all the other years no deep convection would have taken place. The likelihood of deep convection with the 1969 winter heat flux is thus at least 1 (possibly 2) out of 10 winters. In conclusion, although the sea surface conditions were unusual and the winters were unusually mild, it was the combination of these two effects that was responsible for the complete shutdown of deep convection during the GSA winters.

3.5 Return of deep convection in 1972

In the winter of 1972 deep convection returned (Figure 3.1). Here we examine whether this was due to the very harsh winter of 1972, or due to changes in the oceanic conditions. We know from Figure 3.6 that the amount of buoyancy needed to be removed for deep convection in 1972 was the highest in this decade-long

record. Also, Figure 3.2a shows that the surface salinity in the beginning of the winter of 1972 was still very low. The oceanic conditions at the start of the convection season were thus not favorable at all for deep convection. That being said, they may have changed over the course of the winter due to lateral fluxes, for example because the GSA was moving away at the time (Dickson et al. 1988). On the other hand, the winter heat flux was exceptionally large as this was a very harsh winter (Figures 3.2b, 3.4 and 3.8). The atmospheric conditions were thus very favorable for deep convection.

To answer the question whether the ocean or the atmosphere was responsible for the return of deep convection we again used the 1D mixed layer model. To study the effect of the large heat flux alone, we first calculated the evolution of the mixed layer over the winter of 1972 without (lateral) salinity fluxes, the surface heat flux thus being the only forcing. Our model run shows that convection would not have reached the observed mixed layer depth of 1500 m, but instead only to less than 600 m. The heat flux which would have been required for deep convective mixing is never observed in the 40-year ERA40 time series. Also, when a sufficiently large heat flux was imposed to mix down to the observed mixed layer depth, the water in the mixed layer was about 0.2°C too cold. This implies that (changes in) the salinity of the water column must have played a role in the resumption of deep convection. When the observed lateral salinity fluxes are added to the model simulations, the mixed layer depth and properties are well captured.

Thus, contrary to what is commonly assumed (Straneo 2006a, Yashayaev 2007), for the deep convection event in the winter of 1972 both the large winter heat flux and a change of oceanic salinity conditions were essential. The salinity change could have been caused either by the withdrawal of the GSA or by a larger than usual lateral eddy flux with a subsurface salinity maximum (Lilly et al. 2003, Hatun et al. 2007). The time resolution of the available oceanographic data is however insufficient to be conclusive on which mechanism was responsible for the change in salinity, because once the water is mixed one does not know whether it originates from the surface or deeper down. A regional model study could provide more insight on this point.

3.6 Summary and discussion

Our analysis shows that the two primary factors that inhibited deep convection during the Great Salinity Anomaly (GSA) period were the mild atmospheric winter conditions of 1969-1971 and freshening due to the GSA. The mild winters were associated with a small heat and buoyancy loss to the atmosphere. The way in which the GSA affected convection is more complex (Figure 3.5): The initial response of the

Labrador Sea to the GSA was an increasing stratification, which inhibited convective mixing into the underlying warm, salty layer. Two positive feedbacks ensued which further decreased the surface buoyancy flux and resulted in the shutdown of convection until the winter of 1972.

The surface feedbacks are as follows (Figure 3.5). In a regular convection winter, warm subsurface water is mixed upwards and counteracts the surface cooling. When no convection occurs, however, the surface continues to cool down from about 3.2 °C to about 2.2 °C (Figure 3.3). A lower sea surface temperature (SST) limits the surface sensible and latent heat fluxes to the atmosphere and thus the magnitude of the surface buoyancy flux. The surface buoyancy flux is further diminished by the dependence of the thermal expansion coefficient α on SST (Eq. 3.2; the mean winter surface α value during the convective winters was $9.4 \times 10^{-5} \text{ }^\circ\text{C}^{-1}$, while in the shutdown winters it was $8.6 \times 10^{-5} \text{ }^\circ\text{C}^{-1}$). Thus, when convection was initially inhibited the ocean surface cooled, which restricted the surface buoyancy fluxes which in turn inhibited deep convection. There is thus a positive feedback loop which reinforces a shutdown state.

It should be noted that this positive surface temperature feedback is different from the negative temperature/salinity feedback in simple box models as Welander (1982), Lenderink and Haarsma (1994) and Kuhlbrodt et al. (2001), which restarts convection after a multiple-year nonconvective state. The most important difference between these studies and the current one is the use of a linear equation of state and thus a thermal expansion coefficient α which is independent of temperature and salinity. For the temperature and salinity range of the OWS Bravo data set α shows a range of about 0.7×10^{-4} to $1.7 \times 10^{-4} \text{ }^\circ\text{C}^{-1}$ (the range of the haline contraction coefficient β is smaller by an order of magnitude). Both a higher temperature and a lower salinity decrease the density of the seawater, but an artificially high α -value gives too much weight on the temperature dependence. When a linear equation of state is used, the influence of a higher temperature of the subsurface water on its density is therefore overestimated with respect to the effect of the low salinity in the surface layer. The stability of the observed GSA winter profiles depends critically on the value of α chosen, and in some cases an (incorrect) unstable stratification is obtained. The box models slowly warm the subsurface box in a nonconvective state, which represents the interaction with the boundary currents. Due to the linear equation of state, however, this warm water then becomes less dense than the cold and fresh water on top. This is not what happened during the GSA years, as the buoyancy of the top layer increased more rapidly than the buoyancy of the subsurface layer (Figure 3.6). This does of course not leave out the possibility that this feedback can play a role if the lateral influx conditions are different, but using a nonlinear equation of state is required to answer this question with certainty.

In this study we quantified the effects of the mild winters and the low surface salinity in the Labrador Sea during the GSA years. First the initial response of the ocean to the low surface salinity, the increasing stratification, was studied (left-hand side of the 'Ocean' box in Figure 3.5). It was shown that the stratification of the whole water column above the Labrador Sea Water (LSW) layer was not unusually large at the beginning of the winter of 1969, but instead comparable to that of winters when deep convection did take place. A notable difference with deep-convection winters however was found in the amount of buoyancy stored in the upper cold and fresh layer, which was the signature of the GSA. The stratification of this upper layer was about twice the pre-GSA value.

Second, the limiting effect of the low SST and the mild winters on the surface buoyancy flux was studied ('Atmosphere' box and 'Surface feedback loop' in Figure 3.5). Using bulk formulas it was shown that the buoyancy flux was 76% larger in the years with convection with respect to no-convection years. The effect of a harsher winter (the mean 2-meter temperature in the convective winters was -0.7 °C, while in the non-convective winters is 0.1 °C) on the heat flux (193 W m^{-2} in convective winters vs. 113 W m^{-2} in non-convective winters; Uppala et al. 2005) is much larger than the effect of a higher SST (42% vs. 21%). We found that this difference was much smaller for the buoyancy flux (42% vs. 33%), however, because of the additional α -feedback.

Using a 1D mixed layer model it was shown that neither the low surface salinity/temperature nor the mild winters alone could have prevented deep convection. In the winter of 1969 the magnitude of the winter heat flux needed for deep convection occurred only 12% of the years in the ERA40 40-year reanalysis data set. On the other hand, the magnitude of the 1969 winter heat flux would have induced deep convection in years such as 1965 and 1968, two out of the ten-winter BRAVO record. So, although in 1969 both the oceanic and atmospheric conditions made deep convection unlikely, it was the combination of the two that set off its shutdown.

The return of deep convection in the winter of 1972 is generally attributed to the very harsh winter and large surface heat flux. The 1D-model simulations showed, however, that this heat flux alone, without lateral salinity fluxes, would have been insufficient for deep convection to occur. When the lateral salinity fluxes were added to the simulation, the mixed layer depth and properties were reproduced well by the model. The source of the high salinity water cannot be identified from the data. It could have been the retreat of the GSA, and thus less fresh surface water, or eddy-induced lateral fluxes with a typical subsurface salinity maximum, or both.

So far, we have not specifically discussed the impact of wind forcing. Wind influences deep convection in two ways. The direct mixing effect is small; wind hardly mixes below several hundred meters depth, but it is included in the buoyancy flux

calculation in section 3.4.2 and the model simulation in section 3.4.3. The second effect of wind forcing, the wind stress curl effect on preconditioning, is left out as the hydrographic data showed no sign of increased doming during the GSA period.

This study has a number of implications for our understanding of the effects of fresh water anomalies on deep convection. First, although both changes in the fresh surface layer as well as the warm and salty subsurface layer can alter the likelihood of convection, during the GSA years it was primarily the freshening of the upper layer that caused the shutdown. Once deep convection had stopped, both layers contributed to a consolidation of the status quo. In the light of the recent changes in the boundary current characteristics (a warmer and more saline Irminger Current and more fresh water export from the Arctic) this is an important result. It means that, very likely, increasing ice melt in the Arctic is a larger threat to decreasing convection rates than warmer and more saline Irminger current water. Also, convection resumed due to a lateral salt influx (combined with a very harsh winter). This suggests that since anomalies like the GSA pass the ocean may naturally recover. Conversely, if the fresh water inflow remains high, deep convection will not resume. Second, it is unclear whether the unusually large heat fluxes in 1972 were a coincidence, or whether the ocean played an active role in this. For example, Våge et al. (2009) suggested that the large sea-ice extent in the winter of 2008 kept the passing winds cold, so that the air was still very cold when it reached the central Labrador Sea. Given the anomalous amount of freshwater in the surface layer and the harsh winter in 1972, a similar mechanism could have been at play then. Third, the system is apparently very sensitive to the ocean surface temperature. Once the SST is low, it will tend to remain low because of the surface feedbacks to the buoyancy flux. It is thus of vital importance in ocean and climate models to accurately simulate the ocean surface temperature and its effect on the surface fluxes, and to be particularly careful with restoring SSTs in deep convection areas towards too low or too high temperatures.

This chapter is based on: R Gelderloos, C.A. Katsman and K. Våge – “Detecting newly-formed Labrador Sea Water from space,” manuscript submitted to JGR Oceans, 2012.

Chapter 4

Detecting newly-formed Labrador Sea Water from space

I'm not concerned about all hell breaking loose, but that a PART of hell will break loose... it'll be much harder to detect.

George Carlin

Abstract

In situ monitoring of deep water formation in the Labrador Sea is severely hampered by the harsh winter conditions in this area. Furthermore, the ongoing monitoring programs do not cover the entire Labrador Sea and are often summer observations. The network of satellite altimeters does not suffer from these limitations and could therefore give valuable additional information. Altimeters can in theory detect deep water formation, because the water column becomes denser during convection and therefore the sea surface becomes lower. This signal is small compared to variability in sea surface height induced by other sources, and due to substantial eddy-induced variability a clear one-to-one relation between the local mixed layer depth and the local sea surface height variations at a given location and time is not found in the Labrador Sea. However, if properly averaged in time and space all three winters with deep convection exceeding 1500 m depth in the 1994-2009 period clearly stand out. Furthermore, for 12 out of the other 13 winters the distinction between convection deeper or shallower than 1000 m could be made. This required a thorough analysis of the data than only averaging, but careful inspection of the SSH fields distinguishes convective activity from (primarily wind-driven) gyre-scale variations.

4.1 Introduction

The Labrador Sea area is known for its very harsh winter conditions. If the winds over this part of the ocean are sufficiently strong and cold, and the oceanic conditions are not unfavorable, they can cause deep convection down to more than two kilometers depth (Marshall and Schott 1999, Yashayaev 2007). The product of deep convection, known as Labrador Sea Water (LSW), subsequently spreads into

the North Atlantic region and beyond (Talley and McCartney 1982, Bower et al. 2009). It thus partly sets the density structure at intermediate depth, and thereby plays an important role in setting the strength and shape of the Atlantic meridional overturning circulation (AMOC, Kuhlbrodt et al. 2007). This is supported by several model simulations, which have shown a strong correlation between variability in LSW formation and the strength of the AMOC on interannual to decadal timescales (Eden and Willebrand 2001, Biastoch et al. 2008).

LSW formation displays a large interannual variability. Over the period of the observational record, the mixed layer depth (MLD) showed a range of about 200 m to 2400 m (Yashayaev 2007), an order of magnitude variation. Given the important role LSW formation is considered to play in the variability of the AMOC strength, it is very important to properly monitor this substantial variability. In situ monitoring is, however, severely hampered by the harsh winter conditions on site.

Over the past decades several observational programs have been undertaken in an effort to monitor LSW formation (see Figure 4.1 for the locations of the different long-term observational programs). The first data set showing interannual variability of LSW formation was collected at the US Coast Guard's Ocean Weather Station (OWS) Bravo, which was located in the southwestern part of the central Labrador Sea. Between 1964 and 1974 regular oceanographic measurements were taken, which provided a time series that includes both winters with intense deep convection as well as a multiple-year shutdown (Lazier 1980). From 1990 onwards, a hydrographic section known as AR7W has been occupied annually by the Canadian Bedford Institute of Oceanography (Yashayaev 2007) as part of the World Ocean Circulation Experiment (WOCE). For practical reasons, the hydrographic section is usually taken in spring, summer or autumn and therefore only shows the water mass produced by wintertime deep convection. A few wintertime hydrographic observations are available as well. In particular, two winter cruises (in 1997 and 1998) were undertaken as part of the Labrador Sea Deep Convection Experiment (LabSeaGroup 1998), one of which happened to measure during active convection (Pickart et al. 2002). Earlier wintertime hydrographic programs were undertaken in 1962, 1966, 1976 and 1978 (Lilly et al. 1999). As wintertime measurements are difficult to obtain in this region, a mooring was placed on the AR7W line close to the original location of OWS Bravo. This mooring has provided an almost continuous full-depth record of convective activity at that particular location from 1996 to 2003 (Avsic et al. 2006).

A different type of observational tool is the network of autonomous profiling floats (Roemmich et al. 2009, Roemmich, D. and the Argo Steering Team 2009), which have sampled the Labrador Sea since the second half of the 1990s (Lavender et al. 2002, Våge et al. 2009). The floats descend to a prescribed pressure level and

move with the currents for a predefined number of days. They then ascend to the surface, while taking a CTD (conductivity, temperature and depth) profile. There are currently (January 2012) about 3000 autonomous floats in total spread over all ocean basins in the world, of which around 30 in the Labrador Sea. With a typical repeat cycle of 10 days in the Argo program these give around 300 profiles during the deep convection months of February to April.

The many in situ observations provide accurate and reliable information on the MLD at a certain location and a certain time, but they have a poor spatial and temporal coverage. As a result, there is not always a consensus on the depth of the mixed layer in a winter (see section 4.2 for an overview of convective activity since 1993). The one observational network that has none of these disadvantages is the satellite system: they are present throughout the year and sample the whole Labrador Sea. Although satellites cannot measure the MLD directly, they can measure the change in sea surface height (SSH) as a result of convective densification of the water column. During the deep convection season, the water density increases, causing a lowering of the sea level of several centimeters. The major part of this signal, however, is the seasonal cycle. To find out whether it is possible to detect deep convection, we should consider the additional cooling in a deep convection winter with respect to a shallow convection winter. If this additional cooling is about $0.2\text{ }^{\circ}\text{C}$ over 1500 meters (e.g. Yashayaev and Loder 2009), and we assume a thermal expansion coefficient of $1 \times 10^{-4}\text{ }^{\circ}\text{C}^{-1}$ (chapter 3), then the SSH is lowered by about

$$\Delta H = \int \alpha \Delta T dz \approx 3\text{cm}.$$

In this study the feasibility of detecting and monitoring the formation of Labrador Sea Water will be tested by comparing SSH fields (section 4.3) with the observed MLD over the past two decades, an overview of which is included in section 4.2. Using the SSH anomaly fields, we show in section 4.4 that it is possible to detect newly-formed LSW and also to give a very rough estimate of the convection depth and area. In section 4.5 we will take this one step further to try and link the MLD at a certain time and location to the SSH anomaly at that time and location, which we will show to be more challenging. The results are summarized in section 4.6.

4.2 Convective activity in the period 1993-2009

From the combined observational programs we have a reasonable idea of the interannual variability of deep convection in the Labrador Sea since the early 1990s (Table 4.1). The first years of this period were characterized by large winter heat losses and showed the deepest convection in the Labrador Sea on record (Lazier

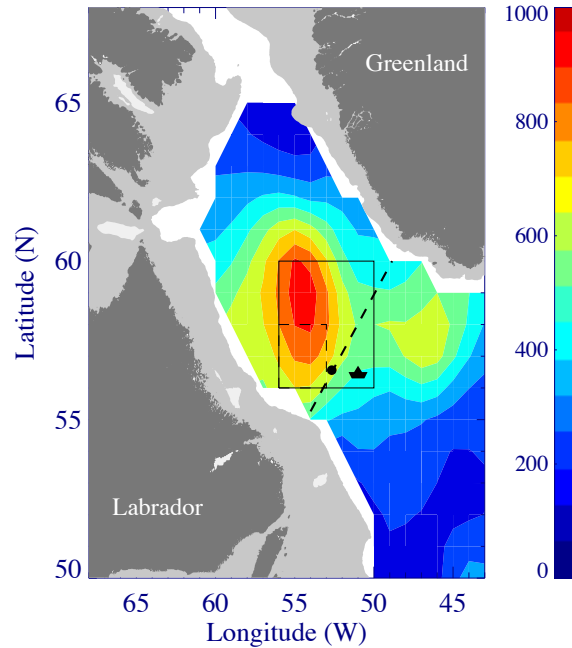


Figure 4.1: Overview of the locations of repeated measurements (the 2000-2007 mixed layer depth climatology from Våge et al. (2009) is shown in color). The dashed line across the basin is the AR7W hydrographic repeat section. The little boat is the location of Ocean Weather Station Bravo, and the black dot on the AR7W line close to Bravo is the location of the K1 mooring (see Table 4.1 for an overview of the mixed layer depths measured at these locations since 1993). The solid large and dashed small rectangles are the areas over which is averaged in sections 4.4 and 4.5. Areas shallower than 500 m are shaded in pale gray.

et al. 2002, Lilly et al. 2003, Yashayaev 2007), with the deepest mixed layers reached between 1993 and 1995. From 1996 to 1999 the winter heat loss was moderate and so mixed layers decreased in depth, causing a multiyear period of restratification at middepth. Convection was generally around 1000 m in these years (Lazier et al. 2002, Lilly et al. 2003, Avsic et al. 2006), although a local maximum MLD of 1500 m has been recorded in 1997 during a wintertime survey (Pickart et al. 2002). This short revival is corroborated by the K1-mooring record, which showed a mixed layer of 1400 m in the 1997 winter. The winter of 2000 interrupted the restratification trend with another convection winter which formed a new class of LSW (Yashayaev 2007). Despite the fact that a new class was formed, the convection does not seem to have been very deep. Yashayaev and Loder (2009) cite a maximum MLD of 1300 m be-

tween 2000 and 2003, without being specific on the convection depth in 2000, while Avsic et al. (2006) suggest an MLD of 1100 m based on the mooring data. The same mooring record shows the deepest convection in the 2000-2003 period in 2003, with a maximum MLD of 1400 m. The period between 2004 and 2007 was reasonably quiet with convection not exceeding 700 to 1100 m (Yashayaev and Loder 2009), although the mooring recorded an MLD of 1300 m in 2005 (Avsic et al. 2006). In 2008, deep convection returned with winter mixed layers of up to 1800 m depth (Våge et al. 2009). This seems so far to have been a single-year interruption of the long-term restratification period, however, as in 2009 and 2010 no deep convection has been observed.

Despite these complications, the combined database enables us to divide the winters into three categories: convection deeper than 1500 m (hereafter referred to as deep convection), convection to 1000 m or less (shallow convection), and convection between roughly 1000 m and 1500 m (intermediate convection). These depth limits may at first seem rather arbitrary, but they serve well as a first indication of the formation of LSW as 1000 m is approximately the depth over which is restratified in summer so when convection is shallower than that no renewal of LSW takes place.

From the overview in Table 4.1 it is clear that the exact depth of the mixed layer is not always agreed upon. This is not surprising, however, as the different observations were taken at different times and different locations (Figure 4.1). For example, the float profiles in the winter of 1996 are clustered around 58°N and 54°W, which is much further northwest than the AR7W line which the summer estimates are based on. Moreover, as noted by Lazier et al. (2002), internal waves and eddies can easily cause a difference of 100 m in the MLD between two measurements at different locations. Particularly large discrepancies are found in the MLD estimates for 1996, 1998, 2002 and 2005. We will come back to these years in section 4.4.5.

4.3 Sea Surface Height anomaly data: AVISO

The AVISO altimetry data center¹ provides maps of sea level anomaly, on a high spatial resolution (1/3°) and interpolated to a daily temporal resolution. We used the 'updated' delayed time series for this study, which combines as many missions available at any given time and location to obtain the best possible quality of the SSH anomaly estimate (Table 4.2). The time series is over the period of October 1992 to January 2011.

¹<http://www.aviso.oceanobs.com/en/data/products/sea-surface-height-products/global/msla/index.html#c5122>

Year	AR7W	AR7W	AR7W	AR7W	K1	Floats	Floats	Floats
	Y09	L03	L02	P02	A06	A06	Y09	V09/GKV12
1993	2400	2300	2320	-	-	-	-	-
1994	-	2000	2300	-	-	-	-	-
1995	-	2300	-	-	2300	-	-	-
1996	-	1200	≤1000	-	-	1300	-	630
1997	-	1400	≤1000	1500	1400	-	-	1420
1998	-	1000	≤1000	-	1000	-	-	1170
1999	-	900	≤1000	-	1000	-	-	1040
2000	*	-	-	-	1100	-	-	1020
2001	1300	-	-	-	1100	-	700 -	900
2002		-	-	-	1200	-	1100	690
2003		-	-	-	1400	-	1200-1300	1330
2004	-	-	-	-	-	700		820
2005	-	-	-	-	1300	-	700 -	1290***
2006	-	-	-	-	-	-	1100	990
2007	<700	-	-	-	-	-		940
2008	1600	-	-	-	-	-	1600**	1830
2009	-	-	-	-	-	-	-	790

Table 4.1: Compilation of estimates of maximum winter MLD in the Labrador Sea for 1993–2009 from various locations and sources (gray shading marks the deep convection years, dashes indicate no specific estimate in that manuscript). The estimates in the first three columns are based on summertime surveys of the AR7W section (Y09: Yashayaev and Loder (2009); L03: Lilly et al. (2003); L02: Lazier et al. (2002)). Other columns represent wintertime measurements from the 1997 winter survey (P02: Pickart et al. (2002)), the K1 mooring (A06: Avsic et al. (2006)), and float data (A06: profiles obtained near the K1 mooring + some summertime CTD stations; Y09: rough estimate for the central Labrador Sea). The final column contains estimates based on a detailed analysis of available float profiles for 1996–2001 (section 4.5.1, denoted in the table as GK12) and 2002–2009 (V09: Våge et al. 2009). *Yashayaev (2007) states that wintertime convection in 2000 reached 1600 m. **Yashayaev and Loder (2009) note that one float suggested an MLD greater than 1800 m. ***The deep mixed layer in 2005 was located just southwest of the Greenland coast.

The SSH time series display variability on different temporal and spatial scales. As the SSH signal related to a convective density change of the water column only explains a small part of the variability, filtering of the data is required. The filtering procedure is applied to every data point in the grid, but illustrated for the area-

Period	Missions used
October 1992 to August 2002	Topex/Poseidon + ERS-1 or ERS-2
August 2002 to June 2003	Jason-1 + ERS-2
June 2003 to January 2004	Jason-1 + Envisat
From January 2009	OSTM/Jason-2 + Envisat

Table 4.2: Satellite missions used in the AVISO merged altimetry product (AVI 2011).

averaged time series in Figure 4.2.

One source of SSH variation is the long-term trend (Figure 4.2a). This is the result of changing thermohaline forcing over the center of the subpolar gyre and the subsequent warming since the 1990s. This has reduced the strength of the cyclonic gyre circulation and has resulted in a gyre-scale long-term positive trend in the SSH time series (Häkkinen and Rhines 2004). This trend is removed from the SSH fields by subtracting the one-year running mean from the original SSH time series at every grid point. The resulting detrended time series is shown as the dashed line in 4.2b.

Apart from the long-term trend a second gyre-scale source of variability is evident in the time series, which is the seasonal cycle (Figure 4.2b). This is caused in part by changes in the strength of the gyre circulation as a result in increasing and decreasing wind stress curl, and in part by thermohaline forcing, mainly surface heating and cooling. As our time series contains years with deep convection as well as shallow and intermediate convection, we expect the winter values from the mean seasonal cycle (solid line in Figure 4.2b) to be consistent with intermediately-deep mixed layers. We are thus interested in the deviation from the mean seasonal cycle, i.e. the difference between the dashed and the solid lines in Figure 4.2, where we expect a large negative wintertime anomaly to be an indicator of deep convection. Note that the climatological fields were spatially smoothed in both directions with a one-degree boxcar filter.

The last form of variability is small-scale and not coherent in space or time. This noisy pattern of positive and negative SSH values is mainly caused by eddies. In particular the larger Irminger Rings (a typical radius of 25 km, see chapter 2) have a non-negligible dynamical sea surface anomaly signal ($\mathcal{O}(10\text{cm})$; Lilly et al. 2003). The SSH values depend on the sense of rotation of the eddy, where anticyclonic eddies cause positive anomalies and cyclonic eddies negative anomalies.

The eddy-induced 'background noise' is removed from the fields by averaging over time and over subregions of the Labrador Sea (see section 4.4 for details). This procedure is justified for our purposes, because deep convective mixing takes place in convective plumes on a very small horizontal scale of about 1 km, but during

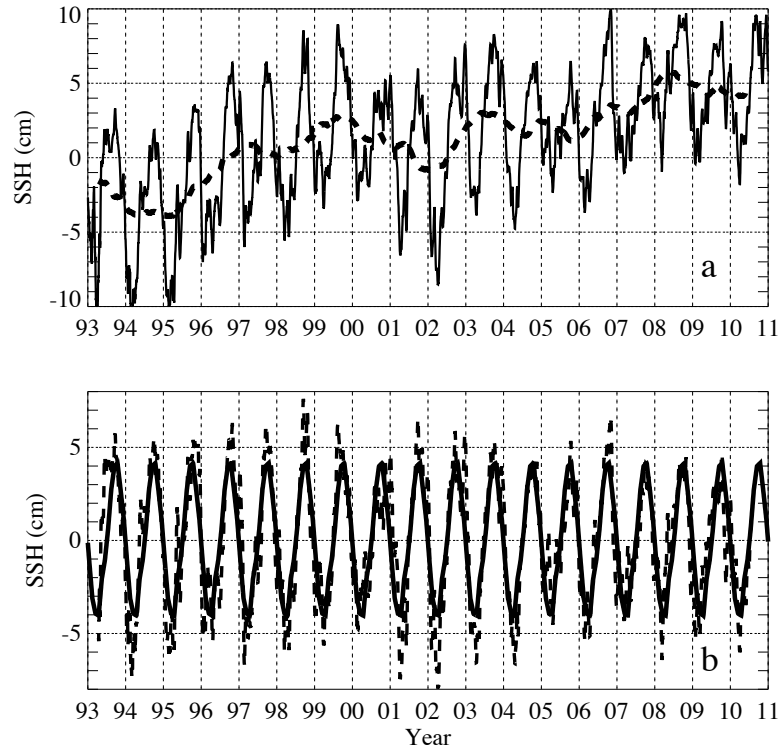


Figure 4.2: Filtering of the original SSH data to obtain the SSH anomaly (all time series are the average over $56\text{--}60^{\circ}\text{N}$ and $56\text{--}53^{\circ}\text{W}$, the large rectangle in Figure 4.1). (a) Original time series (solid line) with the 1-year running mean overlaid (dashed line). (b) Detrended time series: The dashed line is the difference between the two timeseries in panel a. The solid line is the mean seasonal cycle of the detrended time series. The analysis is performed on the difference between the detrended time series (dashed line in panel b) and the mean seasonal cycle (solid line in panel b). This quantity will be called 'SSH anomaly'. Note that the area-averaged time series shown in this figure only serve to explain the filtering method used. In the analysis the filtering is performed on each data point in the grid individually.

convection as well as directly following the event, violent lateral mixing homogenizes nearby plumes with the more stratified water in between into a homogeneous dense mixed patch or 'chimney', typically tens of kilometers to more than 100 km in diameter (Marshall and Schott 1999, see also section 1.2). It is therefore not necessary to catch the individual plumes in order to be able to detect deep convection. It is sufficient to detect the chimneys. Note that the chimneys are also much larger

than eddies so that the two features can easily be distinguished in an SSH anomaly map.

4.4 Detecting newly-formed Labrador Sea Water using altimetry

4.4.1 Visual inspection: detecting the chimney

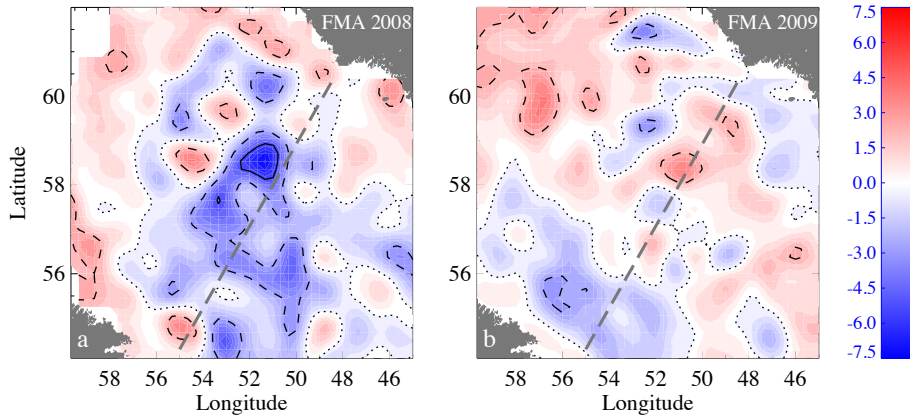


Figure 4.3: SSH anomaly (SSH minus long-term trend minus the mean seasonal cycle; see text in section 4.3) in cm, averaged over February to April. (a) A deep convection winter (2008) and (b) a shallow convection winter (2009). Greenland (in the northeast) and Labrador (in the southwest) are indicated in gray. The AR7W hydrographic section is added for reference as the thick gray dashed line from Labrador to Greenland. The zero-contour is dotted, the -2.5 and $+2.5$ cm contours are dashed, and the -5 and $+5$ cm contours are indicated by a solid black line.

As a first indication whether or not deep convection occurred in a winter, we take a look at the winter-mean (February-April) values of the SSH anomaly fields to see if the chimneys are visible. If so, they should show up as a relatively large area of strongly negative SSH anomalies. A map of the SSH anomaly in the only deep-convection winter of the past decade (2008) immediately reveals the deep convection area (Figure 4.3a) as a large dark blue patch of negative SSH anomalies larger -2.5 cm, roughly between 56 and 59°N and 55 and 50°W . The deep convection site is surrounded by a noisy pattern of positive and negative anomalies of slightly smaller amplitude, which is caused by eddies in the basin. The same map for the winter of

2009, on the contrary, only shows this noisy pattern and has no large-scale coherent negative anomaly. This is consistent with the fact that 2009 was a known shallow-convection winter (Table 4.1).

4.4.2 Time and space-averaged SSH anomalies

Based on the example in Figure 4.3 one would expect that the mean SSH anomalies in a deep convection winter, if averaged over a suitably chosen area, will be significantly more negative than in shallow convection winters. This is shown in Figure 4.4 for the two rectangular areas highlighted in Figure 4.1, averaged over February and March (solid squares) and February to April (open squares). The known deep convection winters (1994, 1995, and 2008) stand out by their large negative SSH anomaly. Also, well-known shallow-convection years (e.g. 1999 and 2001) clearly show a positive anomaly.

Convection of intermediate depth is more difficult to diagnose, partly because the winter-mean anomaly depends on the area over which the average is taken. For example, in the small rectangular domain in the southwestern part of the Labrador Sea (Figure 4.4b) the negative SSH anomaly in 1997 was much larger than in 2000, while the averages over the large rectangular area, representative for the southern Labrador Sea (Figure 4.4a), show comparable anomalies. Apparently, the MLD was large in the southwest corner of the Labrador Sea in 1997, but averaged over the larger domain a similar densification has taken place.

Two winters, 2003 and 2006, show unsatisfying results. According to in situ measurements (Table 4.1), 2003 was an intermediate convection winter, but the SSH anomaly is surprisingly positive. In contrast, the evidence suggests 2006 to have been a shallow convection winter, yet in this year a negative wintertime SSH anomaly is observed. Both of these cases seem to be independent of the area over which is averaged (Figure 4.4). We will get back to these winters when looking at the time dependency of the SSH anomaly (sections 4.4.3 and 4.4.4).

In summary, using straightforward temporal and spatial averaging, only 2 out of 17 winters show results inconsistent with *in situ* observations. Furthermore, all three deep convection winters are easily identified.

4.4.3 Time-dependent SSH anomalies

The Hovmöller diagrams in Figure 4.5 show the latitude and time variation of the SSH anomalies in the southwestern part of the Labrador Sea (cf. Figure 4.4b). The deep convection winters, indicated by a solid rectangle surrounding the panel of that year, clearly show prolonged and coherent negative anomalies. This is particularly true for 1994 and 2008. 1995 also shows a large-scale prolonged negative

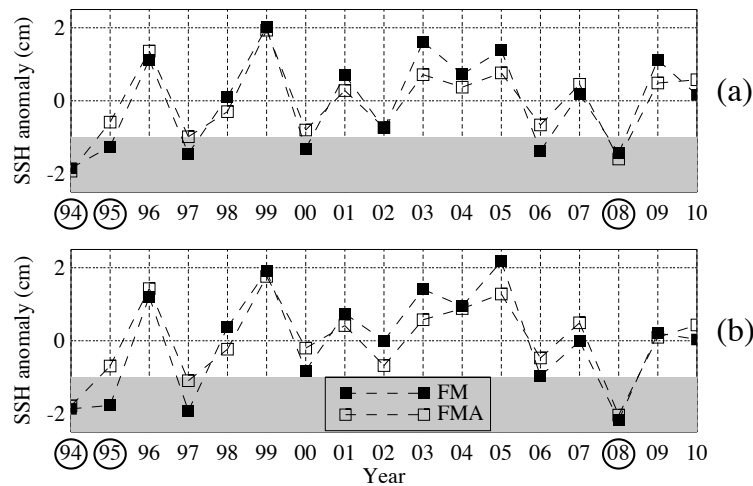


Figure 4.4: Multimonth mean SSH anomaly per year averaged over (a) $56\text{--}60^\circ\text{N}$ and $56\text{--}50^\circ\text{W}$, the large rectangle in Figure 4.1 and over (b) $56\text{--}58^\circ\text{N}$ and $56\text{--}53^\circ\text{W}$, the small rectangle in Figure 4.1. Negative SSH anomalies larger than -1 cm are shaded to help visual inspection. Deep convection winters are highlighted by a circle around the year on the axis. Note that we lost one year of data on both sides of the time series due to subtraction of the one-year running mean.

anomaly, but only until mid-March rather than mid-April, after which the signal is more variable. This very nicely reflects the fact that the winter of 1995 was not a particularly harsh one (Uppala et al. 2005); the convection was mainly so deep because this winter was preceded by a deep convection period lasting multiple winters in a row. Apparently, there was deep convection in February, but no more convective densification in March and April than in an average winter.

The intermediate convection winters (1997, 2000 and 2003; indicated by a dashed frame in Figure 4.5) are characterized by negative anomalies of a similar latitudinal extent and amplitude as in the deep convection winters, but of shorter duration. The reason for the seeming very large positive SSH anomaly in 2003 in Figure 4.4 now immediately becomes clear: it originates from a very high positive anomaly in the first half of February. The SSH anomaly during the rest of the winter is comparable to, for example, 2000. In this case, it is thus very important to look at the time evolution of the SSH anomaly before drawing conclusions: from mid February onwards 2003 was definitely an intermediate-convection winter, in line with the conclusions from in situ observations (Table 4.1).

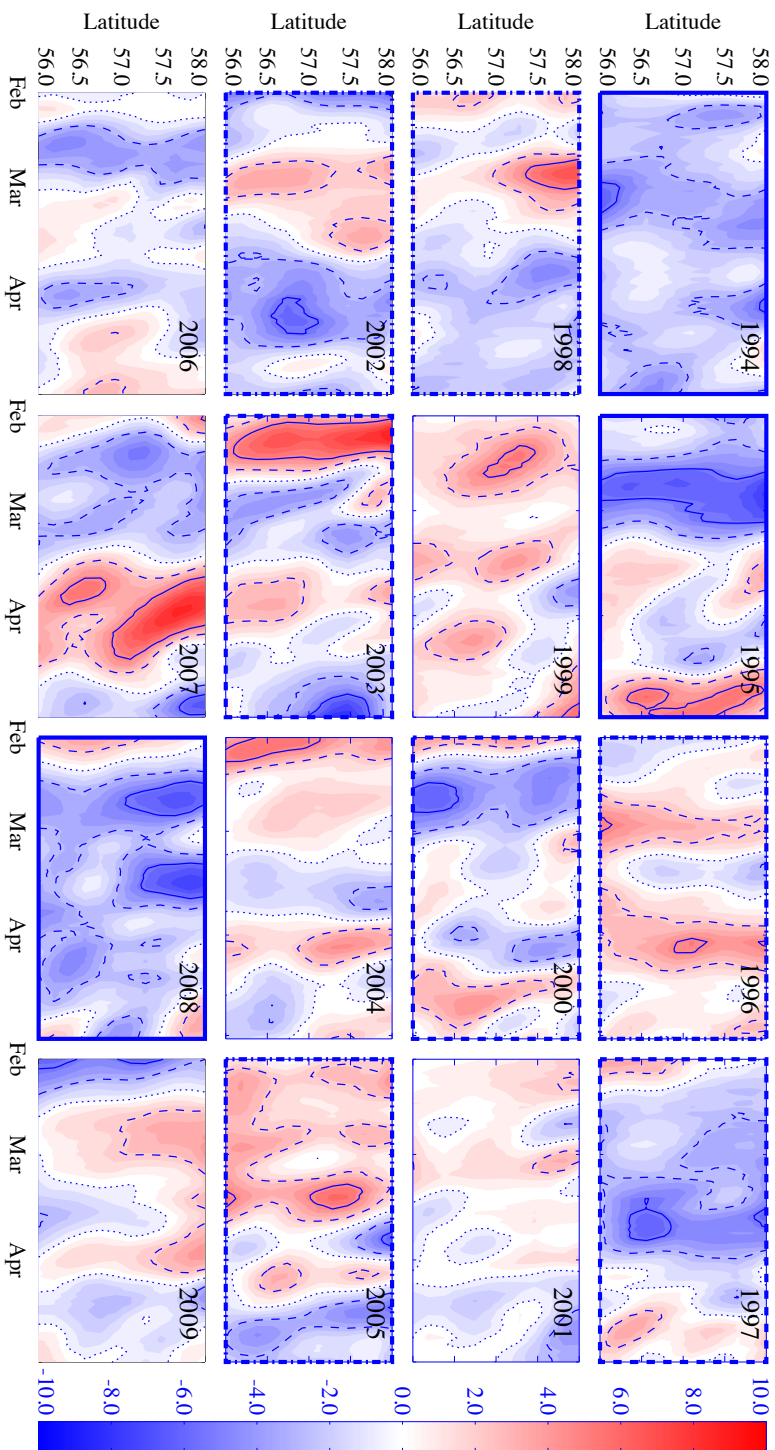


Figure 4.5: Hovmöller plots of the SSH anomaly (cm) for 1994 to 2009, zonally averaged over 56–53°W (small rectangle in Figure 4.1). Winters with deep convection are surrounded by a thick solid frame, intermediate-convection winters are indicated by a dashed frame, and shallow-convection winters have no frame. The four winters on which literature is not conclusive whether intermediate of shallow convection took place have a dash-dotted frame. The contour levels are as in Figure 4.3.

Four of the six shallow convection winters (no frame; 1999, 2001, 2004 and 2009) show only weak negative anomalies (fade shades of blue) or positive values (red and pink shades), as expected. The other two shallow convection winters, 2006 and 2007, can be classified as either shallow or intermediate convection winters, based on a comparison with the other panels in Figure 4.5.

Out of the 12 winters under consideration that have an undisputed convective regime (see Table 4.1), there are thus only 2 winters that are classified as shallow based on the *in situ* observations for which the SSH anomaly analysis suggests a different convective regime (intermediate). These winters, 2006 and 2007, are examined below.

4.4.4 When altimetry seems to fail: 2006 and 2007

For the winter of 2007 the explanation for the discrepancy between the altimetric SSH anomaly and the *in situ*-measured MLD is straightforward. In February and early March of that year, the entire gyre was lower than average (Figure 4.6a), in contrast to a chimney-like feature in a deep convection year (see Figure 4.3a). At the same time, an exceptionally large wind stress curl is observed around the southern tip of Greenland and spread over the Irminger Sea and the southern part of the Labrador Sea (Figure 4.6b). It can be expected that such a large wind stress spins up the cyclonic circulation of the gyre, yielding a negative SSH anomaly over a large area, consistent with the observations. The large negative SSH anomaly in 2007 is thus a wind effect and not the result of convective densification. This type of results is thus easily eliminated by considering a larger area.

Explaining the negative anomaly in the winter of 2006 is more difficult. In the monthly-mean SSH anomaly maps (Figure 4.7), only in February two chimney-like features can be discerned. The floats showed no deep mixed layers in the 'chimney' around 60°W and 53°W. At the location of the second chimney-like feature, centered around 57°N and 52°W, the profiling floats recorded mixed layers around 800 m. The fact that the SSH anomalies in March and April are comparable to normal values for the time of the year also indicates that, if convection took place in February, it did not reach very deep. This is confirmed by the lack of newly-formed deep water on the AR7W line in spring. One possible explanation is that the dip in sea level is not a chimney, but a cluster of cyclonic eddies which all remain fairly stable at the same position during the month of February. This is not very likely, however, as the larger eddies in the Labrador Sea are predominantly anticyclonic (Lilly et al. 2003). Another possibility is that an increased wind stress curl over the Irminger Sea, East of Greenland (known as a Greenland tip jet; Pickart et al. 2003), induced a cyclonic recirculation gyre extending into the Labrador Sea as described by Spall

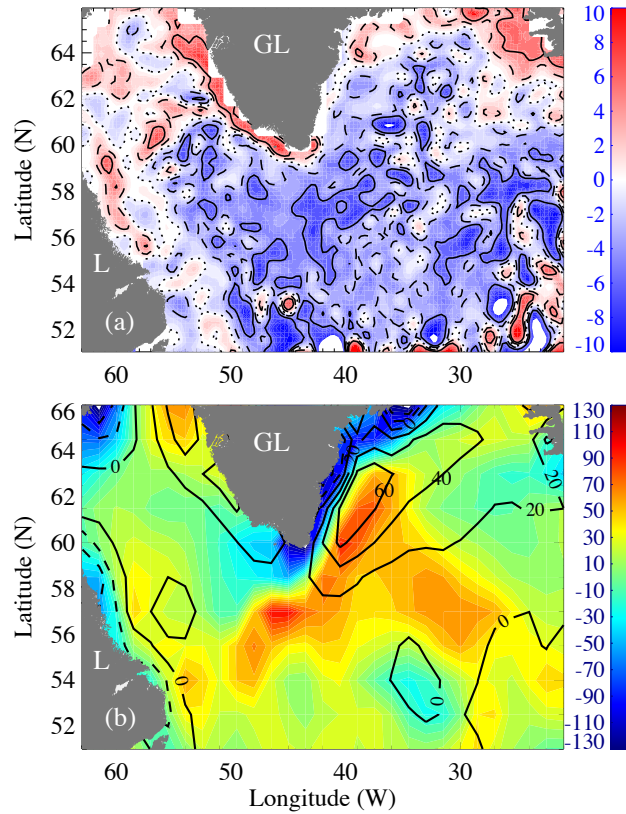


Figure 4.6: (a) February-mean SSH anomaly in 2007. (b) Wind stress curl fields ($N/m^3 \times 10^{-8}$) calculated from the ERAinterim time series (Dee et al. 2011). In color is the mean wind stress curl over February 2007. The climatological February wind stress curl over 1993 to 2009 is overlaid in contour lines. GL = Greenland; L = Labrador.

and Pickart (2003). Indeed, according to the wind stress data from the ERA-interim reanalysis a number of high wind stress curl events occurred in this region between late January and half March (Dee et al. 2011). As the increased wind stress curl events were localized, a spinup of the entire gyre such as in 2007 would not have occurred. Nevertheless, as for 2007, we suspect that local wind effects played a role in lowering the sea surface in this winter.

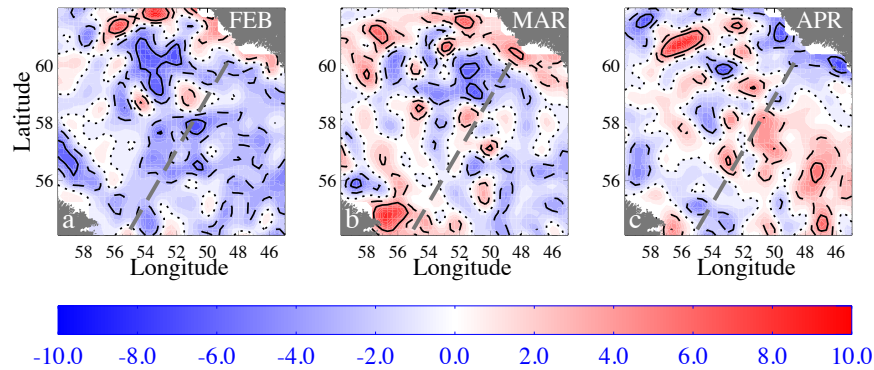


Figure 4.7: Monthly-mean SSH anomaly maps of 2006. (a) February; (b) March; (c) April. The continents, AR7W line and contours are as in Figure 4.3.

4.4.5 When in situ monitoring programs disagree: 1996, 1998, 2002 and 2005

As discussed in section 4.2, for four winters in the past two decades the in situ observations disagree on whether the convective regime was shallow or intermediate. These winters are indicated by a dash-dotted frame in Figure 4.5. With the knowledge from the analyses of the SSH anomalies of all winters we can now estimate the convective regime in these winters. Both 1998 and 2002 show coherent negative anomalies in the Hovmöller plots (Figure 4.5) during March and April, such as can be found in 1997 and 2000. The timing and spatial extent of these negative anomalies indicate that these two years had an intermediate convection regime, consistent with the moderate negative winter-mean SSH anomalies in these two years (Figure 4.4).

In contrast, the Hovmöller diagrams of 1996 and 2005 show mainly positive and very weak anomalies, the only exception being the second half of April 2005. This negative anomaly, however, does not appear to represent one but two features, the size of which resemble the dimensions of an eddy rather than those of a chimney. Furthermore, the anomaly is very late in the convection season, as convective densification is typically largest in February and March. Overall, the winter-mean SSH anomalies in 1996 and 2005 were large and positive, indicating that these years likely had a shallow-convection regime. The SSH anomaly fields can thus successfully help solve the disagreement between *in situ* observations.

4.5 Potential of altimetry as a monitoring tool

In the previous section we showed that, by averaging the satellite altimetry data in several different ways and careful consideration of the resulting patterns and evolution, winters can be classified as deep, intermediate and shallow convective regimes (Figures 4.4 and 4.5). Also, the area where convective densification has taken place can roughly be located (Figure 4.3a). A more ambitious goal is to not only *detect* newly-formed deep water using satellite altimetry, but to use it as an operational tool to *monitor* where and when deep convection takes place in the Labrador Sea. The difficulty here is that the signal of convection in the SSH anomaly fields (a range of about 4 cm, see Figure 4.4) is typically smaller than the (mostly eddy-induced) background noise. The averaging procedures in section 4.4 suppress the noise, which make detection feasible.

To be able to operationally monitor LSW formation with satellite altimetry, a tight relation between the *local* SSH anomaly measured by the altimeter and the *local* depth of the mixed layer must exist, without averaging in time and space. In this section we will test this relation by correlating in situ-measured MLDs with the SSH anomalies measured by the altimeter. The MLDs are derived from float profiles obtained between 1996 and 2009, and the stations from the winter cruise in February/March 1997 (Pickart et al. 2002). The procedure for deriving the MLDs is explained in section 4.5.1. Then the correlation between SSH anomaly and the depth of the mixed layer is studied in section 4.5.2.

4.5.1 Float-based mixed layer depth

As part of the World Ocean Circulation Experiment (WOCE), the Labrador Sea Deep Convection Experiment and later as part of the Argo program the interior Labrador Sea has been sampled by autonomous profiling floats (LabSeaGroup 1998, Laverder et al. 2000, Straneo 2006a, Våge et al. 2009). The floats give information on the temperature and salinity distribution, from which the depth of convection in winter can be derived. From 1997 to 1999 and from 2005 to 2009 the spatial coverage during the deep convection season (February to April) is rather good (typically 50 to 150 profiles per winter, with a fair coverage of the central Labrador Sea). Some profiles are available as well for the winters of 1996 and 2000 to 2004 (typically 10 to 50 profiles per winter, with only a limited spatial coverage). Figures 4.8a and b show an example of a poorly sampled winter and a well sampled winter, respectively. A complete overview of the number of floats per winter is given in Table 4.3. A total number of 1104 profiles were included in the analysis.

Year	# Float profiles			
	Feb	Mar	Apr	Total
1996	3	4	3	10
1997	19	20	12	51
1998	55	70	58	183
1999	21	17	15	53
2000	8	6	6	20
2001	3	3	3	9
2002	1	4	6	11
2003	18	31	26	75
2004	20	21	18	59
2005	34	36	33	103
2006	35	47	42	124
2007	52	54	53	159
2008	31	37	35	103
2009	35	29	27	91

Table 4.3: Number of float profiles in the area between 65-42W and 52-65N (Figure 4.8a and b), per year per month.

Pickart et al. (2002) determined the MLD from the stations during the winter cruise in 1997 as follows. First, a subjective estimate of the MLD was made by visual inspection of the potential density profile. Then, the mean density and the standard deviation were computed over the depth range of the subjectively estimated MLD. The two-standard deviation envelope was then overlaid on the potential density profile and the MLD was determined as the depth where the profile permanently crossed outside of this envelope. In a later study, Våge et al. (2009) used the same method to determine the mixed layer depth (MLD) of the floats in the Labrador Sea that were part of the Argo program (winter data in the Labrador Sea in 2002-2009). Here we expand the MLD record using the floats deployed as part of WOCE and the Labrador Sea Deep Convection Experiment (Lavender et al. 2005), which provided winter profiles in the Labrador Sea between 1996 and 2001.

Before comparing the in situ-measured MLDs with the altimetry-derived SSH anomaly, an additional step had to be taken. The spatial spreading of the float profiles is always different. This is especially a problem when a float is trapped inside a cyclonic eddy, because this links the MLD in the eddy (which need not be large) to the large negative SSH anomaly of the eddy. To avoid these (and other) spurious matches from dominating the overall correlation between the MLD and SSH

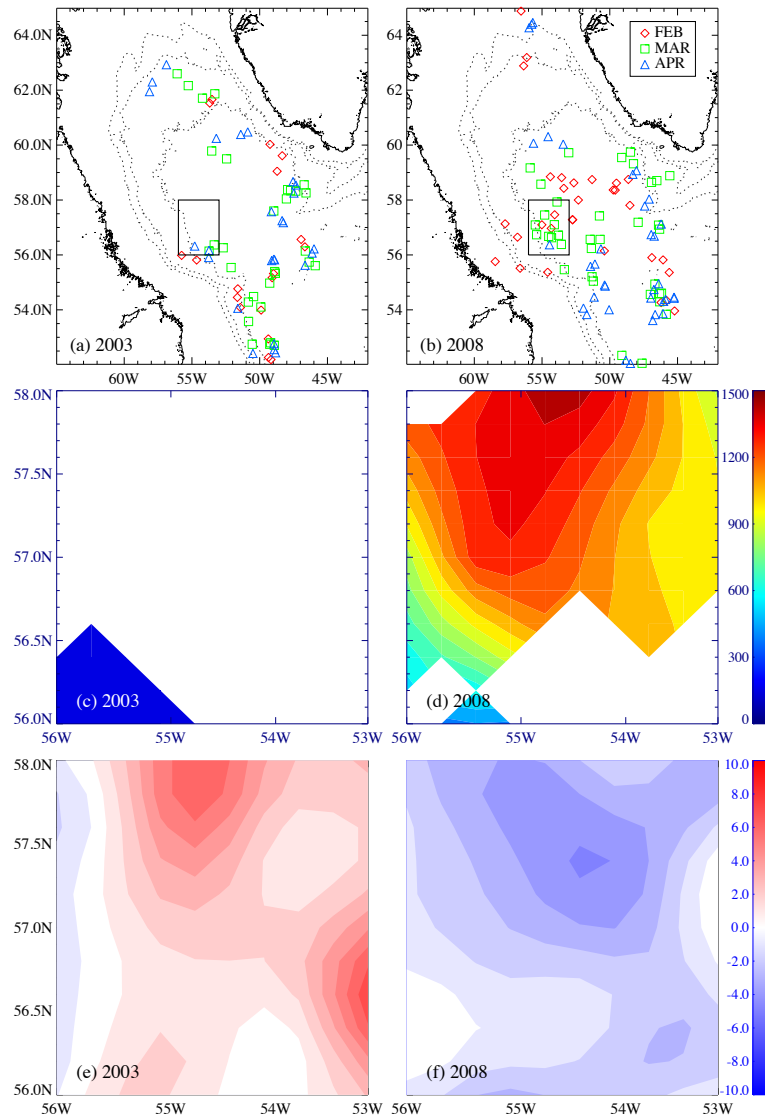


Figure 4.8: Locations of float profiles in the months of February, March and April in (a) a year with poor coverage in the central Labrador Sea (2003) and (b) a year with good coverage in the central Labrador Sea (2008). See Table 4.3 for the number of profiles on these and other years. The area in panels (c) to (f) is indicated in panel (a) and (b) by a rectangle. (c) Interpolated MLD map from the float profiles in February 2003 and (d) February 2008. (e) The SSH anomaly maps of February 2003 and (f) February 2008.

anomaly, we interpolated the in situ measured MLDs onto the same grid as the SSH anomaly fields to obtain MLD maps (Figures 4.8c and d). For this interpolation an optimum had to be found between a minimum of temporal averaging (as too much averaging would be useless from an operational point of view) and a minimum distance between floats used for the interpolation (as large distances make the interpolated map unreliable). Based on a subjective evaluation, we found that a month was the minimum time period required to have enough profiles to make a map. Naturally, these maps do still not cover the entire Labrador Sea and also in the area we use for the analysis 'white spots' remain, i.e. grid points too far away from the nearest float or CTD station (white areas in Figures 4.8c and d). After making the maps, the SSH anomaly maps (Figures 4.8e and f) are subsampled on the valid data points from the MLD maps, i.e. the areas not covered by 'white spots', for further analysis.

4.5.2 Relating SSH anomaly to mixed layer depth

First, every valid grid point (non-white grid points in Figures 4.8c and d, and equivalent for all other years and months) of the MLD maps were plotted against the accompanying SSH anomaly (Figures 4.8e and f). The result is shown in Figure 4.9a. The correlation between the SSH anomaly and the MLD is -0.26, which means in physical terms (which is also immediately clear from the figure) that the local SSH anomaly is not a good indicator for the local MLD in a certain month. Apparently, the averaging procedures from section 4.4 are indeed necessary to separate the convective densification signal from the eddy-induced variability. This is shown in Figure 4.9b. Here, the valid points from the maps like Figure 4.8c and d are averaged over the southwestern part of the Labrador Sea (area indicated in Figure 4.8) and compared to the accompanying averaged SSH anomaly value. This increases the correlation to -0.4. This is still not sufficient, however, to be able to use the altimeter for operational monitoring purposes. Averaging to suppress small scale variability and a certain amount of expert judgment (section 4.4) are required to determine the convective regime.

4.6 Summary and Conclusions

From the combination of the winter-mean sea surface height (SSH) anomalies (Figure 4.4) and Hovmöller diagrams of these SSH anomalies (Figure 4.5) we have shown that it is possible to detect newly-formed Labrador Sea Water (LSW) from altimetry data and to estimate whether the wintertime mixed layer depths (MLDs) from 1994 to 2009 were deep (>1500 m), shallow (< 1000 m), or intermediate (be-

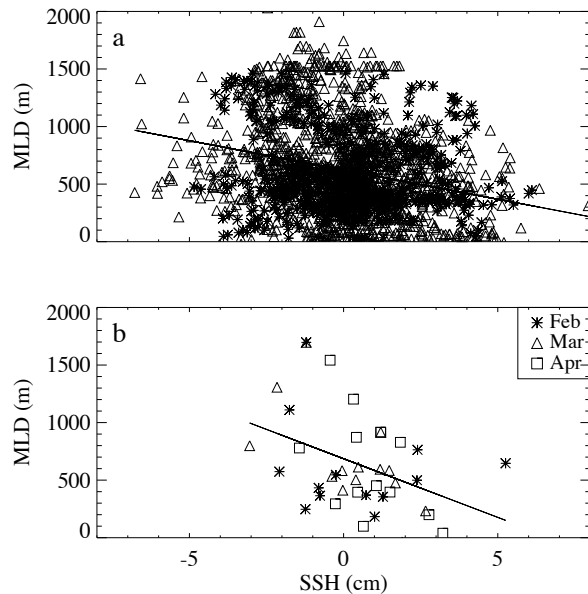


Figure 4.9: Relation between in situ measured MLD and the SSH anomaly from altimetry data. (a) Scatterplot showing all valid data points between 56 and 58°N and 56 and 53°W (small rectangle in Figure 4.1) from the gridded MLD monthly maps. (b) As (a), but now the values are first averaged over 56 to 58°N and 56 to 53°W . This improves the overall correlation from -0.26 to -0.4 .

tween roughly 1100 and 1400 m). The reason we make the distinction between shallow and intermediate convection is because most of the literature on deep convection is in terms of MLD, while the altimetry measures the change in density. These are, of course, strongly related, but a winter following a restratification period of multiple years requires a larger densification of the water column to mix convectively to a certain depth. It is therefore useful to make a distinction between convection which can produce a traceable amount of LSW (the intermediate convection winters in our study), and that which can not (shallow convection).

The most interesting winters are the winters deep convection winters, which ventilate the deeper layers of the Labrador Sea. These winters can be easily and irrefutably singled out based on satellite altimetry data alone. Most of the intermediate and shallow convection winters are easily identified as well. For some winters, however, spatial maps and expert judgment are required to draw the correct conclusion. In one winter, the winter of 2006, all analyses of the SSH anomaly suggest an

intermediate convection winter, while no such convection has been reported from in situ measurements. For all other winters, however, the SSH anomaly fields were consistent with the in situ-measured MLD.

In an earlier study Herrmann et al. (2009) suggested the possibility to monitor deep convection in the northwestern Mediterranean Sea using satellite altimetry. Their study is based on the same basic concept as ours, but differs on some essential points. In particular, Herrmann et al. (2009) used a model hindcast to find a (linear) relation between deep convection and the local SSH anomaly. Assuming this relation would hold for the observations in the real ocean as well, they estimated the MLD based on satellite altimetry data. However, it appears that this relation does not always hold, not even in their model simulations (see for example the large negative anomalies north of point 'B' in the lower panel of their Figure 1e, which do not correspond to a deep mixed layer). Furthermore, it is assumed that the location of the deepest mixed layer in the model is exactly the same as in reality. Certainly in the Labrador Sea, there is quite some variability in the location where the deepest convection occurs (Våge et al. 2009). We found no simple linear relationship between the local MLD and local SSH anomaly in the Labrador Sea. Detection of newly-formed LSW is only possible if spatial and temporal averaging is applied first. Therefore, satellite altimetry can not be used to monitor the formation of LSW for operational purposes, and the approach of Herrmann et al. (2009) will not provide reliable results in the Labrador Sea case.

We have shown that satellite altimetry can be used successfully to detect newly formed deep water and roughly indicate the location. This does not mean that in situ measurements have become superfluous, and conclusions based on altimetry need to be interpreted with care. The major advantage of using satellites for the detection of deep convection is their high temporal resolution and large spatial coverage, which enable detecting the occurrence of deep water formation away from the annual hydrographic repeat section. This information can be used to guide research vessels. When applied in this way, satellite altimetry is thus a very useful and valuable addition to the efforts to monitor variability in deep water formation in the Labrador Sea.

Chapter 5

Conclusions and Outlook

The aim of this dissertation was to increase the understanding of some of the physical processes affecting the formation of Labrador Sea Water (LSW) on one hand, and to investigate the possibilities of increasing the monitoring potential of LSW formation, using satellite altimetry observations, on the other hand. In this chapter the main results from this dissertation are summarized, and recommendations are given for what future work on this topic should focus on.

5.1 Conclusions on the process studies

The first of two process studies considered the roles of different eddy types in the restratification process after deep convection (chapter 2). Restratification, or replenishment of densified water by more buoyant water through lateral fluxes to re-establish the stratification, is one of the key factors determining the variability of LSW formation. This process is active year-round, but particularly prominent in the spring season directly following deep convection. In these spring and early summer months, three different eddy types efficiently carry buoyant boundary current water into the interior and mix the central Labrador Sea.

Using a numerical model in a highly idealized configuration of the Labrador Sea, the roles of three different eddy types, that had been identified in previous studies to be important for restratification in this area, were studied and quantified. Two of these eddy types, Convective Eddies and Boundary Current Eddies, are relatively small eddies that are formed through baroclinic instability of a front. In case of the former, this front is between the convection area and the more stratified water outside this area. In case of the latter, this front is between the boundary currents and the interior Labrador Sea. It was found that these two eddy types together replenish 30% of the heat lost during a deep convection winter over a restratification period of six months. The third eddy type, Irminger Ring, is very different. These eddies are much larger (a radius of typically 25 km instead of around 10 km for the other two eddy types) and are formed at one specific location along the western coast of Greenland, where the boundary current becomes unstable due to the steepness

of this stretch of bathymetry. It is found that the eddies of this type replenish an additional 45% of the heat lost in the deep convection winter over a period of six months. Furthermore, Irminger Rings are found to be very efficient in stirring the interior basin, which may enhance the efficiency of the smaller eddies in the restratification process. The presence of this eddy type is thus essential for a realistic rate of restratification.

The second process study (chapter 3) focused on quantifying the effects of a low surface salinity on LSW formation. For this study a specific case was selected, of which it has long been suggested that the very low surface salinity inhibited deep convection (Dickson et al. 1988), but which had never been studied in detail. This case study covers the period of 1964 to 1974 and in particular three winters without deep convection (1969 to 1971) and the year when deep convection returned (1972). During this period, the Ocean Weather Station Bravo, located in the southwestern Labrador Sea, established a continuous, year-round data set of *in situ* oceanographic observations. This data set is the only record available to date that shows a complete shutdown of deep convection for multiple winters in a row. Furthermore, these shutdown years are characterized by a low surface salinity (known as the 'Great Salinity Anomaly') as well as very mild winters. The effects of both these factors on the absence of deep convection were quantified.

A low surface salinity increases the stratification of the water column. This means that a larger buoyancy flux to the atmosphere is required in winter to densify the upper layers. Therefore, a sufficiently large salinity anomaly could inhibit deep convection. From the oceanographic measurements at the beginning of the shutdown period, it was found that, although the total amount of buoyancy stored in the layers above the LSW layer was not larger than during some deep convection winters, the stratification of the upper cold and fresh layer was twice as large as in the years before the shutdown period due to the presence of the Great Salinity Anomaly. However, using a 1D mixed layer model it was shown that this increased stratification was in itself not sufficient to stop deep convective mixing; it was the combination of the increased stratification (due to the low surface salinity) and the mild winter that set off the shutdown.

Once the shutdown was initiated, however, two previously unknown surface feedbacks were found to reinforce the shutdown state. As a result of the convective shutdown, the surface layer was not mixed with the subsurface warm and saline layer, and the surface temperature decreased. The low sea surface temperature reduced the heat flux to the atmosphere. Moreover, the surface value of the thermal expansion coefficient was lowered, which reduces the surface buoyancy flux even more. It was found that the lack of upward mixing of warm water reduced the surface heat flux by 21% and the surface buoyancy flux by 33%. The effect of the mild

winter on the surface fluxes was, however, still larger. Typical winter conditions from a deep convection winter would have yielded a 42% larger surface heat flux (and thus also a 42% larger surface buoyancy flux).

During the convective shutdown the interior Labrador Sea became more and more stratified and the fresh water was not mixed to depth. Therefore, a return of the convective cycle became more and more difficult. Still, in 1972 deep convection resumed. It was found that this was the result of a combination of the exceptionally harsh winter and lateral salinity fluxes.

5.2 Detecting LSW formation from space

Due to the harsh winter conditions, monitoring LSW formation using *in situ* measurements is an observational challenge. Furthermore, the *in situ* observations are very limited in their spatial and temporal coverage. Satellite altimetry observations do not have these disadvantages, but they can not measure the properties of the ocean at depth in detail. Nonetheless, they could in theory detect the lowering of the sea level as a result of convective densification of the water column. Whether this works in practice is studied in chapter 4.

As the convective densification signal is small compared to other sources of sea surface height variability, it was found not to be possible to link the mixed layer depth at a certain location and time to the sea surface height anomaly at that location and time. However, if averaged over the convection season, the convective chimney can be detected as a relatively large, coherent negative sea surface height anomaly. In particular, from the 1993-2009 period studied the three winters with convection deeper than 1500 m were easily and irrefutably singled out based on the satellite altimetry data. For all but one of the other winters, the distinction between convection deeper or shallower than 1000 m could be made.

In conclusion, the convective regime (deep, shallow or intermediate) and the location of the convection area can roughly be estimated from satellite altimetry data. As they cover the whole Labrador Sea at a good temporal resolution, they give a more complete picture of the convective activity in the Labrador Sea winter than the *in situ* observations. Also, they can be used to guide summertime ship-based surveys to the location of deepest convection. These data thus provide a very valuable addition to the *in situ* measurement programs.

5.3 Outlook

Although this dissertation has contributed some important pieces to the puzzle, quantification of all the processes that determine the variability of LSW formation is an important future task. Both the methods that could be used and the processes such studies could focus on are now discussed.

The primary outstanding question is how changes in the surface buoyancy flux affect LSW formation *given* certain representative boundary current characteristics, versus how changes in the boundary current characteristics affect LSW formation *given* a certain characteristic surface buoyancy flux. In particular, a stronger boundary current will have competing effects. It will cause increased doming of the isopycnals at the center of the cyclonic gyre, which will bring denser waters to the surface and thus enhance the formation of LSW. On the other hand, it will also increase the interior-boundary current density gradient, which will increase the restratification. Furthermore, a stronger boundary current may shed more Irminger Rings, which will also enhance restratification.

Second, the contribution to restratification of the upper two layers, above the LSW layer, should be investigated. The upper layer, which occupies the upper ca 200 m, is fed by boundary currents carrying water of Arctic origin and is therefore fresh and typically cold (although in summer solar insolation raises its temperature). The subsurface layer contains water from subtropical origin and is hence relatively warm and saline. The characteristics of these layers are strongly influenced by the characteristics of the boundary currents that feed them. Changes in the characteristics of the boundary currents, typically caused by remote processes, thus influence the variability of LSW formation. In chapter 3 of this dissertation it was shown that during the Great Salinity Anomaly years the upper fresh and cold layer gained buoyancy quicker than the subsurface warm and saline layer. However, this need not always be the case. In particular, the effects of the recent warming trend in the subpolar gyre versus increased ice melt from the Arctic Ocean and Greenland should be investigated.

Last, the exact link between variability of LSW formation and the Atlantic overturning circulation should be investigated in detail. Still much is unknown about this relation and especially about the relation between dense water formation and net sinking. In particular, while convective mixing close to a steep topographic boundary would induce sinking (Spall and Pickart 2001), interaction between convected water in the interior and a stratified boundary current would also induce sinking (Straneo 2006b). This line of study is complicated by the fact that global models, required to model variability in the overturning circulation, generally do a poor job at resolving convective variability because their low spatial resolution does

not resolve all the processes important for LSW variability (e.g. Irminger Rings). Therefore, the idealized process studies outlined earlier are very important to assess the consequence of such a shortcoming.

While studying the above questions, one needs to keep in mind that the different processes can interfere with each other in an unexpected way. The effect of the low surface salinity on the surface buoyancy flux, discussed in chapter 3, is a good example of such an unexpected interplay. The surface feedbacks found from careful analysis of the *in situ* data would likely not have been revealed in a process study where either the salinity fluxes or the surface buoyancy fluxes are enforced using an idealized model like the one applied in chapter 2. On the other hand, such idealized process studies are very useful to provide more insight into the effects of individual processes over a certain parameter regime. It is thus the combination of process-orientated idealized model studies and analyses of *in situ* data that could help most towards a better understanding of the convective variability.

Bibliography

- Alley, R. B., Marotzke, J., Nordhaus, W. D., Overpeck, J. T., Peteet, D. M., Pielke, R. A., Pierrehumbert, R. T., Rhines, P. B., Stocker, T. F., Talley, L. D. and Wallace, J. M.: 2003, Abrupt climate change, *Science* **299**, 2005–2010.
- AVI: 2011, *SSALTO/DUACS user handbook: (M)SLA and (M)ADT near-real time and delayed time products*, 2rev 6 edn. Reference: CLS-DOS-NT-06-034.
- Avsic, T., Karstensen, J., Send, U. and Fischer, J.: 2006, Interannual variability of newly formed Labrador Sea Water from 1994 to 2005, *Geophysical Research Letters* **33**, L21S02.
- Belkin, I. M., Levitus, S., Antonov, J. and Malmberg, S. A.: 1998, Great Salinity Anomalies in the North Atlantic, *Progress in Oceanography* **41**, 1–68.
- Biastoch, A., Böning, C. W. and Getzlaff, J.: 2008, Causes of interannual-decadal variability in the meridional overturning circulation of the midlatitude North Atlantic Ocean, *Journal of climate* **21**, 6599–6615.
- Bower, A. S., Lozier, M. S., Gary, S. F. and Böning, C. W.: 2009, Interior pathways of the North Atlantic meridional overturning circulation, *Nature* **459**, 243–248.
- Bracco, A. and Pedlosky, J.: 2003, Vortex generation by topography in locally unstable baroclinic flows, *Journal of Physical Oceanography* **33**, 207–219.
- Bramson, L.: 1997, Air-sea interactions and deep convection in the Labrador Sea, M.S. thesis, Department of Oceanography, Naval Postgraduate School, 76 pp.
- Brandt, P., Funk, A., Czeschel, L., Eden, C. and Böning, C. W.: 2007, Ventilation and transformation of Labrador Sea Water and its rapid export in the deep Labrador Current, *Journal of Physical Oceanography* **37**, 946–961.
- Brandt, P., Schott, F. A., Funk, A. and Martins, C. S.: 2004, Seasonal to interannual variability of the eddy field in the Labrador Sea from satellite altimetry, *Journal of Geophysical Research* **109**, C02028.
- Broecker, W. S.: 1997, Thermohaline circulation, the Achilles heel of our climate system: Will man-made CO₂ upset the current balance?, *Science* **278**, 1582–1588.

- Broecker, W. S., Peteet, D. M. and Rind, D.: 1985, Does the ocean-atmosphere system have more than one stable mode of operation, *Nature* **315**, 21–26.
- Chanut, J., Barnier, B., Large, W., Debreu, L., Penduff, T., Molines, J. M. and Mathiot, P.: 2008, Mesoscale eddies in the Labrador Sea and their contribution to convection and restratification, *Journal of Physical Oceanography* **38**, 1617–1643.
- Clark, P. U., Pisias, N. G., Stocker, T. F. and Weaver, A. J.: 2002, The role of the thermohaline circulation in abrupt climate change, *Nature* **415**, 863–869.
- Clarke, R. A. and Gascard, J. C.: 1983, The formation of Labrador Sea Water. Part I: Large-scale processes, *Journal of Physical Oceanography* **13**, 1764–1778.
- Cuny, J., Rhines, P. B., Niiler, P. P. and Bacon, S.: 2002, Labrador Sea boundary currents and the fate of the Irminger Sea Water, *Journal of Physical Oceanography* **32**, 627–647.
- Curry, R. G., McCartney, M. S. and Joyce, T. M.: 1998, Oceanic transport of subpolar signals to mid-depth subtropical waters, *Nature* **391**, 575–577.
- Dee, D. P., Uppala, S. M., Simmons, A. J., Berrisford, P., Poli, P., Kobayashi, S., Andrae, U., Balmaseda, M. A., Balsamo, G., Bauer, P., Bechtold, P., Beljaars, A. C. M., van de Berg, L., Bidlot, J., Bormann, N., Delsol, C., Dragani, R., Fuentes, M., Geer, A. J., Haimberger, L., Healy, S. B., Hersbach, H., Hólm, E. V., Isaksen, L., Kållberg, P., Köhler, M., Matricardi, M., McNally, A. P., Monge-Sanz, B. M., Morcrette, J.-J., Park, B.-K., Peubey, C., de Rosnay, P., Tavolato, C., Thépaut, J.-N. and Vitart, F.: 2011, The era-interim reanalysis: Configuration and performance of the data assimilation system, *Quart. J. Roy. Meteor. Soc.* **137**(656), 553–597.
- Dengler, M., Fischer, J., Schott, F. A. and Zantopp, R.: 2006, Deep Labrador Current and its variability in 1996–2005, *Geophysical Research Letters* **33**, L21S06.
- Dickson, R. R., Lazier, J., Meincke, J., Rhines, P. and Swift, J.: 1996, Long-term coordinated changes in the convective activity of the North Atlantic, *Progress in Oceanography* **38**, 241–295.
- Dickson, R. R., Meincke, J., Malmberg, S. and Lee, A. J.: 1988, The “Great salinity anomaly” in the northern North Atlantic 1968–1982, *Progress in Oceanography* **20**, 103–151.
- Eden, C. and Böning, C. W.: 2002, Sources of eddy kinetic energy in the Labrador Sea, *Journal of Physical Oceanography* **32**, 3346–3363.
- Eden, C. and Willebrand, J.: 2001, Mechanism of Interannual to Decadal Variability of the North Atlantic Circulation, *Journal of Climate* **14**, 2266–2280.
- Fairall, C. W., Bradley, E. F., Hare, J. E., Grachev, A. A. and Edson, J. B.: 2003, Bulk parameterization of air-sea fluxes: Updates and verification for the COARE algorithm, *Journal of Climate* **16**, 571–591.
- Fischer, J., Visbeck, M., Zantopp, R. and Nunes, N.: 2010, Interannual to decadal variability of outflow from the Labrador Sea, *Geophysical Research Letters* **37**, L24610.
- Ganachaud, A. and Wunsch, C.: 2000, Improved estimates of global ocean circulation, heat transport and mixing from hydrographic data, *Nature* **408**, 453–457.
- Gill, A. E.: 1982, *Atmosphere-ocean dynamics*, Academic Press.

- Haak, H., Jungclaus, J., Mikolajewicz, U. and Latif, M.: 2003, Formation and propagation of great salinity anomalies, *Geophysical Research Letters* **30**, 1473–1476.
- Haine, T. W. N. and Marshall, J.: 1998, Gravitational, symmetric, and baroclinic instability of the ocean mixed layer, *Journal of Physical Oceanography* **28**, 634–658.
- Häkkinen, S.: 1999, A simulation of thermohaline effects of a great salinity anomaly, *Journal of Climate* **12**, 1781–1795.
- Häkkinen, S. and Rhines, P. B.: 2004, Decline of the subpolar North Atlantic circulation during the 1990s, *Science* **304**, 555–559.
- Hatun, H., Eriksen, C. C. and Rhines, P. B.: 2007, Buoyant eddies entering the Labrador Sea observed with gliders and altimetry, *Journal of Physical Oceanography* **37**, 2838–2854.
- Herrmann, M., Bouffard, J. and Béranger, K.: 2009, Monitoring open-ocean deep convection from space, *Geophysical Research Letters* **36**, L03606.
- Houghton, R. W. and Visbeck, M. H.: 2002, Quasi-decadal salinity fluctuations in the Labrador Sea, *Journal of Physical Oceanography* **32**, 687–701.
- Hurrell, J. W.: 1995, Decadal trends in the North Atlantic Oscillation: regional temperatures and precipitation, *Science* **269**, 676–679.
- IOC, SCOR and IAPSO: 2010, The international thermodynamic equation of seawater 2010: Calculation and use of thermodynamic properties, *Intergovernmental Oceanographic Commission, Manuals and Guides No. 56*. . UNESCO.
- Jones, H. J. and Marshall, J.: 1993, Convection with rotation in a neutral ocean: A study of open-ocean deep convection, *Journal of Physical Oceanography* **23**, 1009–1039.
- Jones, H. J. and Marshall, J.: 1997, Restratification after deep convection, *Journal of Physical Oceanography* **27**, 2276–2287.
- Katsman, C. A., Spall, M. A. and Pickart, R. S.: 2004, Boundary current eddies and their role in the restratification of the Labrador Sea, *Journal of Physical Oceanography* **34**, 1967–1983.
- Khawwala, S., Schlosser, P. and Visbeck, M.: 2002, Rates and mechanisms of water mass transformation in the Labrador Sea as inferred from tracer observations, *Journal of Physical Oceanography* **32**, 666–686.
- Kieke, D., Rhein, M., Stramma, L., Smethie, W. M., Bullister, J. L. and LeBel, D. A.: 2007, Changes in the pool of Labrador Sea Water in the subpolar North Atlantic, *Geophysical Research Letters* **34**, L06605.
- Kistler, T., Kalnay, E., Collins, W., Saha, S., White, G., Wollen, R., Chelliah, M., Ebisuzaki, W., Kanamitsu, M., Kousky, V., van den Dool, H., Jenne, R. and Fiorino, M.: 2001, The NCEP-NCAR 50-year reanalysis: Monthly means CD-ROM and documentation., *Bulletin of the American Meteorological Society* **82**, 247–268.
- Kuhlbrodt, T., Griesel, A., Montoya, M., Levermann, A., Hofmann, M. and Rahmstorf, S.: 2007, On the driving processes of the Atlantic meridional overturning circulation, *Reviews of Geophysics* **45**, RG2001.
- Kuhlbrodt, T., Titz, S., Feudel, U. and Rahmstorf, S.: 2001, A simple model of seasonal open ocean convection, *Ocean Dynamics* **52**, 36–49.

- Kwok, R., Cunningham, G. F., Wensnahan, M., Rigor, I., Zwally, H. J. and Yi, D.: 2009, Thinning and volume loss of the Arctic Ocean sea ice cover, *Journal of Geophysical Research* **114**, C07005.
- LabSeaGroup: 1998, The Labrador Sea deep convection experiment, *Bulletin of the American Meteorological Society* **79**, 2033–2058.
- Lavender, K. L., Davis, R. E. and Owens, W. B.: 2000, Mid-depth recirculation observed in the interior Labrador and Irminger Seas by direct velocity measurements, *Nature* **407**, 66–69.
- Lavender, K. L., Davis, R. E. and Owens, W. B.: 2002, Observations of open-ocean deep convection in the Labrador Sea from subsurface floats, *Journal of Physical Oceanography* **32**, 511–526.
- Lavender, K. L., Owens, W. B. and Davis, R. E.: 2005, The mid-depth circulation of the subpolar North Atlantic Ocean as measured by subsurface floats, *Deep-Sea Research I* **52**, 767–785.
- Lazier, J. R. N.: 1973, The renewal of Labrador Sea Water, *Deep-Sea Research* **20**, 341–353.
- Lazier, J. R. N.: 1980, Oceanographic conditions at ocean weather ship Bravo, 1964–1974, *Atmosphere-Ocean* **18**, 227–238.
- Lazier, J. R. N., Hendry, R., Clarke, A., Yashayaev, I. and Rhines, P.: 2002, Convection and restratification in the Labrador Sea, *Deep-Sea Research I* **49**, 1819–1835.
- Legg, S., Jones, H. and Visbeck, M.: 1996, A heton perspective of baroclinic eddy transfer in localized open ocean convection, *Journal of Physical Oceanography* **26**, 2251–2266.
- Legg, S., McWilliams, J. and Gao, J.: 1998, Localization of deep convection by a mesoscale eddy, *Journal of Physical Oceanography* **28**, 944–970.
- Lenderink, G. and Haarsma, R. J.: 1994, Variability and multiple equilibria of the thermohaline circulation associated with deep-water formation, *Journal of Physical Oceanography* **24**, 1480–1493.
- Lilly, J. M. and Rhines, P. B.: 2002, Coherent eddies in the Labrador Sea observed from a mooring, *Journal of Physical Oceanography* **32**, 585–598.
- Lilly, J. M., Rhines, P. B., Davis, R., Lazier, J. R. N., Schott, F. and Farmer, D.: 1999, Observing deep convection in the Labrador Sea during winter 1994/95, *Journal of Physical Oceanography* **29**, 2065–2098.
- Lilly, J. M., Rhines, P. B., Schott, F., Lavender, K., Lazier, J., Send, U. and D’Asaro, E.: 2003, Observations of the Labrador Sea eddy field, *Progress in Oceanography* **59**, 75–176.
- Marotzke, J. and Scott, J. R.: 1999, Convective mixing and the thermohaline circulation, *Journal of Physical Oceanography* **29**, 2962–2970.
- Marshall, J., Adcroft, A., Hill, C., Perelman, L. and Heisey, C.: 1997, A finite-volume, incompressible Navier Stokes model for studies of the ocean on parallel computers, *Journal of Geophysical Research* **102**, 5753–5766.
- Marshall, J. and Schott, F.: 1999, Open-ocean convection: Observations, theory, and models, *Review of Geophysics* **37**, 1–64.

- Maslanik, J., Stroeve, J., Fowler, C. and Emery, W.: 2011, Distribution and trends in Arctic sea ice through spring 2011, *Geophysical Research Letters* **38**, L13502.
- Maxworthy, T. and Narimousa, S.: 1994, Unsteady, turbulent convection into a homogeneous, rotating fluid with oceanographic applications, *Journal of Geophysical Research* **24**, 865–887.
- McDougall, T. J., Jackett, D. R. and Millero, F. J.: 2009, An algorithm for estimating Absolute Salinity in the global ocean, *Ocean Science Discussions* **6**, 215–242.
- MEDOC-Group: 1970, Observations of formation of deep-water in the Mediterranean Sea, 1969, *Nature* **227**, 1037–1040.
- Mizoguchi, K., Morey, S. L., Zavala-Hidalgo, J., Sugimoto, N., Häkkinen, S. and O'Brien, J. J.: 2003, Convective activity in the Labrador Sea: Preconditioning associated with decadal variability in subsurface ocean stratification, *Journal Geophysical Research* **108**, 3330.
- Molinari, R. L., Fine, R. A., Wilson, W. D., Curry, R. G., Abell, J. and McCartney, M. S.: 1998, The arrival of recently formed Labrador Sea Water in the Deep Western Boundary Current at 26.5°N, *Geophysical Research Letters* **25**, 2249–2252.
- Myers, P. G. and Donnelly, C.: 2008, Water mass transformation and formation in the Labrador Sea, *Journal of Climate* **21**, 1622–1638.
- Pickart, R. S. and Spall, M. A.: 2007, Impact of Labrador Sea convection on the North Atlantic meridional overturning circulation, *Journal of Physical Oceanography* **37**, 2207–2227.
- Pickart, R. S., Spall, M. A., Ribergaard, M. H., Moore, G. W. K. and Milliff, R. F.: 2003, Deep convection in the Irminger Sea forced by the Greenland tip jet, *Nature* **424**, 152–156.
- Pickart, R. S., Torres, D. J. and Clarke, R. A.: 2002, Hydrography of the Labrador Sea during active convection, *Journal of Physical Oceanography* **32**, 428–457.
- Prater, M. D.: 2002, Eddies in the Labrador Sea as observed by profiling RAFOS floats and remote sensing, *Journal of Physical Oceanography* **32**, 411–427.
- Price, J. F., Weller, R. A. and Pinkel, R.: 1986, Diurnal cycling: Observations and models of the upper ocean response to diurnal heating, cooling and wind mixing, *Journal Geophysical Research* **91**, 8411–8427.
- Renfrew, I. A., Moore, G. W. K., Guest, P. S. and Bumke, K.: 2002, A comparison of surface layer and surface turbulent flux observations over the Labrador Sea with ECMWF analyses and NCEP reanalyses., *Journal of Physical Oceanography* **32**, 383–400.
- Rignot, E., Velicogna, I., van den Broeke, M. R., Monaghan, A. and Lenaerts, J. T. M.: 2011, Acceleration of the contribution of the Greenland and Antarctic ice sheets to sea level rise, *Geophysical Research Letters* **38**, L05503.
- Roemmich, D., Johnson, G. C., Riser, S., Davis, R., Gilson, J., Owens, W. B., Garzoli, S. L., Schmid, S. and Ignaszewski, M.: 2009, The Argo program: Observing the global ocean with profiling floats, *Oceanography* **22**, 34–43.
- Roemmich, D. and the Argo Steering Team: 2009, The challenge of continuing 10 years of progress, *Oceanography* **22**, 46–55.

- Rykova, T., Straneo, F., Lilly, J. M. and Yashayaev, I.: 2009, Irminger Current anticyclones in the Labrador Sea observed in the hydrographic record, 1990-2004, *Journal of Marine Research* **67**, 361–384.
- Samelson, R. M.: 2004, Simple mechanistic models of middepth meridional overturning, *Journal of Physical Oceanography* **34**, 2096–2103.
- Sathiyamoorthy, S. and Moore, G. W. K.: 2002, Buoyancy flux at ocean weather station Bravo, *Journal of Physical Oceanography* **32**, 458–474.
- Schmidt, S. and Send, U.: 2007, Origin and composition of seasonal Labrador Sea freshwater, *Journal of Physical Oceanography* **37**, 1445–1454.
- Send, U. and Käse, R.: 1998, Parameterization of processes in deep convection regimes, in E. Chassignet and J. Verron (eds), *Ocean modelling and parameterization*, Kluwer Academic Publishers, pp. 191–214.
- Spall, M. A.: 2004, Boundary currents and water mass transformation in marginal seas, *Journal of Physical Oceanography* **34**, 1197–1213.
- Spall, M. A.: 2007, Circulation and water mass transformation in a model of the Chukchi Sea, *Journal of Geophysical Research* **112**.
- Spall, M. A. and Chapman, D. C.: 1998, On the efficiency of baroclinic eddy heat transport across narrow fronts, *Journal of Physical Oceanography* **28**, 2275–2287.
- Spall, M. A. and Pickart, R. S.: 2001, Where does dense water sink? A subpolar gyre example, *Journal of Physical Oceanography* **31**, 810–826.
- Spall, M. A. and Pickart, R. S.: 2003, Wind-driven recirculations and exchange in the Labrador and Irminger Seas, *Journal of Physical Oceanography* **33**, 1829–1845.
- Stommel, H. M.: 1961, Thermohaline convection with two stable regimes of flow, *Tellus* **13**, 224–230.
- Straneo, F.: 2006a, Heat and freshwater transport through the central Labrador Sea, *Journal of Physical Oceanography* **36**, 606–628.
- Straneo, F.: 2006b, On the connection between dense water formation, overturning, and poleward heat transport in a convective basin., *Journal of Physical Oceanography* **36**, 1822–1840.
- Talley, L. D. and McCartney, M. S.: 1982, Distribution and circulation of Labrador Sea Water, *Journal of Physical Oceanography* **12**, 1189–1205.
- Uppala, S. M., Kallberg, P. W., Simmons, A. J., Andrae, U., da Costa Bechtold, V., Fiorino, M., Gibson, J. K., Haseler, J., Hernandez, A., Kelly, G. A., Li, X., Onogi, K., Saarinen, S., Sokka, N., Allan, R. P., Andersson, E., Arpe, K., Balmaseda, M. A., Beljaars, A. C. M., van de Berg, L., Bidlot, J., Bormann, N., Caires, S., Chevallier, F., Dethof, A., Dragosavac, M., Fisher, M., Fuentes, M., Hagemann, S., Holm, E., Hoskins, B. J., Isaksen, I., Janssen, P. A. E. M., Jenne, R., McNally, A. P., Mahfouf, J. F., Morcrette, J. J., Rayner, N. A., Saunders, R. W., Simon, P., Sterl, A., Trenberth, K. E., Untch, A., Vasiljevic, D., Viterbo, P. and Woollen, J.: 2005, The ERA-40 re-analysis, *Quarterly Journal of the Royal Meteorological Society* **131**, 2961–3012.

- Våge, K., Pickart, R. S., Moore, G. W. K. and Ribergaard, M. H.: 2008, Winter mixed layer development in the central Irminger Sea: The effect of strong intermittent wind events, *Journal of Physical Oceanography* **38**, 541–565.
- Våge, K., Pickart, R. S., Thierry, V., Reverdin, G., Lee, C. M., Petrie, B., Agnew, T. A., Wong, A. and Ribergaard, M. H.: 2009, Surprising return of deep convection to the subpolar North Atlantic Ocean in winter 2007-2008, *Nature Geoscience* **2**, 67–72.
- Visbeck, M., Marshall, J. and Jones, H.: 1996, Dynamics of isolated convective regions in the ocean, *Journal of Physical Oceanography* **26**, 1721–1734.
- Welander, P.: 1982, A simple heat-salt oscillator, *Dynamics of Atmospheres and Oceans* **6**, 233–242.
- Wolfe, C. L. and Cenedese, C.: 2006, Laboratory experiments on eddy generation by a buoyant coastal current flowing over variable bathymetry, *Journal of Physical Oceanography* **36**, 395–411.
- Wunsch, C. and Ferrari, R.: 2004, Vertical mixing, energy, and the general circulation of the ocean, *Annual Review of Fluid Mechanics* **36**, 281–314.
- Yashayaev, I.: 2007, Hydrographic changes in the Labrador Sea, 1960-2005, *Progress in Oceanography* **73**, 242–276.
- Yashayaev, I. and Dickson, R. R.: 2008, Transformation and fate of overflows in the North Atlantic, in R. R. Dickson, J. Meincke and P. Rhines (eds), *Arctic-Subarctic Ocean Fluxes*, Springer, pp. 505–526.
- Yashayaev, I. and Loder, J.: 2009, Enhanced production of Labrador Sea Water in 2008, *Geophysical Research Letters* **36**, L01606.

Acknowledgments

"Silent gratitude isn't much use to anyone."

G.B. Stern

After four years of work, I am left with one or two pages in my thesis to appropriately thank everyone who has helped me to get where I am now. As stated in every thesis: I will likely forget someone, for which I apologize in advance.

The one person I could never forget to thank is my daily advisor and co-promotor Caroline Katsman. You held my hand when I took my first steps in the scientific landscape, taught me all I needed to know to successfully finish this thesis, introduced me in other places, and did not stop me in any of my crazy plans (even encouraged it I believe) to do a ten-week summer program, go on a research cruise, attend conferences and, while I'm in the neighbourhood, spend a few extra days there to give some presentations and talk to other people about my work. Your confidence and support, during good days as well as the difficult period, have been indispensable.

Second, I would like to thank my promotor Will de Ruijter. Your encouraging and calm style of supervision and the safe atmosphere you create in the group meetings have helped me greatly to grow as a scientist. Thank you for your advice throughout these four years and for your swift response on the completed thesis.

Two other people who deserve a separate thank you are Fiamma en Sybren. Both of you supervised or co-supervised me during part of my PhD project. I really enjoyed working with both of you and I am grateful for your time and inspiration.

I am most indebted to all my colleagues from the Global Climate division at the KNMI. You made work a great place to be! I don't think I'll encounter a group again where you are expected to bring cake on your birthday, stroopwafels for every accepted paper and sweets or cookies from every foreign trip; coffee will never be the same again. Outside of work hours you filled a substantial part of my social life with informal dinners and parties. A special thanks goes to Helio, my office mate throughout the first three years here at KNMI. I thoroughly enjoyed the Dutch lessons, our many conversations about the Dutch high school system and your never-ending enthusiasm for my colorful pictures. Thank you in particular

for your support during rough times. Thanks Eveline for your company during the last few months, and thanks as well to all the colleagues I have not named in person!

All the people at the physical oceanography group at IMAU: thank you for inviting me into the group as one of your own. Ann, thank you for giving me a home away from home. Emily, thank you for making me feel like a local! Colm and Andrew, thank you for teaching me how to do lab experiments and letting me use your camera. Thanks to Hendrik and Janine for taking me out to sea; in the end, that is what oceanography is all about. Thank you to all my friends for the numerous supporting diversions.

And last but not least, thank you to my family for your unconditional support. Anne, Nienke, Wietse and Hjalmar, thank you for the warmth you have provided. Thank you for believing in me. And thank you for providing a safe base, from which I can always explore new territory.

Renske Gelderloos
Utrecht
April 12, 2012

Curriculum Vitae

Renske Gelderloos was born on 13 February 1983 in Zuidhorn, The Netherlands. After five years she moved with her parents to Bennebroek, where she attended the Atheneum College Hageveld in Heemstede from 1995 to 2001. After graduating high school, she moved again to study Civil Engineering and Management at the University of Twente, followed by a Masters in Water Management and Engineering from which she graduated cum laude. During the course of her studies, she noticed that she was more interested in the underlying physical principles of the water system than in the human impact on it. At the same time, her enthusiasm for sailing had been taken to a whole new level through the sea sailing activities at the student yacht club, where she sailed as a skipper on the sea-going yachts. These developments made her decide to pursue a PhD in physical oceanography. In 2008 she could start a PhD program at the Royal Netherlands Meteorological Institute in collaboration with Utrecht University on variability of deep water formation in the Labrador Sea. The results from that study are described in this thesis. In the coming years, Renske will move up her research area further northwards when she works as a postdoc at the University of Oxford on the Canadian Archipelago.